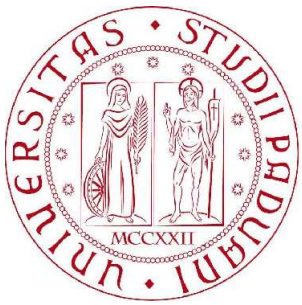

Sede Amministrativa: Università degli studi di Padova

Dipartimento di Astronomia

SCUOLA DI DOTTORATO DI RICERCA IN ASTRONOMIA

CICLO XXII

FORMATION OF DARK MATTER HALOES: MODELS AND SIMULATIONS

Coordinatore della Scuola: Ch.mo Prof. Giampaolo Piotto
Supervisore : Ch.mo Prof. Giuseppe Tormen

Dottorando: Federico Biondi

"Under normal conditions the research scientist is not an innovator but a solver of puzzles, and the puzzles upon which he concentrates are just those which he believes can be both stated and solved within the existing scientific tradition."

Thomas S. Kuhn

Contents

List of Figures

Abstract

At present, the best model for the Universe as a whole is given by the so called "Hot Big Bang", which describes an expanding universe in which the density and temperature of matter and radiation are followed in time. The value of the parameters characterizing the observed universe is summarized by the concordance ΛCDM model, where CDM stands for Cold Dark Matter (the main matter component), and Λ is the cosmological constant (some kind of unknown energy, with an anti-gravitational effect). According to this model, the universe is spatially flat (i.e. the density parameter Ω equals one), and 75% of its energy balance is assigned to dark energy, about 20% to dark matter and about 5% to ordinary (baryonic) matter; the expansion speed assumes a value $H_0 = 70.5$ Km/s/Mpc (the Hubble parameter).

The present dissertation focuses on the distribution of dark matter into virialized structures, called dark matter haloes. According to structure formation theory, cosmic structures originates from the amplification of quantum fluctuations during an early stage of accelerated expansion (cosmic inflation); these perturbations grow by self-gravity until they collapse and originate virialized structures. In the linear regime (when fluctuations are small), this process is well understood by the Jeans' theory. The non linear regime is much harder to describe; erlier attempts assumed a simple spherical simmetry, where the collapse is driven only by the internal density (e.g. Peebles, 1980); more recently (White & Silk 1979; Bond & Myers 1996) this hypothesis has been relaxed, and a more complex model was proposed in which proto-structures are described by triaxial ellipsoids, governed by their internal density and shape.

Using the results coming from the dynamical analysis of the spherical collapse, and exploiting the statistical "excursion sets formalism", it is possible to obtain analytical information about the mass distribution of dark matter haloes. In this approach, for each particle in the universe, the trajectory describing the density evolution of a sphere of matter built around that particle is modeled as a random walk as a function of the mass M within that sphere. When a trajectory crosses some pre-defined threshold, one assumes that a virialized structure of mass M has formed.

By considering all the particles in the universe one obtains analytical forms for the

global mass function, and for the progenitor and descendant mass functions. From these it is possible to calculate other quantities, like the (instantaneous and integrated) rates of creation and destruction of dark matter haloes.

In the 1990's the ellipsoidal collapse was first tried in order to find a better match with numerical simulations. However, partly due to the analytical complexity of the model, until now one can still not find in the literature analytical forms for e.g. the descendant and merger rate distributions (see Table 4.3).

The main goal of this work is to provide such expressions for a number of statistics related to the mass distributions of dark matter haloes, striving to obtain simple and accurate formulas. In order to do so, we start from the statistical considerations by Sheth, Mo e Tormen (2001), who introduced the dynamical effects of the ellipsoidal collapse into the excursion sets formalism just by modifying the shape of the density threshold. Sheth and Tormen (2002) further suggested an new expression for the ellipsoidal global mass function, using a Taylor expansion series for the barrier: this expression allows one to also derive analytical formulas for the conditional mass functions. We obtain a set of models changing the order of this Taylor expansion, and considering the normalization of the distribution as a free parameter; we then compare these equations with the results of the cosmological simulation Gif2 (Gao et al. 2004) and, in some cases, with the Millennium Simulation (Springel et al. 2005). For the global and conditional mass functions the match between models and simulations is estimated using a χ^2-method. For the merger rates we compare the results qualitatively, whereas for the creation rates we only derived analytical results. We especially focus on the cases providing the simplest analytical expressions: the zero-order and the infinite-orders Taylor series.

In the last part of the dissertation we propose a new statistical method that can overcome two inconvenients of χ^2-methods: (i) data binning and (ii) neglect of field particles (dust) in simulations. Concerning point (i), different bin-sizes can lead to small differences in the χ^2-results. As for point (ii), particles that are not bound to haloes are usually considered only for computing the normalization. By using a maximum likelihood analysis we can treat unbinned data, as well as take into account dust in the determination of the best parameters of the mass function. Our tests are performed by comparing a two-parameter mass function with results of Monte Carlo simulations.

Our work naturally settles within the systematic search of analytical expressions associated to the ellipsoidal collapse of dark matter haloes. Since haloes are thought to be the sites where baryons can condense and form stars, galaxies and other luminous objects, the expression we derive can be used for a number of applications, ranging from unveiling the nature of dark matter through self-annihilation, to the understanding of the mechanisms leading to galaxy formation. Furthermore, the description of galaxy evolution requires knowledge on the hosting haloes: semi-analytical models of

galaxy formation depend on the global mass function of the dark matter haloes, and the corrisponding merger-trees are based on the progenitor mass functions. The rates of creation and destruction are useful to compute the abundances of objects like Active Galactic Nuclei (AGNs) and Super Massive Black Holes (SMBHs). Many other examples can be found in the literature for the use of dark matter distributions in studies of galaxy formation.

The structure of the dissertation is as follows: **Chapters 1** justifies the need of dark matter. In **Chapters 2** we present the concordance cosmological model, its geometry and thermal history. We also introduce the linear and non-linear models for the formation of dark matter haloes. **Chapter 3** describes the excursion sets approach in the framework of the spherical collapse. The extension of this method to the ellipsoidal collapse is given in **Chapter 4**, where the firsts analytical results are derived. In **Chapter 5** we compare our analytical predictions to a number of results from numerical simulations. **Chapter 6** is devoted to the new maximum likelihood tests with unbinned data and dust particles. We finally draw our **Conclusions**, followed by one **Appendix** where the numerical simulations are described.

Sommario

La miglior descrizione dell'Universo, di cui si dispone al momento, è il modello del "Big Bang Caldo", che contempla un universo in espansione nel quale viene seguita l'evoluzione temporale della densità e della temperatura della materia e della radiazione. I parametri che caratterizzano l'Universo osservato sono riassunti in un modello chiamato ΛCDM di concordanza: CDM sta per Cold Dark Matter (la componente dominante della materia), e Λ è la costante cosmologica (una sorta di energia oscura, con effetto anti-gravitazionale). Secondo questo modello, l'universo è spazialmente piatto (cioè il parametro di densità Ω è uguale a uno), e il 75% del suo bilancio energetico è assegnato all'energia oscura, circa il 20% alla materia oscura e circa il 5% alla materia ordinaria (barioni); la velocità dell'espansione assume il valore 70.5 Km/s/Mpc (parametro di Hubble).

Questa tesi si sofferma sulla distribuzione della materia oscura in strutture virializzate, chiamate aloni di materia oscura. Secondo la teoria di formazione delle strutture, le strutture cosmiche hanno origine dall'amplificazione di fluttuazione quantistiche durante un periodo iniziale di espansione accelerata (inflazione cosmica); queste perturbazioni crescono per effetto dell'autogravità fino al collasso, creando delle strutture virializzate. Durante il regime lineare (quando le fluttuazioni sono piccole), questo processo è ben descritto dalla teoria di Jeans. Il regime non lineare è molto più difficile da descrivere; i primi tentativi assumono una simmetria sferica, per la quale il collasso è descritto solo dalla densità interna (es. Peebles, 1980); più recentemente (White & Silk 1979; Bond & Myers 1996) questa ipotesi è stata rilassata, ed è stato proposto un modello più complesso nel quale le protostrutture sono descritte da ellissoidi triassiali, regolati dalla loro densità interna e dalla loro forma.

Utilizzando i risultati ottenuti dall'analisi dinamica del collasso sferico e sfruttando il formalismo statistico degli "excursion set", è possibile ottenere informazioni analitiche in merito alla distribuzione di massa degli aloni di materia oscura. In questo approccio, per ogni particella nell'universo, la traiettoria che descrive l'evoluzione della densità della sfera di materia costruita attorno a quella particella viene modellata come un cammino browniano come funzione della massa M all'interno della sfera. Quando una

traiettoria interseca una pre-definita soglia, si assume che venga a formarsi una struttura virializzata di massa M.

Considerando tutte le particelle dell'universo, si ottengono forme analitiche per la funzione di massa globale, e per le funzioni di massa dei progenitori e dei figli. Da queste, è possibile calcolare altre quantità, come i tassi di creazione e distruzione (istantanei e integrati).

Negli anni '90, il collasso ellissoidale è stato utilizzato per trovare un miglior accordo con le simulazioni numeriche. Tuttavia, in parte a causa della complessità analitica del modello, fino ad ora non è stato ancora possibile trovare in letteratura forme analitiche per esempio per la funzione dei figli o per i tassi di distruzione (vedi Tabella 4.3).

l'obiettivo principale di questo lavoro è di fornire tali espressioni per una serie di funzioni legate alle distribuzione di massa degli aloni di materia oscura, aspirando ad ottenere delle formule semplici ed accurate. Per farlo, siamo partiti dalle considerazioni statistiche di Sheth, Mo e Tormen (2001) che introducono gli effetti dinamici del collasso ellissoidale nel formalismo excursion sets, modificando la forma della soglia di densità. Sheth e Tormen (2002), inoltre, propongono una nuova espressione per la funzione di massa globale ellissoidale, usando uno sviluppo in serie di Taylor per la barriera: questa espressione permette di derivare forme analitiche anche per le funzioni di massa condizionali. Abbiamo ottenuto un set di modelli cambiando l'ordine di questo sviluppo di Taylo, e considerando la normalizzazione delle distribuzioni come un parametro libero; abbiamo poi confrontato queste equazioni con i risultati della simulazione cosmologica Gif2 (Gao et al. 2004) e, in alcuni casi, con la Millennium Simulation (Springel et al. 2005). Per le funzioni di massa globale e condizionali, l'accordo tra modelli e simulazioni è stimato usando un metodo χ^2. Per i merger rates abbiamo confronti qualitativi, mentre per i tassi di creazione abbiamo derivato le sole equazioni analitiche. Ci siamo soffermati specialmente sui casi che forniscono le espressioni analiticamente più semplici: le serie di Taylor con zero ordini e con infiniti ordini.

Nell'ultima parte della tesi, proponiamo un nuovo metodo statistico che può scartare gli inconvenienti dei metodi χ^2: (i) la divisione in intervalli dei dati e (ii) il trascurare le particelle di campo (polvere) delle simulazioni. Per quanto riguarda il punto (i), differenti ampiezze degli internalli di massa possono portare a piccole differenze nei risultati del χ^2. Il punto (ii) si riferisce al fatto che le particelle che non sono legate in aloni sono di solito considerate solo per il calcolo della normalizzazione. Usando un'analisi di massima verosimiglianza, possiamo trattare dati non raggruppati in intervalli e considerare la polvere nella determinazione dei parametri migliori per la funzione di massa. I nostri tests sono condotti confrontando una funzione di massa a due parametri con i risultati di simulazioni Monte Carlo.

Il nostro lavoro si inserisce naturalmente nella ricerca sistematica delle espressioni

analitiche associate al collasso ellissoidale degli aloni di materia oscura. Poichè si pensa che gli aloni siano i siti ove i barioni possono concentrarsi e formare stelle, galassie ed altri oggetti luminosi, le espressioni che otteniamo possono essere usate in varie applicazioni, dallo svelare la natura della materia oscura attraverso l'auto annichilazione, fino alla comprensione dei meccanismi che portano alla formazione galattica. Inoltre, la descrizione dell'evoluzione galattica richiede la conoscenza dell'alone correlato: i modelli semi-analitici di formazione galattica dipendono dalla funzione di massa globale degli aloni di materia oscura, e i corrispondenti merger-trees sono basati sulle funzioni di massa dei progenitori. I tassi di creazione e distruzione sono utili per calcolare le abbondanze di oggetti come Nuclei Galattici Attivi (AGN) e Buchi Neri Super Massicci (SMBH). Altri esempi dell'utilizzo delle distribuzioni della materia oscura in studi di formazione galattica si possono trovare copiosi in letteratura.

L'elaborato si articola in questo modo: il **Capitoli 1** giustifica la necessità della materia oscura. Nel **Capitolo 2** presentiamo il modello cosmologico di concordanza, la sua geometria e la storia termica. Inoltre, introduciamo i modelli, lineare e non lineare, di formazione degli aloni di materia oscura. Il **Capitolo 3** descrive l'approccio degli excursion sets nel contesto del collasso sferico. L'estensione di questo metodo al collasso ellissoidale è proposto nel **Capitolo 4**, ove vengono esposti i primi risultati analitici. Nel **Capitolo 5** confrontiamo le nostre predizioni analitiche con i risultati di due simulazioni numeriche. Il **Capitolo 6** è dedicato all'esposizione dei test di un nuovo metodo di massima verosimiglianza con l'utilizzo di dati non raggruppati in intervalli e con le particelle di polvere. Infine tracciamo le nostre **Conclusioni**, seguite da un'**Appendice** ove sono descritte le simulazioni numeriche.

Chapter 1

Necessity of Dark Matter

An usual way to describe the energetic properties of the Universe is the use of the *density parameter* Ω, that shows the ratio between the energy density associated to a component, and the *critical density* that discriminates between closed and open universes. Each component that fills the universe has an associated density parameter and a law that describes its time evolution. From the analysis of the density parameters one can notice that the two most important energetic components are the most problematic ones: the Dark Energy ($\Omega_\Lambda \sim 0.721$) and the Dark Matter ($\Omega_{DM} \sim 0.233$) (baryonic matter has $\Omega_{BM} \sim 0.046$), two concepts that are postulated to frame some observational datas into a consistent theory, but without a precise characterization in terms of current particle theories. In this chapter I will consider the reasons that lead to the introduction of the concept of Dark Matter (hereafter DM).

DM have been introduced to explain evidence of "missing mass" in the universe. This phenomenon was first detected by F. Zwicky [96] in 1933, through the observation of the Coma cluster of galaxies: he expressed the "missing mass problem" estimating the total mass of the cluster based on the motions of galaxies near its edge (using virial theorem) and comparing it to the mass found by the number of galaxies and total brightness of the cluster: there was about 400 times more estimated mass than was visually observable. Then, in the late 1960s and early 1970s, V. Rubin measured the velocity curve of edge-on spiral galaxies and showed that most stars in spiral galaxies orbit at roughly the same speed, which implied that their mass densities were uniform well beyond the locations with most of the stars. This result suggests that either Newtonian gravity does not apply universally or that upwards of 50% of the mass of galaxies was contained in the relatively dark galactic halo. Since those years, other observational evidences for DM has been collected over the decades through the analysis of many phenomena (CMB anisotropies, gravitational lenses, large scale structure of the universe), theories about the nature of DM were proposed and experiments planned to solve one of the most

challenging issue of modern astrophysics.

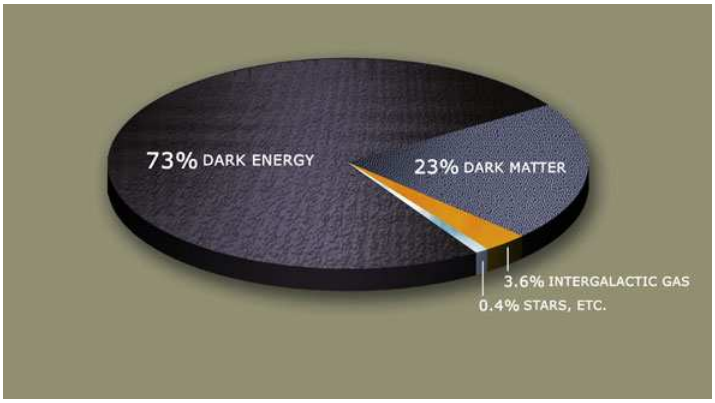

Figure 1.1: An intuitive representation of the contributions to the total energy of the universe.

1.1 The indirect clues

1.1.1 Galactic rotation curves

From the rotation curve of a spiral galaxy, i.e. the rotational velocity $v(r)$ of stars and gas as a function of galactocentric radius r, one can infer the mass of the galaxy $M(r)$ enclosed in that radius. If the visible stars and gas provided all the mass in the galaxy, one would expect that the rotation curve should decline at radii larger than the extent of stellar disk according to the keplerian relation $v^2 = \frac{GM}{r}$. Instead, one observes that $v(r)$ remains constant out to much larger radii, indicating that the galaxies must contain far more matter that contributed by the stars and gas. These mesurements, applied in the Milky Way, are important also for fixing the local DM density, relevant for direct detection of DM.

1.1.2 Galaxy Clusters

There are at least three ways to show the discrepancy between the mass of visible matter and the total mass inside a cluster of galaxies.

Lensing

The gravitational field of the clusters curves the space around it, so the light rays emitted from objects behind the cluster travel along curved paths (gravitational lensing). If the lensing is strong enough, there are multiple paths from the same object that arrive

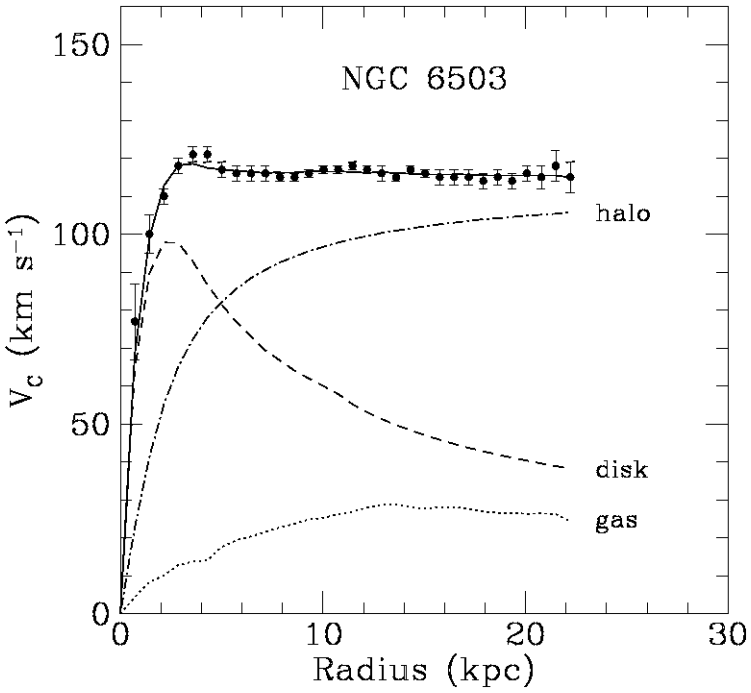

Figure 1.2: Rotation curve of NGC 6503. The dotted, dashed and dash-dotted lines are the contributions of gas, disk and dark matter, respectively. From [1]

.

at the location of the telescope. Because the light from different sides of the same galaxy travels along different paths, the images of strongly lensed sources are distorded into arcs. For a lensing cluster with total mass M and impact parameter d the deflection angle is of order $\alpha \sim \left(\frac{GM}{dc^2}\right)^{1/2}$. From the measurements of the deflection angle and impact parameter, one can infer that the total mass of a cluster is much larger than the observed baryonic mass. Another way to show that, in a cluster, $M_{total} \gg M_{baryons}$ consists in using the equation of hydrostatic equilibrium: $\frac{\mathrm{d}p}{\mathrm{d}r} = -G\frac{M(r)\rho(r)}{r^2}$, where the pressure $p(r)$ is measured combining data from the temperature $T(r)$ (inferred using the strenght of the emission lines) and from the electron number density $n_e(r)$ (inferred using x-ray luminosity).

Dynamics

The virial theorem allows to obtain the mass of a cluster through the relation: $v^2(r) = \frac{GM(r)}{r}$. Once again: $M_{total} \gg M_{baryons}$.

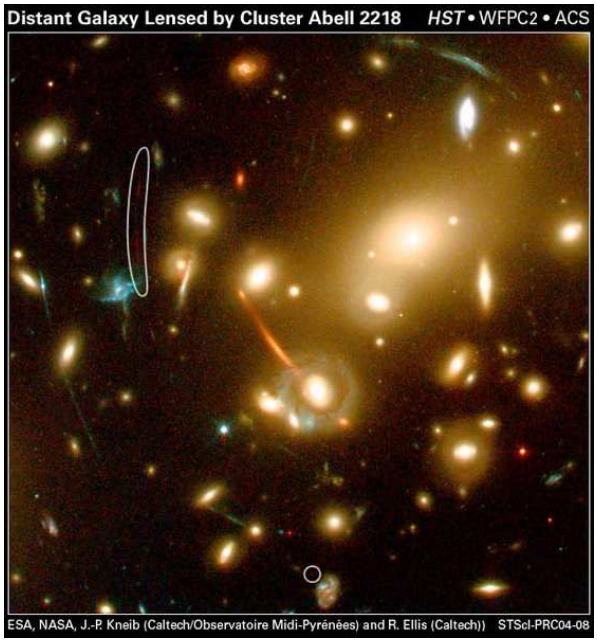

Figure 1.3: Distant galaxy lensed by Abell cluster 2218. Credit: NASA, Andrew Fruchter and the ERO team.

1.1.3 CMB and LSS

The most compelling hints about the non-baryonic nature of DM are provided by the measurements of the Cosmic Microwave Background (CMB) and by the Large Scale Structure (LSS) of the universe. Tuning the parameters on which theoretical prediction are based, in order to fit the angular power spectrum of CMB temperature anisotropies, and constraining the results with the datas from LSS, one can obtain $\Omega_{matter}h^2 = 0.133 \pm 0.006$ and $\Omega_{baryons}h^2 = 0.0227 \pm 0.0006$ (Dunkley et al. 2009 [18]).

1.2 The direct investigation

1.2.1 Properties of Dark Matter

Althought it is not clear which is the particle that people call DM, there are some constrains that restrict the field of investigation:

- DM have no interactions with photons (or extremely weak interactions), otherwise it might contribute to the dimming of quasar, creating absorption lines or emitting photons.

- Self-interaction should be small, otherwise it would suffer gravotherma catastro-

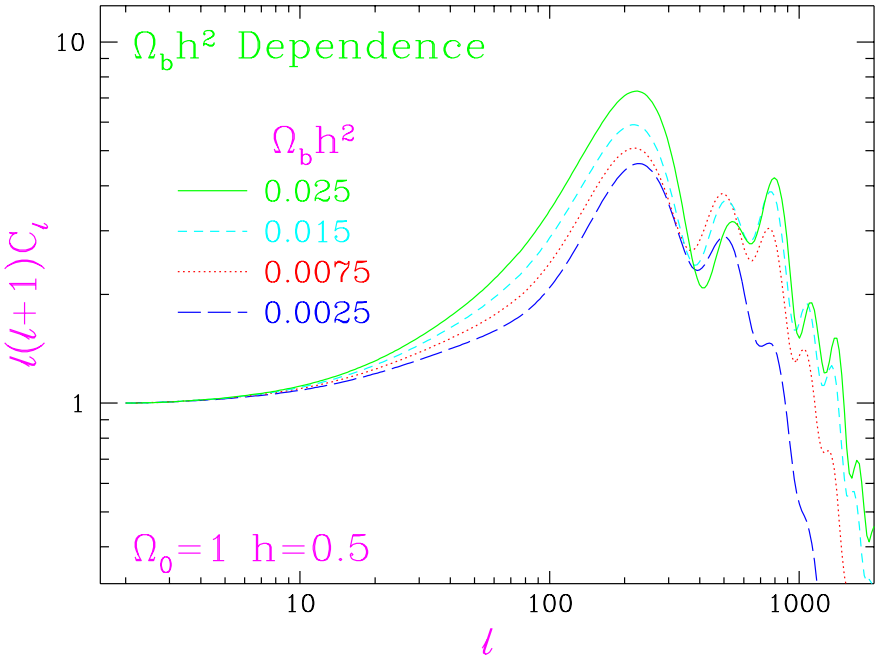

Figure 1.4: An example of the dependence on Ω_{baryon} of the CMB-angular spectrum. From Wayne Hu's webpage [32]

phe: in binary interactions of two DM particles, one can get ejected from the halo, while the other moves to a lower energy state at smaller radius: in this way much of the halo evaporate and the remaining shrinks.

- Interactions with baryons must be weak.
- DM cannot be made up of standard model particles, since most leptons and baryons are charged; the only potentially suitable standard model particle is the neutrino, but it cannot be DM because of Gunn-Tremaine bound.

The most attractive DM-candidates are weak-interacting massive particles (*WIMPs*) that interact, besides through gravity, through weak nuclear force, and that has a large mass compared to standard particles; so they are slow, cold and clumpy: *WIMPs* are considered one of the main candidates for "cold dark matter".[1]

1.2.2 Detection of Dark Datter

There are many experiments to attempt to detect *WIMPs*, both directly and indirectly. Among the direct searches, the majority of present experiments use one of two

[1] Cold means that it has decoupled from the radiation in a non relativistic regime.

detector technologies. The first the cryogenic detector, operating at temperatures below 100mK, detect the heat produced when a particle hits an atom in a crystal matrix of an absorber such as germanium. The second is the noble liquid detector that sees the flash of scintillation light produced by a particle collision in liquid xenon or argon. Cryogenic detector experiments include: CDMS (Cryogenic Dark Matter Search), CRESST (Cryogenic Rare Event Search with Superconducting Thermometers), EDELWEISS (Expérience pour DEtecter Les Wimps En Site Souterrain), and EURECA (European Underground Rare Event Calorimeter Array). Noble liquid experiments include ZEPLIN, XENON, ArDM and LUX (Large Underground Xenon Detector). Other direct dark matter experiments include DAMA/NaI, DAMA/LIBRA, DRIFT (Directional Recoil Identification From Tracks), and PICASSO (Project in Canada to Search for Supersymmetric Objects). Indirect detection experiments search for the products of WIMP annihilation. If WIMPs are majorana particles (the particle and antiparticle are the same) then two WIMPs colliding would annihilate to produce gamma rays, and particle-antiparticle pairs. This could produce a significant number of gamma rays, antiprotons or positrons in the galactic halo, that can be measured by EGRET (Energetic Gamma Ray Experiment Telescope) or by GLAST (Gamma-ray Large Area Space Telescope).

1.2.3 Possibility of Baryonic Dark Matter

Although it's most unlike that all the DM that make $\Omega_{matter} \sim 0.3$ is made up with baryons, there are some hints for choosing them as plausible candidates for galactic halo DM. The strongest argument for the existence of baryonic DM comes from primordial nucleosyntesis: the results for ^4He, ^3He, ^2H, ^7Li abundances give $\Omega_{baryon}h^2 \sim 0.0125$; since the contribution of luminous baryons is $\Omega^{lum}_{baryon}h^2 \sim 0.007$, we need the presence of dark baryons. If there exist baryonic DM, it could take these forms, of decreasing plausibility:

- stellar mass objects: they could be brown dwarfs ($10^{-3} \div 0.08 M_\odot$), white dwarfs ($0.4 \div 1.4 M_\odot$), neutron stars ($1.4 \div 2 M_\odot$), stellar relict black holes from ordinary massive stars ($2 \div 10 M_\odot$), black holes from supermassive stars ($100 \div 10^4 M_\odot$)
- Diffuse dense clouds of cold hydrogen.
- Exotica, including primordial black holes, and nuggets of strange matter.

During the early 90's, these objects were called *MACHOs*, massive astrophysical compact halo objects, a term chosen whimsically, by contrast with *WIMPs*. *MACHOs* were detected through microlensing analysis: when they pass in front of or nearly in front of a star they bend the light, causing the star to appear brighter.

1.2.4 What is the Dark Matter made of?

There are a lot of candidates for non-baryonic DM, but the most appealing, at the moment, is the neutralino with a mass of $\sim 100GeV$. For the rest of this thesis two things will be enough to know about the nature of DM, in order to develop a model for structure formation: the type of interaction between DM particles and between DM and baryons (i.e. the laws of gravity), and the fact that there are hints that the DM is "cold" , i.e. it has decoupled from the radiation in a non relativistic regime.

Chapter 2

Structure Formation in a ΛCDM Universe

2.1 Cosmological Reference Paradigm: the Hot Big Bang

Both the analytical calculations and the numerical simulations shown in this thesis are based on a theoretical framework that follows the history of the universe from the Big Bang to the formation of the structures: a cosmology built on the concordance ΛCDM model, with parameters defined by observational results, is used.

The observation of the cosmological redshift phenomenum, through the recession of the distant galaxies with a speed proportional to the distance (Hubble law), contributed to the development of a cosmological model based on the idea of *Big Bang*, the space-time singularity at time $t = 0$, after which the universe has evolved expanding in an adiabatic way. The analysis of the light-element abundances plus the standard model of particles allow to fix a series of eras characterized by typical temperatures, by the presence of typical particles and by their densities. The adjective "hot" comes from the cosmological origin of the radiative component.

2.1.1 From Cosmological Principle to Evolution of the Hubble Parameter

The cosmological redshift is interpreted as a consequence of the expansion of the universe that is predicted by the general relativity (GR) theory, used to describe the gravitational force that is the main interaction when large scales are considered. In order to introduce the gravitational force into the description of the space-time, GR uses an expression called metric that identify the space-time interval:

$$\mathrm{d}s^2 = g_{ij}\mathrm{d}x^i\mathrm{d}x^j \quad , \tag{2.1}$$

the *metric tensor* g_{ij} describes the properties of the space-time and x^k $(k = 0, 1, 2, 3,)$ are the space-time coordinates. It is possible to simplify the metric using two properties of the large scale structure of the universe ($> 100Mpc$) that come from the observation of the small anisotropies of the Cosmic Microwave Background and from the wide field surveys: the omogeneity and the isotropy. The new expression is:

$$\mathrm{d}s^2 = (c\mathrm{d}t)^2 - a(t)^2 \left[\frac{\mathrm{d}r^2}{1 - Kr^2} + r^2(\mathrm{d}\theta^2 + sin^2\theta \mathrm{d}\phi^2)\right] \quad , \tag{2.2}$$

$a(t)$ is the expansion factor as a function of proper time t; r, θ, ϕ are polar-spherical comoving coordinates (i.e. they are defined in a reference frame that is bound to the expansion of the universe); K is the curvature parameter that admits three values: $-1, 0, 1$, that refer to an open, flat or closed universe.

It is possible to simplify also the Einstein's equations:

$$R_{ij} - \frac{1}{2} g_{ij} R = \frac{8\pi G}{c^4} T_{ij} \quad , \tag{2.3}$$

in which R_{ij} is the Ricci's tensor, R the scalar curvature, T_{ij} the energy-momentum tensor, G the gravitational constant and c the speed of light. For the time-time component:

$$\ddot{a} = -\frac{4\pi G}{3}\Big(\rho + \frac{3p}{c^2}\Big)a \quad , \tag{2.4}$$

and for the the space-space components:

$$a\ddot{a} + 2\dot{a}^2 + 2Kc^2 = 4\pi G\Big(\rho - \frac{p}{c^2}\Big)a^2 \quad , \tag{2.5}$$

from which:

$$\dot{a}^2 + Kc^2 = \frac{8\pi G}{3}\rho a^2 \quad , \tag{2.6}$$

where the expression of the energy-momentum tensor for macroscopic bodies is used:

$$T_{ij} = (p + \rho c^2)U_i U_j - p g_{ij} \quad ,$$

in which U_k is the 4-velocity, p the pressure and ρc^2 the energy density.

The equation (2.2) is called Robertson-Walker metric; (2.4) and (2.6) are the Friedmann equations, which are useful to obtain the equation for the evolution of the *Hubble parameter* H[1]:

$$H^2(t) = \left(\frac{\dot{a}}{a}\right)^2 = H_0^2 \left(\frac{a_0}{a}\right)^2 \left[\Omega_{0w}\left(\frac{a_0}{a}\right)^{1+3w} + (1 - \Omega_0 w)\right] \quad , \tag{2.7}$$

the subscript 0 refers to the present time; Ω_{0w} is the density parameter, defined as: $\Omega_{0w} = \frac{\rho_{0w}}{\rho_{0c}}$, where w relates the pressure to the energy density in the equation of state[2]

[1] The definition for the Hubble parameter is $H(t) = \frac{\dot{a}(t)}{a(t)}$.

[2] A radiative fluid has $w = \frac{1}{3}$, the dust has $w = 0$.

$p = w\rho c^2$; $\rho_{0c} = \frac{3H_0^2}{8\pi G}$ is the *critical density*.[3] The analysis of $a(t)$ shows that the GR predicts the expansion of the universe and, in the cases with $\rho_0 > \rho_{0c}$, predicts the collapse of it.

2.1.2 Thermal Evolution of the Universe

Going back in time, Friedmann's equations show that $a(t) \to 0$, and the temperature $T \to \infty$. However, there exist a typical energy for which the de Broglie wavelenght associated to a particle is less than its Schwarzchild's radius: in this regime, one can not use the classical approximation for the Friedmann equations anymore; this energy-threshold defines some associated quantities (called Planck-mass, Planck-lenght, Planck-temperature, ...), in particular the Planck-time ($t_p = 10^{-43}s$) is the time before which one can not consider the relativistic aspect and the quantistic one together, for a theoretical lack of knowledge.

From the Planck-time, the universe has evolved in an adiabatic way, so getting cold through the relation $T(t) \propto a^{-1}(t)$. The temperature of the universe, so its energetic characteristic, determines the presence of some particles and forces in different eras.

The era between t_p and $t \approx 10^{-5}$s is called the *transition phase era*, and it is characterized by the unify description of the fundamental forces (electromagnetic, weak and strong forces).

From $t \approx 10^{-5}$s ($T \approx 200 \div 300$MeV), there is the *adron era*, when *quarks* formed the adrons and the universe was filled by pions, protons, neutrons, antiprotons, antineutrons, leptons, antileptons e photons. The annihilation of the pions at $T \approx 130$MeV determines the beginning of the *lepton era*, that lasts untill $t \approx 10s$ ($T \approx 0.5$MeV) when electrons annihilated with positrons.

The radiative era followed, with the *cosmological nucleosynthesis*, at $T \approx 10^9$K.

The time when the radiation energy density was equal to the matter energy density is called *equivalence* and depends by Ω and H; the typical *redshift*[4] for the equivalence between radiation and dark matter is $z_{DMeq} \approx 10^4$.

At lower temperatures, the protons combine the electrons and form neutral hydrogen; when the ionized atoms are less that 50%, we have the *ricombination*, at $z_{rec} \approx 1500$. When the neutral atoms represent an high percentage of the total, the cross

[3] If $\rho_0 < \rho_{0c} \Rightarrow$ then $\Omega_0 < 1$ and $K = -1$, open universes;
if $\rho_0 > \rho_{0c} \Rightarrow$ than $\Omega_0 > 1$, $K = 1$, closed universes;
if $\rho_0 = \rho_{0c} \Rightarrow$ than $\Omega_0 = 1$, $K = 0$, flat universes.

[4] The redshift is defined by:

$$z = \frac{\lambda_0 - \lambda_e}{\lambda_e}$$

λ_0 is the wavelenght of an observed radiation that was emitted with a wavelenght λ_e at a previous time by a distant source.

section between barions and radiation becomes negligible: this happens at $z \approx 1000$. After this *decoupling*, matter and radiation evolve in a different "thermal way" following:

$$T_m = T_{0m}(1+z)^2 \quad , \tag{2.8}$$

for the matter and:

$$T_r = T_{0r}(1+z) \quad , \tag{2.9}$$

for the radiation; the subscript 0 refers to the present time.

The photons that first decoupled from the matter show a "last scattering surface" placed at $z \approx 1000$ and form a background of radiation that can be described by a black body with $T = 2.728 \pm 0.004$: for this reason it is called "cosmic microwave background"(CMB): this radiation appear similar observing it from all the line of sight in the sky and shows little anisotropies ($\sim 10^{-5}$).

2.2 ΛCDM Concordance Model

The *Lambda Cold Dark Matter concordance model* is based on the *Hot Big Bang* model, but introduces the presence of a *Dark Energy* using the parameter Λ, called *Cosmological Constant*; the model consider also that the most important component for the energy density of the matter is a certain type of *Cold Dark Matter*. Moreover, this model fixes the values of the parameters necessary for a quantitative description of the evolution of the universe.

2.2.1 Cosmological Constant

Some observational results, as those coming from supervonae Ia, show that, at low redshift, the cosmological expansion is accelerated. In order to introduce such phenomenum into the model, a term called "dark energy" was introduced in the Einstein equation, through the *cosmological constant* Λ:

$$R_{ij} - \frac{1}{2}g_{ij}R = \frac{8\pi G}{c^4}T_{ij} + \Lambda g_{ij}. \tag{2.10}$$

One can obtain the associated Friedmann's equations:

$$\ddot{a} = -\frac{4\pi G}{3}\Big(\rho + \frac{3p}{c^2}\Big)a + \frac{\Lambda c^2 a}{3} \tag{2.11}$$

and

$$\dot{a}^2 + Kc^2 = \frac{8\pi G}{3}\rho a^2 + \frac{\Lambda c^2 a^2}{3}. \tag{2.12}$$

Λ has an "anti-gravitational" effect, and it correspond to a fluid with equation of state $p = -\rho c^2$ ($w = -1$), i.e. a fluid with negative pressure that accelerates the expansion.

The density parameter associated to the dark energy is $\Omega_\Lambda = 0.7$.

2.2.2 Contribution of Matter

The total contribution to the energy density that comes from the matter is $\Omega_m \sim 0.3$; from the *CMB* datas and from the analysis of the deuterium, one can obtain the value $\Omega_b = 0.047$ associated to the barions: the stars contribut with an amount $\Omega_{star} \approx 0.005$, the remaining part comes from the diffuse hot gas.

2.2.3 Other Density Parameters

The density parameter associated to the radiation can be obtained by the temperature of the *CMB* ($T_{CMB} = 2.728 \mp 0.004^\circ K$):

$$\Omega_r \approx 2.3 \times 10^{-5} h^{-2}.$$

where $h = \frac{H}{100 Km/s/Mpc}$ and H is the Hubble parameter.

The contribution of neutrinos is negligible too:

$$\Omega_\nu \approx 10^{-5}.$$

2.2.4 Inflation and Power Spectrum

There exist some observations that are not explained by *Hot Big Bang* model: the *flatness problem* (i.e. the parameter density is ~ 1), the *horizon problem* (i.e. the *CMB* shows the same temperature in each direction of observation so diffent parts of the universe, that had never been in causal connection, have the same characteristic), the *monopole problem* (i.e. magnetic monopoles are not observed tough they are predicted by some theories). The solution of these discrepancies is the phenomenum called *inflation* that predicts an accelerated expansion in the first phase of the evolution of the universe: the results is that the geometry of the universe becomes flat, that different regions of the universe are in causal connection much before respect to the prediction of Friedman's models, that the magnetic monopoles are diluted.

The inflation gives also an explanation for the formation of the initial spectrum of perturbation and for its shape: during the infationary era, quantistic fluctuation of matter amplified and became relevant on macroscopic scales. The type of the power spectrum is a function of the inflationary model, but the *Harrison-Zel'dovich* result is always a good approximation: $P(k) \propto k$, where P is the spectrum and k is the characteristic scale of the perturbation in the Fourier space.

2.2.5 Parameter σ_8

Another parameter that characterized the concordance model is the *mass variance* on the scale $8h^{-1}$Mpc. The mass variance is obtained multiplying the power spectrum

by a window function, and integrating this product over all the wavenumbers k:

$$\sigma_M^2 = \frac{1}{(2\pi)^3} \int \mathrm{d}^3 P(k) \hat{W}^2(kR) \quad .$$

σ_8 is obtained putting $R = 8h^{-1}$Mpc into the expression of the window function. In this thesis $\sigma_8 = 0.9$ is assumed.

2.2.6 WMAP

The *Wilkinson Microwave Anisotropy Probe* provides from the year 2003 the values of the cosmological parameters for the concordance model. In Table 2.1 the "time evolution" of the results is shown; one can notice the increase in the precision of the various estimates.

parameter	WMAP 1 year	WMAP 3 years	WMAP 5 years
$H_0\ Kms^{-1}Mpc^{-1}$	72 ∓ 5	73.2 ∓ 3.2	70.5 ∓ 1.3
σ_8	0.9 ∓ 0.1	0.761 ∓ 0.049	0.812 ∓ 0.026
n	0.99 ∓ 0.04	0.958 ∓ 0.016	0.960 ∓ 0.013
$\Omega_m h^2$	0.14 ∓ 0.002	0.1277 ∓ 0.008	0.1358 ∓ 0.0037
$\Omega_b h^2$	0.024 ∓ 0.001	0.02229 ∓ 0.00073	0.02267 ∓ 0.00059

Table 2.1: Comparison among the values of the cosmological parameters provided by *WMAP* after 1 (Spergel et al., 2003 [74]), 3 (Spergel et al., 2007 [75]) and 5 (Komatsu et al., 2009 [39]) years of observation.

In this thesis these values for the parameters are considered: (H_0, σ_8, n, Ω_m, Ω_Λ) = ($70.5 Kms^{-1}Mpc^{-1}$, 0.9, 1.0, 0.3, 0.7)

2.3 Virialized Structure Formation

If one looks to scales smaller than $100Mpc$ he can observe that the matter gets organized into galaxies or clusters that arrange themselves into larger mono- and bi-dimensional structures, breacking the omogeneity and the isotropy that characterized the universe on larger scales. Following the standard scenario, cosmic structures are created by small matter fluctuations that grow because of self-gravity until the collapse. The first structures that arise from this process are the dark matter haloes, that aggregate in a heirarchical way for the gravitational collapse, reaching the virial equilibium between potential and kinetic energy. This dark matter structures create the potential wells into which the barions "fall"; the collisional gas convert its kinetic energy into thermal energy reaching the virial temperature; the consequent radiative loss is the cause

of the barion cooling and condensation of molecular clouds and stars. The standard scenario is considered into a cosmological context that uses the Cosmological Principle (Robertson-Walker metric) until the epoch of recombination; the universe is almost flat and dominated by the cold dark matter.

2.3.1 Jeans Theory

Jeans Scale

The linear regime of gravitational instability is well described by the Jeans theory that consider small density fluctuations over a uniform fluid, i.e. deviations from the mean density over all scales. If one consider a spherical overdense zone with radius R and mean density ρ, it has a mass $M \propto \rho R^3$; the typical velocity of the particles is v. One can make an account of the two processes that contribute to the evolution of the perturbation: the condensation, due to the gravity, and the diffusion, due to the particle motion. One can make this comparison with an esteem of the gravitational and kinetic energy E_p and E_k:

$$E_k \simeq \frac{Mv^2}{2} \tag{2.13}$$

$$E_p \simeq -\frac{GM^2}{R} \simeq -GM\rho R^2 \quad ; \tag{2.14}$$

otherwise, one can evaluate the gravitational force F_g and the pressure F_p:

$$F_p \simeq -\frac{v^2}{R} \tag{2.15}$$

$$F_g \simeq \frac{GM}{R^2} \simeq G\rho R \quad ; \tag{2.16}$$

otherwise one can determine the gravitational free-fall time scale τ_{ff} and the idrodynamic time scale τ_h (the time needed to balance the pressure and density differences):

$$\tau_h \simeq \frac{2R}{v} \tag{2.17}$$

$$\tau_{ff} \simeq \frac{1}{\sqrt{G\rho}}. \tag{2.18}$$

The equality in these quantities is reached for a particular lenght, called Jeans lenght, that determines a threshold for the size of the overdensity, under which the diffusion dominates, and over which the gravity dominates; one can find, from the energies:

$$R_J = v\sqrt{\frac{1}{2G\rho}} \quad ; \tag{2.19}$$

using the forces:

$$R_J = v\sqrt{\frac{1}{G\rho}} \quad ; \tag{2.20}$$

and using the time scales:

$$R_J = \frac{v}{2}\sqrt{\frac{1}{G\rho}}. \tag{2.21}$$

A density with radius $R > R_J$ can collapse under self gravity, if $R < R_J$, the perturbation is erased by diffusion effects.

Jeans Instability

Following the Jeans theory, one have to use the equations that relate the fields describing a fluid, in order to obtain the time evolution:

- the conservation of the mass:

$$\frac{\partial \rho}{\partial t} + \vec{\nabla} \cdot (\rho \vec{v}) = 0 \quad ; \tag{2.22}$$

- the Euler equation (ϕ is the gravitational potential):

$$\frac{\partial \vec{v}}{\partial t} + (\vec{v} \cdot \vec{\nabla})\vec{v} = -\frac{1}{\rho}\vec{\nabla} p - \vec{\nabla}\phi \quad ; \tag{2.23}$$

- the Poisson equation, that connects the gravitational field to its source:

$$\nabla^2 \phi = 4\pi G \rho \qquad ; \tag{2.24}$$

- the equation of state, that give the pressure as a function of the density and entropy (S):

$$p = p(\rho, S) \qquad ; \tag{2.25}$$

- the equation that describe the time evolution of the entropy for adiabatic systems:

$$\frac{\mathrm{d}S}{\mathrm{d}t} = 0. \tag{2.26}$$

The written equations characterize a classical approach to the time evolution of a perfect fluid, so one must consider only non-relativistic particles over scales less than the cosmological horizon[5].

In the proper reference frame, $\vec{r}$ is the space coordinate; in the comoving reference frame, we use $\vec{x}$; the two quantities are related by this relation: $\vec{r} = a\vec{x}$, a is the expansion

[5]Given a point O in the universe, the cosmological horizon is the surface that separates the space where a causal connection with O can exists (within a certain time t) from the zone where there is no causal connection. This surface is at a distance $R_H(t) = a(t) \int_0^t \frac{c\mathrm{d}t'}{a(t')}$ from O.

factor. The velocity of the fluid is the sum of the intrinsic velocity plus the the speed of expansion of the universe:

$$\vec{u} \equiv \frac{\mathrm{d}\vec{r}}{\mathrm{d}t} = \dot{a}\vec{x} + a\dot{\vec{x}} = H\vec{r} + \vec{v}. \tag{2.27}$$

One must express the fields as a sum of a non-perturbed part plus a perturbation: we consider the time evolution of the perturbation:

$$\begin{cases} \rho = \rho_b(1+\delta) \\ \vec{u} = H\vec{r} + \vec{v} \\ p = p_b + \delta p \\ \Phi = \Phi_0 + \phi \end{cases}$$

The subscript b refers to the non-perturbed part. δ is the "density fluctuation":

$$\delta(\vec{r},t) \equiv \frac{\rho(\vec{r},t) - \rho_b}{\rho_b} = \frac{\delta\rho(\vec{r},t)}{\rho_b}. \tag{2.28}$$

In the linear regime $\delta \ll 1$. When entered into the continuity, Euler, Poisson equations, the perturbations give these results in a comoving reference frame:

- continuity equation:
$$\frac{\partial}{\partial t}\delta\rho + \partial\rho_b a\vec{\nabla}\vec{v} + 3H\delta\rho = 0 \quad ; \tag{2.29}$$
- Euler equation:
$$\frac{\partial}{\partial t}\vec{v} + H\vec{v} = -\frac{v^2}{a}\vec{\nabla}\delta - \frac{1}{a}\vec{\nabla}\phi \quad ; \tag{2.30}$$
- Poisson equation:
$$\frac{1}{a^2}\nabla^2\phi = 4\pi G\rho_b\delta. \tag{2.31}$$

The system of these three equations has to be solved searching for a plane wave solution; one can obtain for δ_k[6]:

$$\ddot{\delta_k} + 2\frac{\dot{a}}{a}\dot{\delta_k} + \delta k\Big[\frac{k^2v^2}{a^2} - 4\pi G\rho_b\Big] = 0. \tag{2.32}$$

Using this equation one can follow the evolution of the perturbations through different epochs:

- before the equivalence, the most important contribution to the energy density is the radiation, so the main fluctuations are the radiation ones;

[6] $\delta(\vec{x},t) = \delta_k(t)\exp(i\vec{k}\vec{x})$, and analogous relations for ρ, v, ϕ.

- over scales greater than the horizon, both the dark matter and baryons fluctuations follow the radiation fluctuations, that are proportional to the square of the expansion factor:

$$\lambda > R_H : \qquad \delta_{DM} \propto \delta_B \propto \delta_R \propto a^2$$

- over scales smaller than the horizon, the Jeans scale of the baryon-radiation fluid is greater tha the horizon, so the associated perturbations oscillate; the dark matter perturbations are frozen by the Meszaros effect[7]:

$$\lambda < R_H : \qquad \delta_B \propto \delta_R \qquad \text{oscillate}$$

$$\delta_{DM} \qquad \text{almost constant}$$

- during the epoch between the equivalence and the recombination, the dominant energy density is the one provided by the dark matter, so the main fluctuations are the DM-fluctuations;

  - over scales greater than the horizon, both baryons and radiation fluctuations follow the DM-fluctuations, that are proportional to the expansion factor:

$$\lambda > R_H : \qquad \delta_R \propto \delta_B \propto \delta_{DM} \propto a$$

  - over scales smaller than the horizon and grater than the Jeans scale, the DM-fluctuations grow ($\propto a$), but the gravitational force is smaller than the radiation pressure, so the baryon-radiation fluid continues to oscillate:

$$R_J < \lambda < R_H : \qquad \delta_B \propto \delta_R \qquad \text{oscillate}$$

$$\delta_{DM} \propto a$$

  - over scales smaller than the Jeans scale, the DM-perturbations are erased by the free-streaming: the DM particles diffuse from over-dense regions to under-dens regions following the mean field of the universe instead of the local perturbation.

- after the recombination, the main energy density in the DM-energy density;

  - over scales greater than the horizon:

$$\lambda > R_H : \qquad \delta_R \propto \delta_B \propto \delta_{DM} \propto a$$

[7] The Meszaros effect shows that before the equivalence the time scale for the expansion is less than the time scale for a gravitational free-fall: the DM-perturbations are not able to grow within a Hubble-time.

- over scales smaller than the horizon and greater than the Jeans scale, the DM fluctuations grow $\propto a$; the radiation oscillates and decays; the baryons perturbations, decoupled from the radiations, grow to reach the amplitude of the DM-perturbations and to follow their trend.

$$R_J < \lambda < R_H : \qquad \delta_{DM} \propto a$$

$$\delta_R \quad \text{oscillate and decay}$$

$$\delta_B \quad \text{accelerate growth, then} \propto \delta_{DM}$$

- over scales smaller than the Jeans scale, the DM-perturbations are erased by the free-streaming and the baryons follow this trend. For cold dark matter, the DM-Jeans scale after the equivalence is very small, so this regime practically does not exist.

All these trends hold for universes with $\Omega_{m0} = 1$.

2.3.2 Statistics of Perturbations

Fair Sample Hypothesis

The standard paradigm about the formation of cosmic structures explains how they are consequences of the amplification (during the inflation) of quantum fluctuations so they are a product of a stochastic scalar field: the gravitational field. For this reason it is appropriate the use of a statistical tool for studying the properties of this field and, through the Poisson equation, the properties of the associated density fluctuation field:

$$\delta(\vec{x}) = \frac{\rho(\vec{x}) - \rho_b}{\rho_b}.$$

In order to re-express the Cosmological Principle from a statistic point of view, one can assume that $\delta(\vec{x})$ is a omogeneous and isotropic stochastic field, so that the observed universe can be seen as a statistical realization of that field.

Since the observation allow us to know only one realization of $\delta(\vec{x})$, in order to obtain its properties, one must consider a second hypotesis, the ergodic hypotesis that is: the averages of a stochastic field on a statistical set are equivalent to the spatial average of each realization.

Joining the ergodic hypothesis and the cosmological principle, one obtains the Fair Sample hypothesis.

Power Spectrum, Variance and Mass Variance

Within the standard model for the structure formation, the scalar field $\delta(\vec{x})$, is assumed to be stochastic, omogeneous, isotropic and gaussian with average equal to zero: only the variance can individualize it. The variance is defiined as:

$$\sigma^2 \equiv \left\langle \delta^2(\vec{x}) \right\rangle - \langle \delta(\vec{x}) \rangle^2 = \langle \delta^2(\vec{x}) \rangle \quad , \tag{2.33}$$

where $\langle \quad \rangle$ is the expected value of the stochastic field. Decomposing the fluctuation field into plane waves:

$$\delta(\vec{x}) = \frac{1}{(2\pi)^3} \int \hat{\delta}(\vec{k}) \exp(i\vec{k} \cdot \vec{x}) \mathrm{d}^3 k. \tag{2.34}$$

Using this integral, one expresses the variance as a function of $\hat{\delta}(\vec{k})$ into the Fourier space:

$$\sigma^2 = \frac{1}{(2\pi)^3 V_\infty} \int \mathrm{d}^3 \langle \delta(\vec{\hat{k}}) \delta^*(\vec{\hat{k}}) \rangle = \frac{1}{(2\pi)^3} \int \mathrm{d}^3 k P(k) \quad , \tag{2.35}$$

where δ^* is the conjugata component of δ and V_∞ is the volume of the universe. In the equation the definition of power spectrum $P(k)$ is used:

$$\langle \hat{\delta}(\vec{k}) \hat{\delta}^*(\vec{k}') \rangle \equiv (2\pi)^3 P(k) \delta_D^3(\vec{k} - \vec{k}') \quad , \tag{2.36}$$

where $\delta_D^3(k) = \frac{1}{(2\pi)^3} \int \exp(i\vec{k} \cdot \vec{x}) \mathrm{d}^3 x$ is the distribution Dirac delta function in 3 dimention. If $k = k'$, then $\delta_D^3(0) = V_\infty/(2\pi)^3$, so $\langle |\hat{\delta}(\vec{k})|^2 \rangle = V_\infty P(k)$.

Since $P(k) \propto |\hat{\delta}(\vec{k})|^2$, its value shows, for each k, the weight into the Fourier integral of the fluctuation over a scale k in order to build the generic fluctuation $\delta(\vec{x})$. The variance is the sum of the power of the fluctuation over all the scales k.

The written equation of the variance refers to an exact point into the density field; however, we need a quantity that refers to finite volumes; one can obtain it with a convolution of $\delta(\vec{x})$ with a window function W with a radius R in order to obtain the mean fluctuation density within a volume $V \propto R^3$:

$$\delta_M(\vec{x}) \equiv \frac{\delta M(\vec{x})}{\bar{M}} \quad , \tag{2.37}$$

where $\bar{M}$ is the mean mass within the considered volume. It is possible to obtain also the massa variance, i.e. the variance of the fluctuation field filtered over a scale R:

$$\sigma_M^2 \equiv \langle \delta_M^2 \rangle = \frac{1}{(2\pi)^3} \int \mathrm{d}^3 P(k) \hat{W}^2(kR) \quad , \tag{2.38}$$

where $\hat{W}(kR)$ is the Fourier transform of the window function.

The most common window functions used are:

- Top Hat:

$$W_{TH}(r) = \begin{cases} \frac{3}{4\pi R_T^3} & r < R_{TH}^3 \\ 0 & r > R_{TH}^3 \end{cases}$$

with a Fourier transform:

$$\hat{W}_{TH}(k) = \frac{3}{(kR_{TH})^3}[\sin(kR_{TH}) - (kR_{TH}\cos(kR_{TH}))]$$

- Gaussian:

$$W_G(r) = \frac{1}{(2\pi)^{3/2}R_G^3}\exp\Big(-\frac{r^2}{2R_G^2}\Big)$$

with a Fourier transform:

$$\hat{W}_G(k) = \exp\Big(-\frac{2k^2}{R_G^2}\Big)$$

- sharp k-space:

$$W_{Sk}(r) = \frac{1}{2\pi^2 r^3}[\sin\Big(\frac{r}{R_{Sk}}\Big) - \Big(\frac{r}{R_{Sk}}\Big)\cos\Big(\frac{r}{R_{Sk}}\Big)]$$

with a Fourier transform:

$$\hat{W}_{Sk}(k) = \begin{cases} 1 & k < \frac{1}{R_{Sk}} \\ 0 & k > \frac{1}{R_{Sk}} \end{cases}$$

Transfer Function

Consider scale-free initial power spectra[8]. Over scales greater than the horizon, the density fluctuations $\delta_k(t)$ evolve depending on the cosmological parameters and following an amplitude distribution that is a function of the shape of the primordial spectrum: the perturbations over the scales greater than the horizon are not affected by causal effects triggered by the microscopic physics. Increasing t, the horizon expands and allows bigger perturbations to have a causal relationship, so the primordial power spectrum is modified depending on the acting micro-physical process. If a perturbation is reached by the horizon before a_{eq}, it remains frozen because of Mezaros effect, until the equivalence; since the first perturbations reached by the horizon are over small scales, for those fluctuations the stagnation time is longer. If a fluctuation is big enough to be reached by the horizon after the equivalence, it is not affected by the stagnation. This different trend, that depends on the scale, modifies the shape of the primordial power spectrum: we want to know how the initial spectrum $P_{in}(k) \propto k^n$ becomes the

[8] A scale-free spectrum is a power law relation $P(k) \propto k^n$, with a constant logaritmic slope over all the scales.

processed spectrum $P_{fin}(k)$. We want to calculate the growth of a fluctuation $\delta(k)$ from an initial time, t_{in}, with a primordial power spectrum, to a final time, t_{fin}, between the equivalence and the recombination (after this epoch the DM-fluctuations are no more affected by microphyisical processes). Consider these two regimes:

1. if k determins $a_H < a_{eq}$, there is a growth until a_H, followed by a stagnation until the equivalence; the growth from t_{in} to the equivalence happens before been reached by the horizon scale:

$$\delta(k; a_{eq}) = \delta(k; a_{in}) \left(\frac{a_H}{a_{in}}\right)^2 \propto \delta(k; a_{in}) a_H^2 \quad , \tag{2.39}$$

2. if k determins $a_H > a_{eq}$, there is a growth of the perturbation until a_{eq}. In this case:

$$\delta(k; a_{eq}) = \delta(k; a_{in}) \left(\frac{a_{eq}}{a_{in}}\right)^2 \propto \delta(k; a_{in}) \quad , \tag{2.40}$$

   where $(a_{eq}/a_{in})^2$ is a constant.

To calculate the growth of $\delta(k)$ as a function of k, one must express a_H as a function of k. For $a_H < a_{eq}$ one obtains:

$$a_H \propto M^{1/3} \quad \Rightarrow \quad a_H^2 \propto M^{2/3}$$

and since $M \propto R^3 \propto k^{-3}$:

$$a_H^2 \propto k^{-2}. \tag{2.41}$$

Using this equation into (2.39) one obtains:

$$P_{fin}(k) \sim \delta^2(k; a_{eq}) \propto \delta^2(k; a_{in}) a_H^4 \sim P_{in}(k) k^{-4} \propto k^{n-4}. \tag{2.42}$$

Over small scales ($k \to \infty$), the initial spectrum is modified by a factor k^{-4}. If $a_H > a_{eq}$, from eq. (2.40):

$$P_{fin}(k) \sim \delta^2(k; a_{eq}) \propto \delta^2(k; a_{in}) \sim P_{in}(k) \propto k^n \quad , \tag{2.43}$$

i.e. over bigger scales ($k \to 0$), the initial spectrum remains the same until the equivalence. The transition between the two regimes happens for k similar to the scale of the cosmological horizon at the equivalence. If the universe is dominated by CDM with a Zel'dovich primordial spectrum (spectral index $n = 1$), the power $P_{fin}(k)\, \mathrm{d}^3k \propto k^3 P_{fin}(k)$ is an increasing function of k, and become a constant for $k \to \infty$:

$$\begin{aligned} k \to 0 \quad &\Rightarrow \quad k^3 P_{fin}(k) \propto k^{n+3} \propto k^4 \\ k \to \infty \quad &\Rightarrow \quad k^3 P_{fin}(k) \propto k^{n-4+3} \propto cost. \end{aligned}$$

The CDM model predicts a greater power on small scales implying a hierarchical clustering.

The modification of $P(k)$ can be expressed using a transfer function:

$$T(k; z_{fin}) \equiv \frac{\delta(k; z_{fin})}{\delta(k; z_{in})} \frac{D(z_{in})}{D(z_{fin})} \tag{2.44}$$

So:

$$P_{fin}(k) \propto \delta^2(k; z_{fin}) = P_{in}(k) T^2(k; z_{fin}) \Big[\frac{D(z_{fin})}{D(z_{in})}\Big]^2 = k^2 T^2(k) \Big[\frac{D(z_{fin})}{D(z_{in})}\Big]^2.$$

The transfer functions is a low-pass filter, so:

$$k \to 0 \quad \Rightarrow \quad T(k) \to 1$$

$$k \to \infty \quad \Rightarrow \quad T(k) \propto k^{-2} \to 0$$

2.3.3 Non-Linear Regimes

The Jeans theory holds if the density contrast remains in the linear regime: $\delta \ll 1$. However the perturbations evolve towards the unit value and the towards a strong non-linear regime: $\delta \gg 1$. So we need other theories besides the linear one. Here the spherical collapse model and the ellipsoidal collapse model are described.

Spherical Collapse

The idea is to follow a spherical non homogeneous perturbation with a radius R that contains a mass M; its evolution is:

$$\frac{\mathrm{d}^2 R}{\mathrm{d}t^2} = -\frac{GM}{R^2} \tag{2.45}$$

where:

$$M = \frac{4\pi R_i^3}{3} \bar{\rho}_i (1 + \delta_i) \quad \text{e} \quad \delta_i = \frac{\int_0^{R_i} 4\pi r^2 \delta_i(r)\, \mathrm{d}r}{4\pi R_i^3/3} \tag{2.46}$$

where $\bar{\rho}_i$ e δ_i are, respectively, the background density and the amplitude of the fluctuation at the initial time. The model require that the shells remains concentric during their evolution, so that the total mass would be constant; the equation (2.45) is the motion equation of the shells. The integral of (2.45) gives:

$$\frac{1}{2}\left(\frac{\mathrm{d}R}{\mathrm{d}t}\right)^2 - \frac{GM}{R} = cost = E. \tag{2.47}$$

If $E < 0$, then $\mathrm{d}R/\mathrm{d}t$ can change the sign: even if the perturbation begins to expand, it will collapse. If $\delta_i \ll 1$, then, at first approximation, one assumes that the

velocities are due only to the Hubble stream: $(\mathrm{d}R/\mathrm{d}t)_i \approx (\mathrm{d}(ax)/\mathrm{d}t)_i = x_i\,(\mathrm{d}a/\mathrm{d}t)_i = R_i\,[(\mathrm{d}a/\mathrm{d}t)\,/a]_i = H_i R_i$. The initial kinetic and potential energies are:

$$K_i = \frac{(H_i R_i)^2}{2} \quad \text{e} \quad W_i = -\frac{GM}{R_i} = -\Omega_i(1+\delta_i)\frac{(H_i R_i)^2}{2} \tag{2.48}$$

where, in the expression of W_i, the mass M (2.46) is insered, and $\Omega_i = \bar{\rho}_i/\rho_{c_i} = 8\pi G\bar{\rho}_i/3H_i^2$ is used. The total energy is:

$$E_i = K_i + W_i = K_i - K_i\Omega_i(1+\delta_i). \tag{2.49}$$

The collapse happens when $(1+\delta_i) > 1/\Omega_i$. If the perturbation is dense enough in respect to the background, after an initial expansion, and after reaching the turnaround dimension (maximun dimension), collapses. At the turnaround, the kinetic energy is null; for the conservation of energy:

$$E = -\frac{GM}{R_{max}} = -\frac{R_i}{R_{max}}K_i\Omega_i(1+\delta_i) = E_i = K_i\,[1-\Omega_i(1+\delta_i)] \tag{2.50}$$

so:

$$\frac{R_{max}}{R_i} = \frac{\Omega_i(1+\delta_i)}{\Omega_i(1+\delta_i)-1}. \tag{2.51}$$

When $\Omega_i = 1$, then: $R_{max}/R_i = (1+\delta_i)/\delta_i \approx 1/\delta_i$: the ratio between the radius at turnaround and the initial radius depends on δ_i, in the same way for each M. Shells slightly overdense have $R_{max} \gg R_i$ and need a longer time to collapse. After the turnaround, the perturbation collapse, there's a mixing of the shells and the structure virializes. Because of the virial equilibrium, $-W_{vir} = 2K_{vir}$; since the total energy $E = K_{vir} + W_{vir}$ must be equal to the total energy at turnaround:

$$E = K_{vir} + W_{vir} = W_{vir}/2 \approx -\frac{GM}{2R_{vir}} = -\frac{GM}{R_{max}} \quad , \tag{2.52}$$

so $R_{vir} \approx R_{max}/2$: at the virialization, the structure is 8 times denser respect to the turnaround.

The exact time evolution for each shell has a parametric solution:

$$\frac{R}{R_i} = A(1-\cos\theta) \quad \text{e} \quad \frac{t+T}{t_i} = B(\theta - \sin\theta) \tag{2.53}$$

where $(AR_i)^3 = GM\,(Bt_i)^2$ and θ changes within 2π. The evolution of an underdense region can be obtained changing $(\theta - \sin\theta)$ with $(\sinh\theta - \theta)$ and $(1-\cos\theta)$ with $(\cosh\theta - 1)$. The turnaround has $\theta = \pi$, so A is obtained putting: $R_{max}/R_i = 2A$; B follows.

$$A = \frac{1+1/\delta_i}{2} \quad \text{e} \quad B = \frac{1+\delta_i}{2H_i t_i \Omega_i^{1/2}}\,[1+\delta_i - 1/\Omega_i]^{-3/2}\,. \tag{2.54}$$

T is small compared to t_i, so it can be ignored; if $\Omega_i = 1$:

$$R_i = R_i \frac{1 + 1/\delta_i}{2}(1 - \cos\theta_i)$$

so: $\theta_i^2 \approx 4\delta_i$. So:

$$H_i t_i \left(1 + T/t_i\right) = \frac{1 + \delta_i}{\delta_i^{3/2}} \frac{(\theta_i - \sin\theta_i)}{2} \quad \rightarrow \quad H_i t_i \left(1 + T/t_i\right) = \frac{2}{3}(1 + \delta_i)$$

from this equation one obtains: $T/t_i = \delta_i \ll 1$, so that T can be ignored.

We consider an Einstein-de Sitter universe (only dust, flat $\Omega = 1$, without cosmological constant, with $\bar{\rho}(t) = 1/\left(6\pi G t^2\right)$): the ratio between the mean density within the perturbation anche the background density evolves as:

$$\begin{aligned} 1 + \delta &= \frac{\bar{\rho}_i}{\bar{\rho}(t)} \left(\frac{R_i}{R}\right)^3 \approx \frac{(t/t_i)^2}{A^3(1 - \cos\theta)^3} = \\ &= \frac{B^2(\theta - \sin\theta)^2}{A^3(1 - \cos\theta)^3} = \frac{9(\theta - \sin\theta)^2}{2(1 - \cos\theta)^3}. \end{aligned} \tag{2.55}$$

At $t \approx t_i$:

$$\delta \approx \frac{3\theta^2}{20} \approx \frac{3}{20}\left(\frac{6t}{B}\right)^{2/3} \approx \frac{3}{5}\delta_i \left(\frac{t}{t_i}\right)^{2/3}. \tag{2.56}$$

At *turnaround* ($\theta = \pi$) the density respect to the background is:

$$1 + \delta_{max} = \frac{9\pi^2}{16} \approx 5.55. \tag{2.57}$$

Since $\delta > 1$, the object is strongly non linear. Altought formally $\delta \rightarrow \infty$, when $\theta \rightarrow 2\pi$, the object virializes with a finite radius. These relations hold: $R_{vir} \approx R_{max}/2$; and if $t_{vir} = t(\theta = 2\pi)$, then $t_{vir} = 2t_{max}$. With $\Omega = 1$, the universe expands $2^{2/3}$ times between t_{max} and t_{vir}, decreasing its density by a factor 4. At virialization, the density compared to the background is:

$$1 + \delta_{vir} = \frac{9\pi^2}{16}\left(\frac{R_{max}}{R_{vir}}\right)^3 \left(\frac{\bar{\rho}_{max}}{\bar{\rho}_{vir}}\right) = \frac{9\pi^2}{16} \cdot 8 \cdot 4 \approx 178. \tag{2.58}$$

So the virialized objects have the same densities in spite of different masses.

The prediction coming from the linear theory about the value of the density is much less; in fact, using (2.56) and defining:

$$\delta_L = \frac{3}{5}\delta_i \left(\frac{t}{t_i}\right)^{2/3} = \frac{3}{5}\left(\frac{3}{4}\right)^{2/3}(\theta - \sin\theta)^{2/3} \quad , \tag{2.59}$$

where the subscript L refers to the linear regime, one obtains at the turnaround:

$$\delta_L = \frac{3}{5}\left(\frac{3\pi}{4}\right)^{2/3} = 1.062. \tag{2.60}$$

The linear theory gives a lower esteem of the overdensity, and this gap is greater toward the collapse. The predicted linear overdesity for a virialized object has a significant interest for models that exploit the initial density fluctuations in order to describe the evolution of the non linear custering; the value of this critical threshold for the collapse is:

$$\delta_{sc} = \frac{3}{5}\left(\frac{3\pi}{2}\right)^{2/3} = 1.68647 \tag{2.61}$$

where the subscript sc shows that this value is derived into the spherical model. Here the value of δ_{sc} is obtained for an Einstein-de Sitter universe. For a ΛCDM universe (with $\Omega_m = 0.3$; $\Omega_\Lambda = 0.7$) the critical threshold for the collapse is $\delta_{sc} = 1.675529$.

Ellipsoidal Collapse

Numerical simulations show that the spherical collapse model is not the best approximation for describe the formation of cosmic structures. For example: the mass function obtained with the spherical model overestimates the number of low mass objects and underestimates the number of high mass structures. A more precise model is the ellipsoidal model that is more refined and takes into account a higher degree of complexity for the structures. From a priori point of view, one can predict that the spherical perturbation is a realistic approximation for masses a little greater than the Jeans mass, in a regime where the pressure and dissipative effects drive to spherical condensations in which the self-gravity is supported by the internal pressure. However, at the equivalence, it is unlikely that all the perturbations are spherical because this configuration would be unstable when there are non radial motions.

The ellipsoidal collapse model introduces the necessary geometrical complexity, describing omogeneous and triaxial regions in an uniform background: the perturbations would evolve in omogeneous ellipsoids. In this context, the tidal forces affect the collapse substantially.

White & Silk Model White and Silk developed this model in the 1979 [91] describing the growth and the collapse of omogeneous ellipsoidal perturbations in a uniform and expanding background; they don't take into account the tidal forces created by near objects. The homogeneity can seem to be a forcing because every proto-halo, when begins to free itself from the expansion, shows a strong coarsesness, due to the substructures already viriaized inside it; however it is possible that viscous effects can smooth the fluctuations over scales like $10^{12} \div 10^{13} M_\odot$.

The gravitational potential within an uniform ellipsoid is:

$$V_e = -\pi G \rho_e \sum_{i=1}^{3} \alpha_i x_i^2 \quad , \tag{2.62}$$

where ρ_e is the density of the ellipsoid; the coordinate axis coincide with the principal axis of inertia and V_e is equal to zero in the origin. They define the coefficients α_i:

$$\alpha_i(\frac{a_1}{a_3}, \frac{a_2}{a_3}) = a_1 a_2 a_3 \int_0^\infty (a_i + \lambda)^{-1} \prod_{j=1}^{3} (a_j + \lambda)^{-1/2} \mathrm{d}\lambda \quad , \tag{2.63}$$

where a_i are the semi-axis in comoving coordinates; they assume $a_1 \leq a_2 \leq a_3$. Putting (2.62) into the Poisson equation (2.24) they get:

$$\sum_i \alpha_i = 2. \tag{2.64}$$

The background sourronding the perturbation is a homogeneous sphere with density ρ_b; the associated potential is:

$$V_b = -\frac{2}{3}\pi G \rho_b \sum_{i=1}^{3} x_i^2. \tag{2.65}$$

The sphere is put in the coordinate origin where the potential $V_b = 0$. The total potential of a homogeneous perturbation in a non-perturbed universe is:

$$\begin{aligned} V &= -\pi G \sum_i [(\rho_e - \rho_b)\alpha_i + \frac{2}{3}\rho_b] x_i^2 = \\ &= -\pi G \sum_i [\alpha_i \rho_e + \Big(\frac{2}{3} - \alpha_i\Big)\rho_b] x_i^2. \end{aligned} \tag{2.66}$$

In order to obtain the motion equations starting from the potential equation, one assumes that the region outside the background sphere is uniform and that the external density can be calculated using Friedmann equations. The quadratic form of the potential and the uniform ρ_b allow the fluctuation to evolve through homogeneous ellipsoids: the velocity field remains linear. The evolution of the perturbation follows these equations:

$$\begin{cases} \frac{\mathrm{d}^2 a_i}{\mathrm{d}t^2} = -2\pi G\Big[\alpha_i \rho_e + \Big(\frac{2}{3} - \alpha_i\Big)\rho_b\Big] \\ \frac{\mathrm{d}^2 R_b}{\mathrm{d}t^2} = -\frac{4\pi}{3} G \rho_b R_b \\ \rho_e a_1 a_2 a_3 = cost \\ \rho_b R_b^3 = cost \end{cases} \tag{2.67}$$

where R_b is the a scale factor of the universe. The equations (2.67) must be integrated untill the minor axis becomes null and the structure is called pancake.

Assuming that the α_i's do not depend on time and that $\rho_e a_i$ and $\rho_b a_i$ have the same time evolution, an approximation to the first equation of the system is obtained:

$$\frac{\mathrm{d}^2 a_i}{\mathrm{d}t^2} = \Big[\frac{3}{2}\alpha_i(t_0)\frac{\mathrm{d}^2 R_e}{\mathrm{d}t^2} + \Big(1 - \frac{3}{2}\alpha_i(t_0)\Big)\frac{\mathrm{d}^2 R_b}{\mathrm{d}t^2}\Big]\alpha_i(t_0) \quad , \tag{2.68}$$

where t_0 is the initial time and R_e is the scale factor of a universe with initial density $\rho_e(t_0)$. The integration of (2.68) gives:

$$\begin{aligned} \frac{a_i(t)}{a_i(t_0)} &= \frac{3}{2}\alpha_i(t_0)R_e(t) + \Big(1 - \frac{3}{2\alpha_i(t_0)}\Big)R_b(t) = \\ &= R_b(t) - \frac{3}{2}\alpha_i(t_0)[R_b(t) - R_e(t)]. \end{aligned} \tag{2.69}$$

These equations describe the exact evolution of a spherical perturbation and are a good approximation to the ellipsoidal evolution.

One can obtain the solution of the system (2.67) through a numerical integration. The results show that the time for the collapse decreases if the eccentricity grows; moreover the kinematic properties of the collapsed ellipsoid depend, besides on the initial shape of the perturbation, on the density of the universe. The axial ratios depend on time through:

$$\frac{a_2(t_c)}{a_3(t_c)} \approx \frac{a_2(t_0) - a_1(T_0)}{a_3(t_0) - a_1(T_0)} \quad , \tag{2.70}$$

where t_c is found putting $a_1(t_c) = 0$.

The White and Silk approach allows to determine a relation between the initial perturbation and the final one, and the kinematic properties of the collapsed object. Although the tidal forces are neglected, this model gives a correct qualitative view of the proto-structure formation.

Eisenstein and Loeb Model The model [19] follows, analitically, the non linear collapse of aspheric regions in a gaussian primordial field of perturbations. The perturbations are described as homogeneous triaxial ellipsoids that are subject to their own gravitational field and to an external tidal tensor: this is the news feature respect to other older models. The initial perturbation is generated in a spherical volume around a density peak; the collapse is followed choosing a triaxial ellipsoid with mass equal to the mass of the spherical region, with the same overdensity and with the quadrupole momentum equal to the one of the initial fluctuation. The tidal tensor is originated by the external field and is calculated drawing spherical radial shells around the peak. This mass distribution plays tidal torsions on the object that begins to rotate. Using the equation of motion one can analyze the linear regime of the initial density field and, through an integration, the virialization can be described. It is also possible to determine some statistical properties of the virialized objects (shapes, orientations, angolar momentum) by creating several realizations of the initial field. With this model, one can see that the geometry of the collapse is driven by the tidal forces rather than by the initial anisotropy of the fluctuation.

Bond and Myers Model The model [8] considers both the non-linear internal dynamic evolution of the structures, and the slow external evolution of the virialized structures, following an approach that is the generalization of the peak theory and of the Press-Schechter method. The proto-structure is identified by a local density peak, filtered over a scale R_f: $\delta_f(\vec{r},t;R_f)$. In the local peaks, the gradient $\nabla_i\delta_f$ is equal to zero, and the tensor of the second derivatives, $\nabla_i\nabla_j\delta_f$ is less than zero. $\nabla_i\delta_f$ and $\nabla_i\nabla_j\delta_f$ determine the central properties of the peak; the dynamic of the system is realated to the displacement $\vec{\psi}(\vec{r})$ around the peak. The displacement field is decomposed into a part filtered over a large scale (*background*) and a part that represents the fluctuations of the displacement field, that are statistically indipendent from the background: $\psi = \psi_b + \psi_f$. Around the peak, the field ψ_b is identified by the displacement of the peak and by the deformation tensor:

$$\vec{\psi}_{b,i} \approx \vec{\psi}_{pk,i} - \sum_j e_{pk,ij}(\vec{r} - \vec{r}_{pk})_i + \cdots \tag{2.71}$$

The deformation tensor is defined by:

$$e_{b,ij} \equiv -\frac{1}{2}\Big(\frac{\partial\psi_{b,i}}{\partial r_j} + \frac{\partial\psi_{b,j}}{\partial r_i}\Big)(\vec{r}) \quad ; \tag{2.72}$$

and:

$$e_{pk,ij} \equiv -e_{b,ij}(\vec{r}_{pk}). \tag{2.73}$$

The deformation tensor can be expressed as a function of its eigenvalues, that individualize its principal axis:

$$e^{ij}_{pk} = -\sum_{l=1}^{3} \lambda_l \hat{n}^i_l \hat{n}^j_l \quad ; \tag{2.74}$$

where $\hat{n}_l$ are unit vectors.

In order to describe the ellipsoidal perturbation, one can use three parameters: the ellipticity e, the prolateness p and the density contrast δ. The relations among these parameters and the eigenvalues of the tensor are:

$$\begin{cases} \lambda_1 = (\delta/3)(1 + 3e + p) \\ \lambda_2 = (\delta/3)(1 - 2p) \\ \lambda_3 = (\delta/3)(1 - 3e + p) \end{cases} \tag{2.75}$$

One can obtain:

$$\begin{cases} e = (\lambda_1 - \lambda_3)/(2\delta) \\ p = (\lambda_1 + \lambda_3 - 2\lambda_2)/(2\delta) \end{cases} \tag{2.76}$$

If $\lambda_1 \geq \lambda_2 \geq \lambda_3$, one can obtain the constrains: $e \geq 0$, $-e \leq p \leq e$. The overdensity of the filtered field, δ, coincides with the trace of the tensor:

$$\begin{aligned} \delta &= -e^i_{pk,i} = \\ &= [\vec{\nabla} \cdot \vec{\psi}_b](\vec{r}_{pk}) = \\ &= \lambda_1 + \lambda_2 + \lambda_3 \end{aligned} \tag{2.77}$$

The collapse begins with the first axis and the virialization happens when the third axis collapse.

Chapter 3

The Excursion Sets method

The excursion set formalism was introduced by Bond et al. (1991) [7] and was developed by Lacey and Cole (1993) [41]; they based their work on a model, written by Press and Schechter (1974) [58], that allows an analytic approach to the hierarchical merging history of the dark matter haloes. The first hypothesis of this approach is that the stochastic, homogeneous and isotropic field $\delta(\vec{x},t) = \delta(\vec{x},t_0)D(t)/D(t_0)$ is determined by small density fluctuations, $\delta \ll 1$, that can be treated with the linear regime theory; $D(t)$ is the linear growing factor of the perturbations, $\vec{x}$ is the comoving coordinate and t_0 is a reference time, e.g. the present time. The field $\delta(\vec{x},t)$ is set only by the power spectrum of the fluctuations $P(\vec{k},t)$. The linear regime holds until the amplitude of the fluctuations reaches the unit value; when this happens, the non-linear effects dominate and the region separetes from the expansion of the universe and collapses forming a virialized object. At this epoch, the density contrast foretold by the linear theory is $\delta_c \equiv \delta_{sc} = 1.675529$ for the concordance model.

It is possible to change the point of view on this linear evolution: one can transfer the time dependence from the δ-field to the critical threshold, by multiplying δ_c by $D(t_0)/D(t)$. This means to consider the linear fluctuation field $\delta(\vec{x}) \equiv \delta(\vec{x},t_0)$ at time t_0, and a critical threshold $\delta_c(t) = \delta_c\, D(t_0)/D(t)$ that decreases while the time t grows. The model wants that the infinitesimal mass element in $\vec{x}$ is part of a halo with mass greater or equal than M, at time t, if the linear fluctuation $\delta_f(\vec{x};R)$, centered on $\vec{x}$ and filtered over a sphere with radius $R \propto M^{1/3}$, is equal or greater than the threshold:

$$\vec{x} \in M \quad \Rightarrow \quad \delta_f(\vec{x};R) \geq \delta_c(t). \tag{3.1}$$

3.1 Brownian Motions

The density field $\delta_f(\vec{x};R)$, filtered over a scale R, is the convolution of $\delta(\vec{x})$ with a window function $W(\vec{x},R)$ with a tipical amplitude R. Using the Fourier transform:

$$\delta_f(\vec{x};R) = \frac{1}{2\pi^2}\int_0^\infty \hat{\delta}(k)\hat{W}(kR)k^2\,\mathrm{d}k \approx \frac{1}{2\pi^2}\int_0^{k_f} \hat{\delta}(k)k^2\,\mathrm{d}k \equiv \delta_f(\vec{x};k_f) \tag{3.2}$$

where $k_f \propto 1/R$ is the wave number related to the filtering radius R; considering the position $\vec{x}=0$, one can throw away the exponential. $\delta_f(\vec{x};R)$ is the sum over all the fluctuation with a plane wave shape and with $k \lesssim k_f$; the window function is a low-pass filter and removes the contribution of waves with $k \gtrsim k_f$. The filtering can be done using the mass instead of k_f; the mass variance over a scale k_f is:

$$\sigma_R^2 = \frac{1}{2\pi^2}\int_0^\infty P(k)\hat{W}^2(kR)k^2\,\mathrm{d}k \approx \frac{1}{2\pi^2}\int_0^{k_f} P(k)k^2\,\mathrm{d}k \equiv S(k_f) \quad ; \tag{3.3}$$

usually, $S(k_f)$ is a monotonic increasing function of k_f, so that $S(k_f=0)=0$ and $S(k_f\to\infty)\to\infty$.

Consider, for each point $\vec{x}$, the path in the 2-dim space $(S(k_f),\delta_f(\vec{x};k_f))$ drawn by the fluctuation δ_f centered in $\vec{x}$ and filtered over a scale corresponding to k_f. Each trajectory starts in $(S,\delta_f)=(0,0)$, that corresponds to a null fluctuation with an infinite window as a filter, and then moves away from the origin, following the matter distribution around the point $\vec{x}$.

If the window function is a Top Hat function in the Fourier space, then the contributions to the $\delta_f(\vec{x};k_f)$-field from different k are not correlated. In this case the trajectory is a Brownian motion in (S,δ_f), that can be described using a diffusion equation:

$$\frac{\partial Q}{\partial S} = \frac{1}{2}\frac{\partial^2 Q}{\partial \delta_f^2} \quad , \tag{3.4}$$

where $Q(\delta_f,S)$ is the probability distribution in the stochastic variable δ_f for trajectories that have a given $\sigma^2(k_f)=S$ value. For a free Brownian motion, the solution of this equation is a Gaussian distribution:

$$Q(\delta_f,S) = \frac{1}{\sqrt{2\pi S}}\exp\left(-\frac{\delta_f^2}{2S}\right). \tag{3.5}$$

This distribution shows, for each S, the numerical density of trajectories within the interval $[\delta_f,\delta_f+\mathrm{d}\delta_f]$.

3.2 From Trajectories to Haloes

The trajectories that, starting from the origin, reach the point $(S,\ \delta_f=\delta_c(t))$ are associated with fluid elements that belong to haloes with mass M at time t. For each

t a horizontal threshold $\delta_c(t)$ (called also barrier) is determined; this barrier can be crossed, for the first time, by a brownian path at a value S of the x-axis: this means that, at time t, the mass element related to this trajectory is part of a halo with mass $M(S)$. The relation between S and M is given by (3.3) through $k_f \propto 1/R \propto M^{-1/3}$. The request that the trajectory touches the threshold for the first time, is equivalent to consider the maximum filtering radius $R = R_{max}$ (i.e. the minimum k_f or S) for which the sphere with radius R_{max}, at time t, has an overdensity greater or equal to $\delta_c(t)$. Even if the random walk, after this crossing, comes back again under the barrier, the mass element is consider to be part of the biggest halo with mass $M(R_{max})$, because the region is collapsed over that scale. In order to calculate the mass function of the DM-haloes, i.e. the mass distribution of the virialized structures at various epochs t, one has to consider the various types of trajectories respect to the threshold $\delta_c(t)$ and to count them. Consider a scale k_0, corresponding to the variance S_0, and an epoch t. One can identify three kind of possible trajectories:

1. trajectories that crossed the barrier at $k_f < k_0$ and that are still above the threshold:

$$\delta_f(k) \geq \delta_c(t) \quad \forall k \in [k_f, k_0] \quad ; \tag{3.6}$$

2. trajectories that stay under the barrier at $k_f = k_0$, but that crossed it at a lower value of S:

$$\delta_f(k_0) < \delta_c(t) \quad \text{ma } \exists\ k_f < k_0 \text{ tale che: } \delta_f(k_f) > \delta_c(t) \quad ; \tag{3.7}$$

3. trajectories that did not cross the barrier:

$$\delta_f(k_f) < \delta_c(t) \quad \forall\ k_f \leq k_0. \tag{3.8}$$

A straightforward way to face the problem is to consider the type-3 paths, that correspond to fluid elemets in haloes with mass $M < M(S_0)$ at time t. To do it, one must subtract, from the total number of trajectories that are under the threshold, the type-2 paths.

Since the path is determined by adding indipendent Fourier modes, at every time a trajectory moves upward or downward with the same probability. So, every type-2 trajectory has a corresponding virtual one with the same probability that crosses the barrier at the same point $(S, \delta_c(t))$, but coming from higher values of y-axis: one can obtain it by reflecting the path before the first crossing respect to the axis $\delta_c(t)$. This virtual trajectory corresponds to a brownian walk starting from $(S, \delta_f) = (0, 2\delta_c(t))$ and satisfying the diffusion equation with the solution (3.5); note that the center of the

Gaussian must be shifted from 0 to $2\delta_c(t)$. So, the probability for type-2 paths is:

$$Q_1(\delta_f, S, \delta_c(t))\, \mathrm{d}\delta_f = \frac{1}{\sqrt{2\pi S}} \exp\left[-\frac{(\delta_f - 2\delta_c(t))^2}{2S}\right] \mathrm{d}\delta_f. \tag{3.9}$$

So, the probability for type-3 trajectories is:

$$\begin{aligned} Q_2(\delta_f, S, \delta_c(t))\, \mathrm{d}\delta_f &= [Q(\delta_f, S) - Q_1(\delta_f, S, \delta_c(t))]\, \mathrm{d}\delta_f \\ &= \frac{1}{\sqrt{2\pi S}} \left\{ \exp\left(-\frac{\delta_f^2}{2S}\right) - \exp\left[-\frac{(\delta_f - 2\delta_c(t))^2}{2S}\right] \right\} \mathrm{d}\delta_f \end{aligned} \tag{3.10}$$

Chandrasekhar (1943) shows that this is the solution of the diffusion equation of the

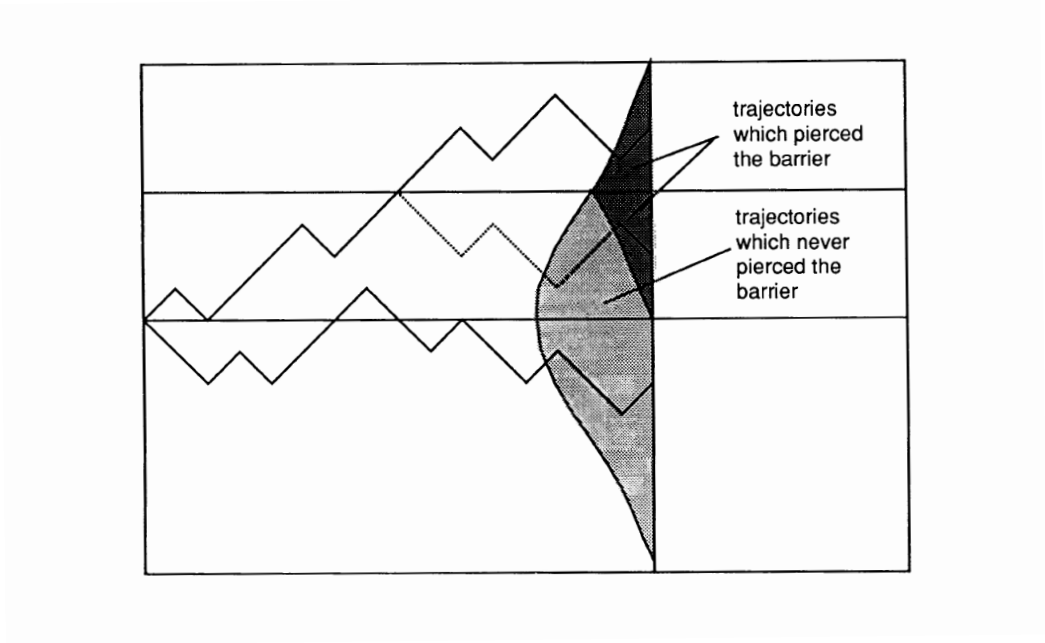

Figure 3.1: An example of stochastic paths and of the probabilities Q, Q_1 and Q_2 associated to the value of S (on the y-axis: $f_v \equiv \delta_c(t)$), from Bond et al. (1991).

stochastic trajectories, eq. (3.4); the boundary condition wants the absortion of the trajectories that cross the barrier. The fraction of paths that, within the time t, have not crossed yet the barrier $\delta_c(t)$, is the cumulative probability obtained with an integral from $-\infty$ to $\delta_c(t)$ of the previous expression:

$$P_2(S, \delta_c(t)) = \int_{-\infty}^{\delta_c(t)} Q_2(\delta_f, S, \delta_c(t))\, \mathrm{d}\delta_f. \tag{3.11}$$

The fraction of trajectories that have already crossed the barrier within t is the complementary set:

$$\bar{P}_2(S, \delta_c(t)) = 1 - P_2(S, \delta_c(t)) \quad ; \tag{3.12}$$

(3.12) is the numerical fraction of fluid element that are part of haloes with variance $< S$, at time t: this is the definition of cumulative mass function at time t, expressed in the S-variable:

$$\bar{P}_2(S, \delta_c(t)) = P(< S, t). \tag{3.13}$$

3.3 Useful distributions

Within the formalism of the excursion sets, following arguments similar to the ones used for the cumulative mass function, and adding some statistics, it is possible to obtain other distributions of interest. In the context of the spherical collapse, Bond et al. (1991) [7] and Lacey and Cole (1993) [41] found the differential mass function; Lacey and Cole [41] [42] considered also the progenitor and the descendant mass functions, besides the merger rate; Cavaliere et al. (1991) [12], Blain & Longair (1993) [6]), Sasaki (1994) [64], Kitayama and Suto (1996) [36], Percival and Miller [57] tried to obtain analytical equations for the creation and destruction rates.

3.3.1 Mass Function

The differential mass function (or global, or unconditional mass function) is the probability that, at time t, a fluid element is part of a halo with mass in the interval $[M, M + \mathrm{d}M]$. It can be obtained starting from the distribution of the trajectories that cross the barrier for the first time at t and at $[S, S + dS]$; this distribution derives from the cumulative mass function, by a derivative respect to the variance S:

$$\begin{aligned} p(S, \delta_c(t)) &\equiv \frac{\partial \bar{P}_2(S, \delta_c(t))}{\partial S} = -\frac{\partial P_2(S, \delta_c(t))}{\partial S} \\ &= -\frac{\partial}{\partial S} \int_{-\infty}^{\delta_c(t)} Q_2(\delta_f, S, \delta_c(t))\, \mathrm{d}\delta_f. \end{aligned} \tag{3.14}$$

Putting the derivative into the integral and exploiting the diffusion equation (3.4), one can substitute the derivative respect to S with the second derivative respecto to δ_f, obtaining:

$$p(S, \delta_c(t)) = -\frac{1}{2} \int_{-\infty}^{\delta_c(t)} \frac{\partial^2 Q_2}{\partial \delta_f^2}\, \mathrm{d}\delta_f = -\frac{1}{2} \frac{\partial Q_2}{\partial \delta_f}\bigg|_{-\infty}^{\delta_c(t)}. \tag{3.15}$$

With a derivative of eq. (3.10) one obtains:

$$\frac{\partial Q_2}{\partial \delta_f} = \frac{1}{\sqrt{2\pi S}} \left\{ \frac{-\delta_f}{S} \exp\left[-\frac{\delta_f^2}{2S}\right] + \frac{\delta_f - 2\delta_c(t)}{S} \exp\left[-\frac{(\delta_f - 2\delta_c(t))^2}{2S}\right] \right\}. \tag{3.16}$$

In $-\infty$, the function is null, because it contains terms like $\exp(-\infty)$. Only the term in $\delta_c(t)$ remains, so:

$$\begin{aligned} p(S,\delta_c(t)) \equiv \frac{\mathrm{d}f(S)}{\mathrm{d}S} &= -\frac{1}{2}\frac{\partial Q_2}{\partial \delta_f}\bigg|^{\delta_c(t)} = \frac{-1}{2\sqrt{2\pi S}}\frac{(-2\delta_c(t))}{S}\exp\left[-\frac{\delta_c^2(t)}{2S}\right] \\ &= \frac{\delta_c(t)}{\sqrt{2\pi}S^{3/2}}\exp\left[-\frac{\delta_c^2(t)}{2S}\right]. \end{aligned} \tag{3.17}$$

This is the fraction of mass in haloes with *variance* around S. The fraction of mass with *mass* around M is obtained changing the variable S into M and using the conservation of probability:

$$p(x)\,\mathrm{d}x = p(y)\,\mathrm{d}y \quad \Rightarrow \quad p(x) = p(y)\left|\frac{\mathrm{d}y}{\mathrm{d}x}\right| \tag{3.18}$$

so:

$$\frac{\mathrm{d}f(M)}{\mathrm{d}M} = \frac{\mathrm{d}f(S)}{\mathrm{d}S}\left|\frac{\mathrm{d}S}{\mathrm{d}M}\right|. \tag{3.19}$$

From,

$$\left|\frac{\mathrm{d}S}{\mathrm{d}M}\right| = \frac{S}{M}\left|\frac{\mathrm{d}\ln S}{\mathrm{d}\ln M}\right| = \frac{2S}{M}\left|\frac{\mathrm{d}\ln\sigma}{\mathrm{d}\ln M}\right| \tag{3.20}$$

one obtains:

$$\frac{\mathrm{d}f(M)}{\mathrm{d}M} = \left(\frac{2}{\pi}\right)^{1/2}\frac{\delta_c(t)}{M\sigma(k_f)}\left|\frac{\mathrm{d}\ln\sigma}{\mathrm{d}\ln M}\right|\exp\left[-\frac{\delta_c^2(t)}{2\sigma^2(k_f)}\right]. \tag{3.21}$$

The number of haloes with mass M in a volume V containing a total mass M_V is:

$$\frac{\mathrm{d}f(M)}{\mathrm{d}M}\frac{M_V}{M} \quad ; \tag{3.22}$$

considering a unit volume ($V = 1$ and $M_V = \rho_0$), one obtains the numerical density of haloes with mass:

$$\frac{\mathrm{d}n}{\mathrm{d}M}(M,t) = \frac{\mathrm{d}f(M)}{\mathrm{d}M}\frac{\rho_0}{M} = \left(\frac{2}{\pi}\right)^{1/2}\frac{\rho_0}{M^2}\frac{\delta_c(t)}{\sigma(k_f)}\left|\frac{\mathrm{d}\ln\sigma}{\mathrm{d}\ln M}\right|\exp\left[-\frac{\delta_c^2(t)}{2\sigma^2(k_f)}\right]. \tag{3.23}$$

This is the Press-Schechter mass function. It is possible and more useful re-write the global mass function eq. (3.23) in the variable $\nu = \delta_c(t)/\sigma(M)$ because in this way there is a degeneracy respct to the redshift, that means that the function has the same shape for each epoch:

$$\frac{\mathrm{d}f(\nu)}{\mathrm{d}\ln\nu} = \left(\frac{2}{\pi}\right)^{1/2}\nu\exp\left(-\frac{\nu^2}{2}\right). \tag{3.24}$$

3.3.2 Progenitor Mass Function

The results obtained with the excursion sets apprach, besides the mass function, are called extended Press-Schechter model. So far, the trajectories have been counted at a fixed time in order to obtain the global mass functions. However, a trajectory $\delta_f(S)$ can also describe the merging history of a particle throgh various times. The hierarchical clustering is described: to follow a given fluid element that, as time increases, is part of more massive haloes is the same as to follow a trajectory starting from great values of S and $\delta_c(t)$ and going toward the bottom and the left of the plot, Figure 3.3.2 pointing at the origin of the coordinate system. Since at a given time one assumes that a fluid element is included in a halo with the minimum value of S for which the associate trajectory crossed the δ-threshold, as time incrases (and as the threshold gets lower), the mass of the halo that owns that particle follow the trend given by the trajectory for type-1 trajectories, whereas it jumps toward left until it reaches the first upcrossing for type-2 trajectories; this is shown in Figure 3.3.2.

In the hierarchical clustering, this increase in mass is interpreted as the result of merging events among different haloes.

One can be interested in knowing how a given halo of a certain mass that exists at a certain epoch was splitted in other haloes at a previous times. The progenitor mass function is the distrubution of the haloes at a time t_1 that are constrained to being part of given halo at time $t_2 > t_1$. More precisely, using the correspondence between trajectories and fluid elements: the progenitor mass functions is the probability that a particle resides in an object of mass M_1 at redshift z_1 (it is easier to use the redshift instead of the time) provided that it will be part of an object with greater mass $M_2 > M_1$ at a later time or preavious redshift $z_2 < z_1$. The request that a halo with mass M_1 at t_1 will have a mass M_2 at t_2 corresponds to the selection of all the trajectories that pass through the 2 points $(S_1, \delta_c(t_1))$ e $(S_2, \delta_c(t_2))$ con $S_1 > S_2$ in the excursion sets diagram; in Figure 3.3, all the trajectories conditioned to pass through $(S_2, \delta_c(t_2))$ are shown. The conditional distribution $p(S_1, \delta_c(z_1)|S_2, \delta_c(z_2))$, is obtain from the equation (3.17), noticing that it corresponds to ask that the trajectories don't start from the point $(0, 0)$, but from $(S_2, \delta_c(t_2))$. It is enough to do the replacements $S \to (S_1 - S_2)$ e $\delta_c(t) \to (\delta_c(t_1) - \delta_c(t_2))$ into (3.17), and one can obtain:

$$p(S_1, \delta_c(t_1)|S_2, \delta_c(t_2)) = \frac{\mathrm{d}f}{\mathrm{d}S}(S_1, t_1|S_2, t_2) =$$
$$= \frac{\delta_c(t_1) - \delta_c(t_2)}{\sqrt{2\pi}(S_1 - S_2)^{3/2}} \exp\left[-\frac{(\delta_c(t_1) - \delta_c(t_2))^2}{2(S_1 - S_2)}\right]. \tag{3.25}$$

To write the distribution as a function of the mass, one can use the relation (3.18):

$$p(M_1, t_1|M_2, t_2) = p(S_1, t_1|S_2, t_2)\left|\frac{\mathrm{d}S_1}{\mathrm{d}M_1}\right| \quad ; \tag{3.26}$$

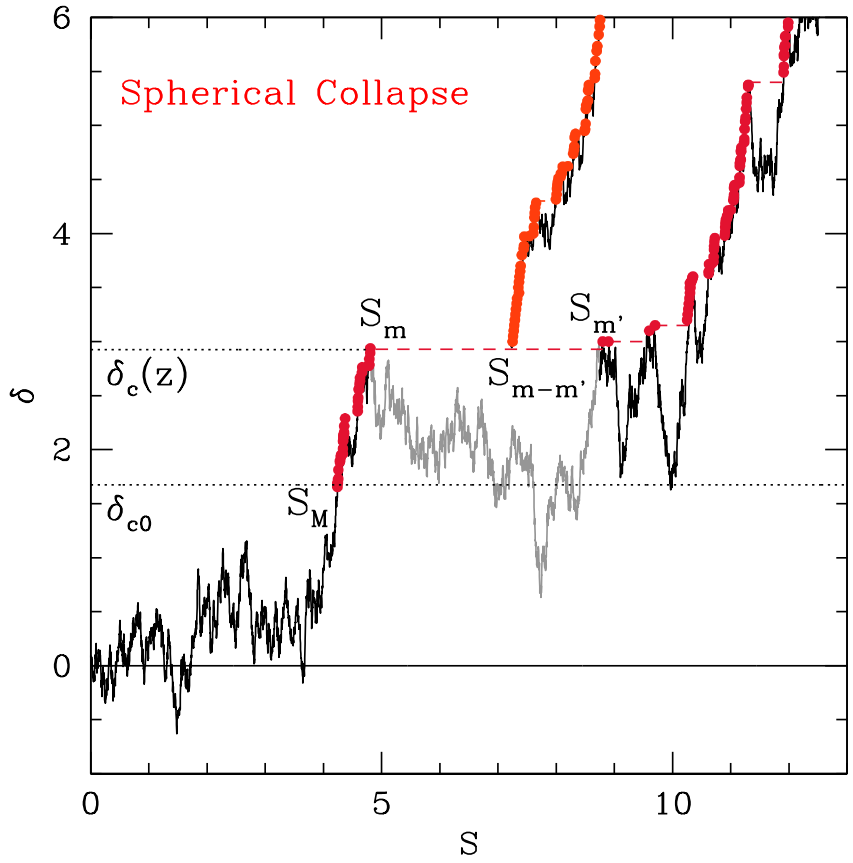

Figure 3.2: A random walk and its associated mass history. A merger $(m, m-M) \rightarrow M$ at redshift z is depicted by the $S_M \rightarrow S_m$ jump at height $\delta_c(z)$. Starting at $(S_{M-m}, \delta_c(z))$, there is a connection between the branch and the associated $(M-m)$ "sibling". From Moreno et al. 2008 [51]

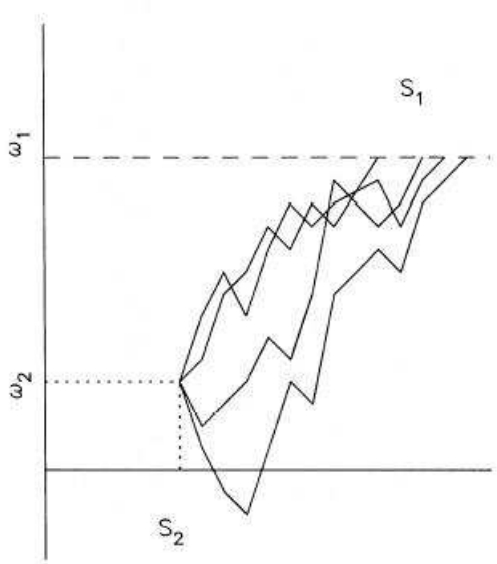

Figure 3.3: Set of trajectories constrained to pass through $(S_2, \delta_c(t_2))$ ($\omega_1 \equiv \delta_c(t_1)$ and $\omega_2 \equiv \delta_c(t_2)$), that correspond to the particles constrained to be part of a halo with variance S_2, at t_2, from Lacey & Cole (1993).

3.3.3 Descendant Mass Function

The descendant mass function is the probability that a halo of mass M_1 at time t_1 will form a halo of mass $M_2 > M_1$ at time $t_2 > t_1$ ($z_2 < z_1$) through merger events; i.e. the conditional probability that a particle resides in an object of mass M_2 at a redshift z_2 provided that it has been part of an object of mass M_1 at $z_1 > z_2$. In order to find the analitical form of this distribution, it is necessary to enunciate the Bayes theorem: the probability of an event A given an event B, is equal to the ratio of the probability of A over the one of B, times the probability of B given A: $p(A|B) = \frac{p(A)}{p(B)} p(B|A)$. So, using the global mass function an the progenitor mass function, it is strightforward to obtain the descendant mass function:

$$\begin{aligned} p(S_2, \delta_c(t_2)|S_1, \delta_c(t_1))\, \mathrm{d}S_2 &= \frac{p(S_1, \delta_c(t_1)|S_2, \delta_c(t_2))\, \mathrm{d}S_1 p(S_2, \delta_c(t_2))\, \mathrm{d}S_2}{p(S_1, \delta_c(t_1))\, \mathrm{d}S_1} \\ &= \left[\frac{S_1}{S_2(S_1 - S_2)}\right]^{3/2} \frac{\delta_c(t_2)(\delta_c(t_1) - \delta_c(t_2))}{\sqrt{2\pi}\delta_c(t_1)} \\ &\times \exp\left[-\frac{(\delta_c(t_2)S_1 - \delta_c(t_1)S_2)^2}{2S_1S_2(S_1 - S_2)}\right] \mathrm{d}S_2 \end{aligned} \tag{3.27}$$

The distribution as a function of mass is obtained multiplying by the Jacobian $|\frac{\mathrm{d}S_2}{\mathrm{d}M_2}|$.

3.3.4 Merger Rate

If one consider a finite time interval Δt, the mass of a halo can change by an amount ΔM, due to the cumulative effects of more than one merger; in an infinitesimal interval $\mathrm{d}t$, the entire ΔM must be due to a single merger event. So taking the limit in the descendent mass function for $t_2 \to t_1$ (so $\delta_{c2} \to \delta_{c1}$), one can obtain the merger rate:

$$\begin{aligned} \frac{\mathrm{d}^2 p}{\mathrm{d}ln\Delta M \mathrm{d}t}(M_1 \to M_2|t) &= 2\sigma_2 \left|\frac{\mathrm{d}\sigma_2}{\mathrm{d}M_2}\right| \Delta M \left|\frac{\mathrm{d}\delta_c(t)}{\mathrm{d}t}\right| \frac{1}{\sqrt{2\pi}} \left[\frac{S_1}{S_1(S_1-S_2)}\right]^{3/2} \times \\ &\times \exp\left[-\frac{\delta_c^2(S_1-S_2)}{2S_1S_2}\right] \end{aligned} \tag{3.28}$$

This is the rate of merging of a halo of mass M_1 with a halo of mass ΔM.

3.3.5 Creation and Destruction Rates

The growth of clustering in a system in which clusters coalesce by binary mergers is described by the Smoluchowski equation [72]: given the distribution $n(M,t)$, of objects masses M at time t, this equation gives the rate of change of this distribution:

$$\begin{aligned} \frac{\partial n(M,t)}{\partial t} &= \int_0^{M/2} Q(M-M',M';t)n(M-M';t)n(M';t)dM' + \\ &- \int_0^{\infty} Q(M,M';t)n(M,t)n(M',t)dM' \end{aligned} \tag{3.29}$$

where $Q(M_1,M_2;t)$ encodes the merger rate between objects of mass M_1 and M_2 at time t. The first term represents the creation event and the second term the destruction ones; within the hierachical scenario, the destruction is the disappearance of objects of a certain mass due to the merging with other objects (with the result of forming more massive structures) and must not be confused with the fragmentation of a halo in smaller haloes, that is common in numerical simulations, but it is not contemplated in the analytical model. Although some authors (Cavaliere et al. 1991 [12], Blain & Longair 1993 [6]) defined the creation and destruction rates of a dark matter halo as the positive and negative part of the time derivative of the mass function, there no theoretical reasons to accept it. In fact, this method is tightly related to the "shape" of the analitical form of the global mass function in the spherical collapse that allow to obtain only two terms making the derivative, one positive and one negative. A more precise method to obtain these distributions is shown by Kitayama and Suto (1996). They define the creation and destruction rates as the comoving number density of bound systems of a given mass that are created or destroyed in unit time at a given epoch. In order to find the rates with the Kitayama and Suto procedure, one must find the instantaneous transition rates starting from the the progenitor and descendant mass

functions and making a time derivative of them. For the instantaneous creation rate, let put $t_1 = t - \Delta t$, $t_2 = t$, $M_2 = M$, in the progenitor mass function, and consider the limit $\Delta t \to 0$:

$$\begin{aligned}\frac{\mathrm{d}P_1(M_1 \to M;t)}{\mathrm{d}t} &\equiv \lim_{\Delta t \to 0} \frac{P_1(M_1, t-\Delta t|M,t)}{\Delta t} \\ &= \frac{1}{\sqrt{2\pi}} \frac{1}{(S_1 - S)^{3/2}} \left[-\frac{\mathrm{d}\delta_c(t)}{dt}\right] \left|\frac{\mathrm{d}S_1}{\mathrm{d}M_1}\right|; \end{aligned} \tag{3.30}$$

The instantaneous destruction rate is obtained by putting $t_2 = t + \Delta t$, $t_1 = t$, $M_1 = M$, in the descendant mass function and considering the limit $\Delta t \to 0$:

$$\begin{aligned}\frac{dP_2(M \to M_2;t)}{dt} &\equiv \lim_{\Delta t \to 0} \frac{P_2(M_2, t+\Delta t|M,t)}{\Delta t} \\ &= \frac{1}{\sqrt{2\pi}} \left[\frac{S}{S_2(S-S2)}\right]^{\frac{3}{2}} \left[-\frac{\mathrm{d}\delta_c(t)}{\mathrm{d}t}\right] \left|\frac{\mathrm{d}S_2}{\mathrm{d}M_2}\right] \\ &\quad \times \exp\left[-\frac{(S-S_2)\delta_c^2(t)}{2SS_2}\right]. \end{aligned} \tag{3.31}$$

This expression was defined as the merger rate. The fomation and destruction rates are defined as:

$$R_{crea}(M,t) \equiv \int_0^M \mathrm{d}M_1 \frac{\mathrm{d}P_1(M_1 \to M;t)}{\mathrm{d}t} N_{PS}(M,t) \tag{3.32}$$

and

$$R_{dest}(M,t) \equiv \int_M^\infty \mathrm{d}M_2 \frac{\mathrm{d}P_2(M \to M_2;t)}{\mathrm{d}t} N_{PS}(M,t). \tag{3.33}$$

3.3.6 The difference between Formation and Creation

Authors have used the term *formation* to consider both the time in the merging history of a halo when the principal progenitor has at least half of the mass of the considered halo (Lacey and Cole, 1993) and the quantities that follow by the progenitor mass function (Kitayama and Suto, 1996). Following the clarification by Giocoli at al. 2007 [26] about this misunderstanding, in this thesis the term "creation" is used referring to the numerical increment of halo of a certain mass caused by the merging of haloes of smaller masses.

Chapter 4

Distributions in the Ellipsoidal Collapse Model

The unconditional mass function found in the spherical collapse context (eq. (3.21)) is reasonably accurate if compared with the results of numerical simulations; however Lacey and Cole (1994) [42] and Sheth and Tormen (1999) [69] showed that the Press-Schechter mass function fails for small haloes and for the high mass cut-off: it predicts too much small structures and less massive objects respect to the results of different simulations (e.g. Efstathiou et al. 1985 [20] for LC93 and the GIF simulation by Kauffmann et al. 1999 [35] for ST99). Sheth, Mo and Tormen (2001) [68] showed how this discrepancy between theory and simulations can be reduced substantially if bound structures are assumed to form from an ellipsoidal, rather than a spherical, collapse.

4.1 Moving Barrier

The excursion sets model builds the spherical collapse into the Press and Schechter formalism, by determing a constant barrier in δ that has to be crossed to found the collapse. This threshod does not depend on mass (or variance) but it is a functions of the redshift (or time). This reflects the fact that the evolution of a spherical initial overdensity is driven only by its self-gravity. The non-correlation of the random walks and the independence of the barrier on $\nu = \frac{\delta_{sc}}{\sigma}$ allow to obtain a simple formula for the mass function associated to the spherical collapse (eq. 3.24). Within this spherical approach the effects due to the background cosmology and those due to the power spectrum can be treated separately: the cosmological models determine how δ_{sc} depends on z (or t), whereas the power spectrum shape constrains the dependence of the variance on $M \propto R^3$.

Within the excursion set approach the shape of the mass function is determined by

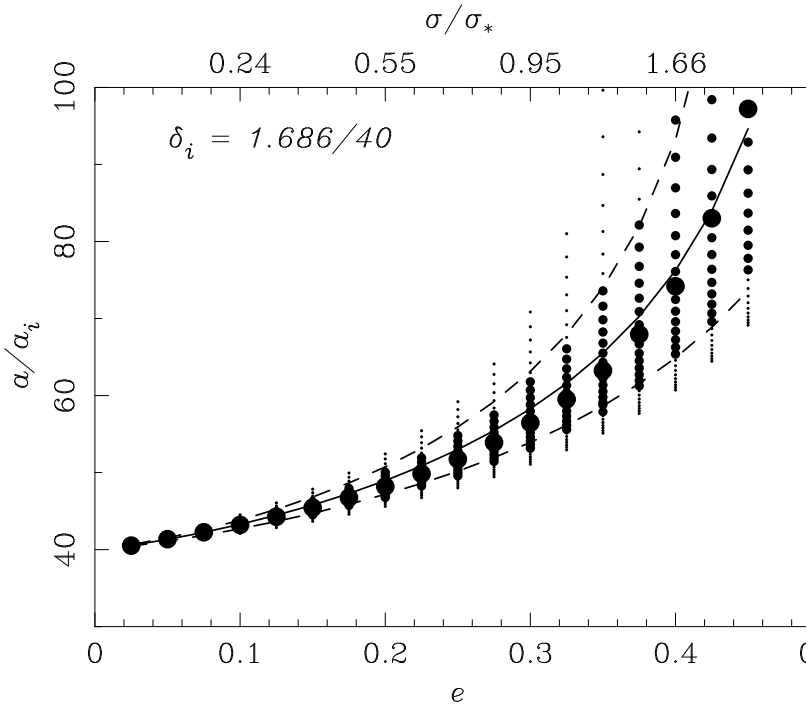

Figure 4.1: The evolution of an ellipsoidal perturbation in an Einstein-de Sitter universe. Symbols show the expansion factor when the longest axis collapses and virializes, as a function of initial e and p, in steps of 0.025, if the initial overdensity was δ_i. The solid curve shows the formula for the $p = 0$ result, and the dashed curves show $|p| = e/2$. The time required to collapse increases mononically as p decreases. The axis on the right shows the associated critical overdensity required for collapse, and the axis on the top shows the result of using the formula to translate from e to $\sigma(m)$ when $p = 0$. From SMT01 [68].

the threshold and by the dependence of S on M. Since $S(M)$ depends on the initial power spectrum but not on the underlying dynamics, in order to incorporate the effects of the ellipsoidal collapse into the excursion sets model, SMT01 determine the barrier shape associated with the non-spherical dynamics. They consider the ellipsoidal model described by Bond and Myers (1996) [8], in which the perturbation is assumed to be better described by the initial shear field than the initial density field. For a given background model (SMT01 assume an Einstein- de Sitter universe), the evolution of an ellipsoidal perturbation is determined by the eigenvalues of the perturbation tensor [1]: the initial ellipticity e, the prolateness p, the density contrast δ. Figure 4.1 shows the expansion factor at the collapse as a function of e and p; at a given e, the largest circles

[1] Any position in a smoothed Gaussian random field has an associated perturbation potential, the second derivatives of which define the deformation tensor

show the relation at $p = 0$, medium ones at $|p| \leq e/2$, small ones at $|p| \geq e/2$. On average, virialization occurs later as e increase and as p decreases. For Eistein-de Sitter models, the expansion factor is proportional to the linear theory grow factor, so the plot shows also a relation for $\delta_{ec}(e, p)$, where the subscript ec refers to the ellipsoidal collapse. For a range of e and p, a reasonable approximation to this relation is given by:

$$\frac{\delta_{ec}(e,p)}{\delta_{sc}} = 1 + \beta\Big[5(e^2 \pm p^2)\frac{\delta_{ec}^2(e,p)}{\delta_{sc}}\Big]^{\gamma} \tag{4.1}$$

where $\beta = 0.47$, $\gamma = 0.615$, δ_{sc} is the critical spherical collapse value; the plus (minus) sign is used if p_ν is negative (positive). The solide curve in Figure 4.1 shows the value given by equation 4.1 with $\gamma = 0.615$ and shows that the fitting is precise within 10%. With a Gaussian initial field, for every scale R_f (parametrized by $\sigma(R_f)$), there is a range of probable values of e, p and δ. This means that there is a range of collapse times associated with regions of size R_f. One can obtain an estimate for an average $\delta_{ec}(\sigma)$ by averaging $\delta_{ec}(e, p)$ over $p(e, p, \delta/\sigma)$ suitably. To do this, SMT01 notice that on average, in a Gaussian field, $p = 0$. The solid curve in Fig. 4.1 shows the expansion factor at virialization in this case. It is straightforward to use this curve to compute the associated $\delta_{ec}(e, z)$. Having done so, if one can relate e to the mass m, then he will be in a position to describe the barrier shape associated with ellipsoidal, rather than spherical collapse. This can be done as follows. Regions initially having a given value of δ/σ most probably have an ellipticity $e_{mp} = (\sigma/\delta)/\sqrt{5}$. To collapse and form a bound object at z, the initial overdensity of such a region must have been $\delta_{ec}(e_{mp}, z)$. If one requires that δ on the right hand side of this relation for e_{mp} be equal to this critical value $\delta_{ec}(e_{mp}, z)$, then this sets $\sigma^2(R_{\rm f})$. Since R_f^3 is proportional to mass, this provides a relation between e and mass, and so between δ_{ec} and mass:

$$\delta_{ec}(\sigma, z) = \delta_{sc}(z)\,\left(1 + \beta\left[\frac{\sigma^2}{\sigma_*^2(z)}\right]^{\gamma}\right), \tag{4.2}$$

where $\sigma_*(z) \equiv \delta_{sc}(z)$. The axis labels on the top and right of the plot show this ($p = 0$) relation. Notice that the power spectrum enters only in the relation between σ and m, whereas the effects of cosmology enter only in the relation between δ_{sc} and z. This expression is approximately the same for SCDM, OCDM, and ΛCDM models if all variances $\sigma^2(m)$ are computed using the model dependent power spectrum, and the value of $\delta_{\rm sc}(z)$ is computed using the spherical collapse model after including its dependence on background cosmology: the differences between these models arise primarily from converting the scaling variable ν to the physical variables z and m. A number of features of equation (4.2) are worth noticing. Massive objects have $\sigma/\sigma_* \ll 1$. For such objects equation (4.2) suggests that $\delta_{\rm ec}(\sigma, z) \approx \delta_{\rm sc}(z)$, so the critical overdensity required for collapse at z is approximately independent of mass: massive objects are well described

by the spherical collapse model. Second, the critical overdensity increases with $\sigma(m)$, so it is larger for less massive objects. This is because smaller objects are more influenced by external tides; they must have a greater internal density if they are to hold themselves together as they collapse. Eq. (4.2) is extremely useful because it allows one to include the effects of ellipsoidal collapse into the Bond et al. (1991) excursion set model in a straightforward manner. Namely, all we need to do is to use equation (4.2) when setting $B(\sigma, z) = \delta_{\rm ec}(\sigma, z)$. The threshold $B(\sigma, z)$ found is called moving barrier allows to obtain the distributions in an ellispoidal collapse context using the logic of Lacey and Cole (1993).

4.1.1 Mass Function

SMT01 give also an estimate of the mass function associated with ellipsoidal collapse, using the distribution of first crossing of the moving barrier (4.2) by indipendent random walk. This first crossing distribution is:

$$\nu\, f(\nu) = 2A \left(1 + \frac{1}{\nu^{2q}}\right) \left(\frac{\nu^2}{2\pi}\right)^{1/2} \exp\left(-\frac{\nu^2}{2}\right), \tag{4.3}$$

where $q = 0.3$ and $A \approx 0.3222$. This first crossing distribution differs from the one predicted by the "standard" constant barrier model for which $q = 0$ and $A = 1/2$. In 1999, Sheth and Tormen showed that, for the GIF simulation (Kauffman et al. 1999), the unconditional mass function is well approximated by:

$$\nu f(\nu) = 2A\Big(1 + \frac{1}{(\sqrt{a}\nu)^{2q}}\Big)\frac{\sqrt{a}\nu}{\sqrt{2\pi}}\exp\Big(-\frac{a\nu}{2}\Big) \tag{4.4}$$

where $a = 0.707$, $q = 0.3$, $A \approx 0.322$. A is determined by assuming that $\int f(\nu)\mathrm{d}\nu = 1$; q depends on the shape of the mass function at the small-mass end; a is determined by the number of massive haloes in the simulation. It is possible to obtain the barrier corresponding to this distribution: to a good approximation the threshold associated with the GIF simulation has the form:

$$B_{GIF}(S, z) = \sqrt{a}\delta_{sc}\Big[1 + \beta\Big(\frac{S}{a\delta_{sc}^2}\Big)^{\alpha}\Big] \tag{4.5}$$

where $S = \sigma^2$, $a = 0.707$, $\beta \approx 0.485$, $\alpha \approx 0.615$. Both the shape of the GIF-barrier and of the GIF-mass function differ from equations 4.2 and 4.3 by the factor a. In order to understand from where this factor comes from, consider that when one simulates a number of excursion sets that cross an absorbing barrier, the masses of the haloes that derive from this analysis are averaged over the mass corresponding to each trajectory; however, that mass is labelled as the one corresponding to the central particle of the formed halo. So the actual mass is less than the predicted one because of the contribution

of the other trajectories that do not correspond to particles in the center. In order to shift the result toward bigger masses, the factor $\sqrt{a}$ is introduced to lower the density threshold for the collapse and compensate the lack of prediction of bigger haloes.

In the rest of this work we will assume B_{GIF} as the shape of the barrier for the ellipsoidal collapse.

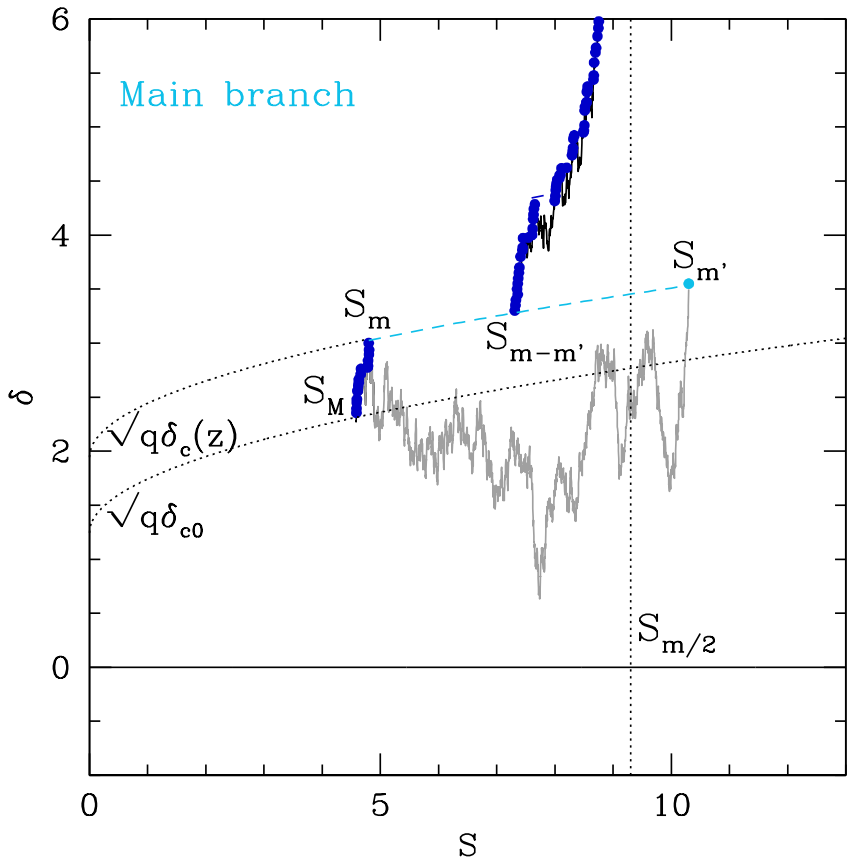

Figure 4.2: The same as Figure 4.2 but with a moving barrier (in this case a square-root barrier). From Moreno et al. 2008 [51].

4.1.2 Special barriers

The value of the exponent α can be modified to obtain other barrier shapes that give different forms for the mass function. Only in few cases this expression can be written in an analytical form:

- if $\alpha = 0$ one obtains the constant barrier that characterizes the spherical collapse. See Section 3.3 for the corresponding mass function.

- if $\alpha = 1$ (linear barrier), Sheth (1998) [67] shows that:

$$f(S,z) = \frac{B(0,z)}{\sqrt{2\pi}S^{3/2}} \exp\left[-\frac{B^2(S,z)}{2S}\right] \tag{4.6}$$

- if $\alpha = 0.5$ (square-root barrier), Mahmood e Rajesh (2005) [45] show that:

$$f(S) = \frac{\exp\left(-\frac{\beta^2}{4D}\right)}{2S} \sum_v \left(\frac{a\delta_{sc}^2}{DS}\right)^{v/2} \frac{U_v'\left(-\frac{\beta}{\sqrt{D}}\right)}{I_v\left(-\frac{\beta}{\sqrt{D}}\right)} \quad , \tag{4.7}$$

where $a = 0.707$, $\beta \approx 0.485$; $U'(\delta)$ is the derivative, respect to δ, of the parabolic cylinder function, defined by Erdelyi (1953) [22]:

$$U_v(\delta) = \sqrt{\frac{2}{\pi}} \quad e^{x^2/4} \int_0^\infty \mathrm{d}t \quad e^{-t^2/2} t^v \cos\left(\delta t - \frac{v\pi}{2}\right) \quad , \tag{4.8}$$

with $v \geq -1$; The definition of I_v is:

$$I_v(x) = \int_x^\infty U_v^2(y)\mathrm{d}y \quad ; \tag{4.9}$$

D is the diffusion constant that constrains the random walks.

- if $\alpha = 2$ (square barrier), Mahmood e Rajesh (2005) show that:

$$f(S) = \frac{2b^2k^2 e^{-2b^2S^3/3D}}{D} \sum_{n=1}^{\infty} e^{-\lambda_n S} \frac{Ai(2b\sqrt{a}\delta_{sc}/D - \lambda_n)}{Ai'(-k\lambda_n)} \tag{4.10}$$

where $b = \beta(\sqrt{a}\delta_{sc})^{-3}$ ($\beta \approx 0.485$); $k = \left[\frac{D}{2b^2}\right]^{1/3}$; $Ai(y)$ is the Airy function[2]; λ_n are the eigenvalues of the diffusion equation; $Ai'(x)$ is the x-derivative of the Airy function.

4.2 Extension and improvement of the Ellipsoidal Collapse Model

In the last ten years many authors tried to improve the analytical form of various distributions both remaining within the excursion sets formalism and trying to write fitting formulae so without assuming necessarily the prescriptions of the ellipsoidal collapse. For the unconditional mass function, the most important fitting forms are those of Jenskin et al. (2001) [33], Warren et al. (2006) [86] and especially for high redshift mass function: Reed et al. (2003, 2007) [60], [61], Lukic et al. (2007) [44]. Other authors

[2]The Airy function is the solution of the differential equation: $\frac{\partial^2\psi}{\partial y^2} - y\psi = 0$.

made use of the excursion sets tool and worked on it e.g. considering series expansions of the barrier like Sheth & Tormen (2002) [70], or considering various shapes of the moving barrier like Mahmood & Rajes (2005) [45] or Zhang & Hui (2005) [94], or considering fractional or correlated excursion sets like Pan (2007) [53] or Pan et al. (2008) [54].
The progenitor mass function was first considered by Sheth and Tormen (2002) for the ellipsoidal collapse model; Rubino-Martìn at al. (2008) [62] obtained the conditional mass funciton by a rescaling of the unconditional one; Zhang, Ma and Fakhouri (2008) [95] found equations for progenitor mass function in the limit of small look back times. The problem of the merger rates was faced by several authors: Benson et al. (2005) [4] and Benson (2008) [5] used the Smoluchowski formalism (1916) [72] to deal with these quantities; Fakhouri & Ma (2008) [23] gave different definitions of the quantity merger rate and, for each one, they checked the behaviour of dark haloes with simulations; Neistein and Dekel (2008) [52] derived analytic merger rates considering more than two progenitor for each merger. Moreno et al. (2009) [51] found an equation for the creation rate in moving barrier models.

All these efforts in finding improvements for the dark matter haloes distributions come not only from the purpose to give a coherent scenario for the dark universe, but also from the necessity of having precise and possibly simple equations to use in various fields of astrophysics. Current scenario of galaxy formation assumes that the dark matter haloes are the structures that trigger the potential well within which the baryonic matter falls and where the gas can cool and form stars (White & Rees, 1978 [90], White & Frenk, 1991 [89], Kauffman et al., 1999 [35]): in such models, understanding the properties of dark haloes is important. Merger history trees are the key to understand galaxy formation and evolution, and any semi-analytical model must include the merger dynamics of their host haloes. They are useful at studying the brighter galaxies in the core of rich galaxy clusters (De Lucia & Blaizot, 2007 [17]), satellites and intra cluster light (Conroy et al., 2007 [15]). Galaxy mergers drive gas toward central starburst (Milhos & Hernquist, 1996 [48]) and supermassive black holes (Hernquist, 1989 [31]). The rate of dark matter mergers is a crucial ingredient in models of galaxy and large scale structure formation, from sub-galactic scale to galaxy-cluster scale. Merger rates have been applied to galaxy formation models: to determine the galaxy morphology through merger history (Gottlober et al. 1999 [27]); for AGN activity (Wyithe and Loeb, 2003 [92]); models for Lyman-break galaxies (Kolatt et al., 1999 [38]); abundances of binary supermassive black holes (Volonteri et al., 2002 [85]); rates for SMBH coalescence (Milovavljevic and Merritt, 2001 [49]) and the resulting LISA event rate (Menou et al., 2001 [47], Haehnelt, 1994 [30]); the first stars (Santos et al., 2002 [63], Scannapieco et al., 2003 [65]); galactic-halo substructure (Kamionkowski and Liddle, 2000 [34], Bullok et al, 2000 [11], Benson et al., 2002 [3], Somerville, 2002 [73], Stiff et al., 2001 [78]);

halo angular momenta (Vitvitska et al., 2002 [84]) and concentrations (Wechstler et al., 2002 [87]); galaxy clustering (Percival et al. 2003 [56]); particle acceleration in clusters (Gabici & Blasi [24]); and formation-redshift distributions for galaxies and clusters and thus their distributions in size, temperature, luminosity, mass, and velocity (Verde et al., 2001, 2002 [82], [83]).

4.3 What's new in this thesis

The leading idea of this thesis is to find precise and simple analytical equations describing some usefull distributions for the dark matter haloes, starting from the unconditional mass function, passing through the progenitor and descendant mass functions, and arriving to the instantaneous creation and destruction rates. The constrain is to remain in the context of the ellipsoidal collapse, since it is built on a robust physical theory and it works better for the global mass function. The tool used is the described excursion sets theory and the approach is similar to that exploited to obtain distributions for spherical objects. In this way, we want to extend to the more precise ellipsoidal dynamic the mass distributions that are usually used, remaing in the spherical case. In Table 4.3 there is summary of the functions that was so far obtained and checked with simulation.

Distribution	SC	check sim	EC	check sim
UMF	LC93	Yes	SMT01, ST02, this work	Yes
PMF	LC93	Yes	ST02, ZMF08, this work	Yes
DMF	LC93	Yes	This work	Yes
ICR	KS96	—	This work	—
IDR	LC93	Yes	This work	Yes
CR	KS96 PM99	Yes	MGS09	Yes
DR	KS96	—	—	—

Table 4.1: For different distributions (Unconditional, Progenitor, Descendant mass functions, Creation and Destruction Rates -Instantaneous and not-), the table shows if there exist an analytical form in the literature and if some authors compare it with the results of the numerical simulations. The abbreviations refer to the names of the authors, easily retrievable in the text.

We start from the work of Sheth and Tormen (2002) [70]: in this paper, the authors show that in the ellipsoidal context, a good approximation for the global mass function,

obtained with the excursion sets approach with a generic moving barrier, is:

$$f(S)\mathrm{d}S = \frac{|T(S)|}{\sqrt{2\pi}S^{3/2}}\exp\left[-\frac{B(S)^2}{2S}\right]dS \tag{4.11}$$

This mass function is expressed in the variable S, the variance of the fuctuations, because from this distribution is easier to do the step toward the progenitor mass function as will be described later. In the equation $B(S)$ is the moving barrier described by eq. (4.5) and $T(S)$ is one of the key-ingredient for understand the work done; this term is defined as:

$$T(S) = \sum_{n=0}^{5}\frac{(-S)^n}{n}\frac{\partial^n B(S)}{\partial S^n} \tag{4.12}$$

This quantity represents the first six terms of the Taylor expansion series of the barrier around the generic position S and evaluated in $S = 0$. Exploiting some recursive properties of the derivative of the barrier respect to S, one ca re-write the mass function in this way:

$$f(S) = \frac{1}{\sqrt{2\pi}S^{3/2}}\exp\left[-\frac{B(S)^2}{2S}\right]\sqrt{a}\delta_{sc}\left[1+\frac{\beta S^\alpha}{(a\delta_{sc}^2)^\alpha}\sum_{n=0}^{5}\frac{(-1)^n}{n!}\prod_{i=0}^{n}\frac{\alpha-i}{\alpha-n}\right] \tag{4.13}$$

A first look to the geometry of the moving barrier, respect to the constant one can, suggests that the use of the Lacey & Cole approach to find the progenitor mass function is more difficult here. The moving barrier shape is not linear in S so, changing the origin (constraining the trajectories of the excursion sets to pass through the point associated to the a halo of which the progenitors are sought) the barrier has not the same functional form. The difference:

$$B(S_1,z_1) - B(S_2,z_2) = \sqrt{a}\delta(z_1)[1+\beta S_1^\alpha/(a\delta(z_1)^2)^\alpha] - \sqrt{a}\delta(z_2)[1+\beta S_2^\alpha/(a\delta(z_2)^2)^\alpha] \tag{4.14}$$

can be written as a constant plus a term which scales as $(S_1 - S_2)^\alpha$ only if α equals zero or one. This means that the solution of the two barrier problem can not be given by a simple rescaling of the unconditional ellipsoidal mass function. However, ST02 avoid this problem starting from eq. (4.11) and making these substitutions: $S \to (S_1 - S_2)$, $B(S) \to (B(S_1,z_1) - B(S_2,z_2))$, $T(S) \to T(S_1|S_2)$, where the subscript 2 refers to an halo with variance $S_2 = S(M_2) < S_1 = S(M_1)$ at time $t_2 > t_1$ (corresponding to $z_2 < z_1$) and the subscript 1 is attached to its progenitor. They write:

$$f(S_1,z_1|S_2,z_2)dS_1 = \frac{|T(S_1|S_2)|}{\sqrt{2\pi}(S_1-S_2)^{3/2}}\exp\left[-\frac{[B(S_1,z_1)-B(S_2,z_2)]^2}{2(S_1-S_2)}\right]dS_1 \tag{4.15}$$

The term $T(S_1|S_2)$ is the second important expansion series for this work; it is defined as:

$$T(S_1|S_2) = \sum_{n=0}^{5}\frac{(S_2-S_1)^n}{n!}\frac{\partial^n[B(S_2,z_2)-B(S_1,z_1)]}{\partial S_1} \tag{4.16}$$

It is the difference between the sum of the first 6 terms of the Taylor expansion series of $B(S, z_1)$ around a generic S_1 and evaluated in S_2, and the value of $B(S, z_2)$ in S_2. The equation 4.15 can be re-written in this way:

$$f(S_1, z_1|S_2, z_2)dS_1 = \frac{1}{\sqrt{2\pi}(S_1 - S_2)^{3/2}} \exp\left[-\frac{[B(S_1, z_1) - B(S_2, z_2)]^2}{2(S_1 - S_2)}\right] \times$$
$$\times \quad \Big[\sqrt{a}(\delta_{sc}(z_1) - \delta_{sc}(z_2)) + \beta\left(\frac{S_1^\alpha}{(a\delta(z_1)^2)^{\alpha-0.5}}\Big(\sum_{n=0}^{5}\left(\frac{S_2 - S_1}{S_1}\right)^n \frac{1}{n!}\prod_{i=0}^{n}\frac{\alpha - 1}{\alpha - n}\right) +$$
$$- \quad \Big(\frac{S_2^\alpha}{(a\delta(z_2)^2)^{\alpha-0.5}}\Big)\Big]dS_1 \tag{4.17}$$

So the introduction of the Taylor expansion series in the mass function leads to a distribution that is "only" an approximation to the exact solution, but allows to obtain the consequent conditional mass function.

A look at the equations written so far can highlight how difficult can be their application in particular when used to find other distributions, e.g. the descendant mass function or the rates of creation and destruction. For this reason this thesis investigates the possibility to exchange the equation found in literature with other forms, possibly simple, but mantaining, or improving the accuracy (measured as a match to the results of the numerical simulations) and mantaining the basic features of the ellipsoidal collapse model. In order to find an improvement of the "standard" ellipsoidal collapse, two parameters in the equations of the unconditional and progenitor mass function were chosen to be tuned in order to find the best formulas; in this context the word "best" means both that better fits the numerical simulations and that shows a simple functional form. The parameter chosen to be free are the (i) orders of the two Taylor expansion series and (ii) the normalization of the distribution. The "hope" in doing this is to find that the best distribution (or, at least, a good approximation), would be the one with zero or infinite terms in the expansion series because they provide simple analytical form for all the distributions in which we are interested. In Figure 4.3 a geometrical representation of the meaning of T_0 and T_∞ for the "conditional" expansion series (eq. (4.16)) is shown. The plot shows that the Taylor expansion is the difference between the height of two moving barriers considered at two different epochs, and for different S, depending on the order chosen; the results of $T(S_1|S_2)$ lies between the minimum value provide by considering ∞ terms in the Tayor expansion, and the maximum value given by T with 0 orders. The utility of these two cases is higlighted by the simplicity if the mass functions that derive; for the unconditional mass function one obtains:

$$f(S)\mathrm{d}S = \frac{B(S)}{\sqrt{2\pi}S^{3/2}} \exp\left[-\frac{B(S)^2}{2S}\right] dS \tag{4.18}$$

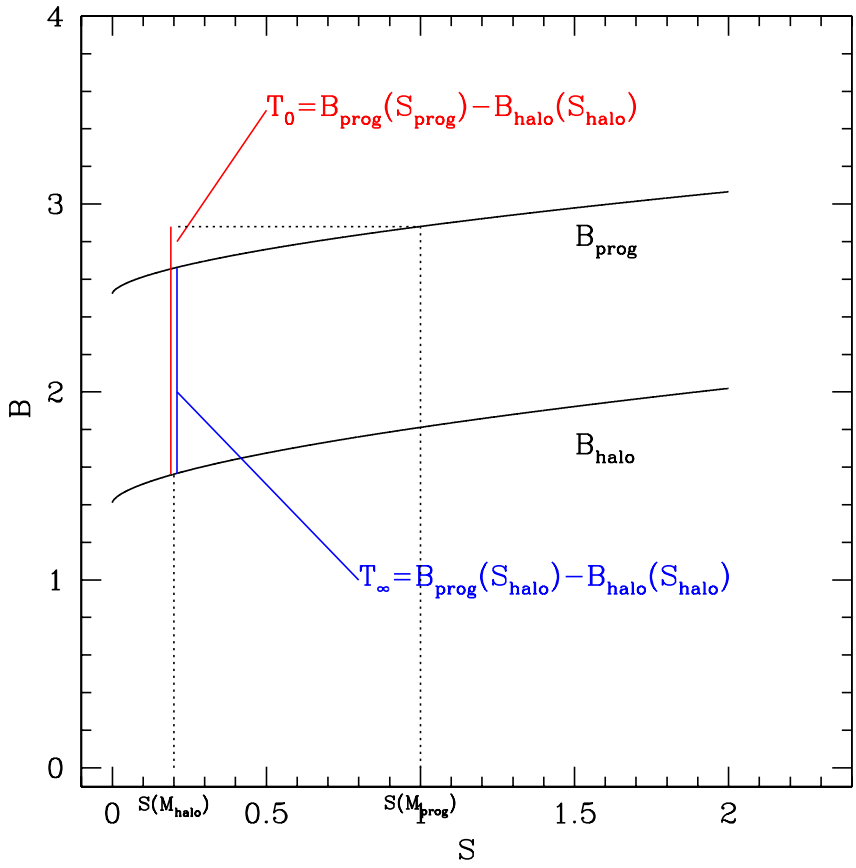

Figure 4.3: Two moving barrier are shown at different redshift. The blue shorter draw is the geometrical meaning of the Taylor expansion series eq. (4.16) with infinite terms; the red longer draw is the series with 0 term.

considering 0 orders;

$$f(S)\mathrm{d}S = \frac{\sqrt{a}\delta_{sc}}{\sqrt{2\pi}S^{3/2}}\exp\left[-\frac{B(S)^2}{2S}\right]dS \tag{4.19}$$

with infinite orders. The progenitor mass function becomes:

$$f(S_1,z_1|S_2,z_2)dS_1 = \frac{B(S_1,z_1)-B(S_2,z_2)}{\sqrt{2\pi}(S_1-S_2)^{3/2}}\exp\left[-\frac{[B(S_1,z_1)-B(S_2,z_2)]^2}{2(S_1-S_2)}\right]dS_1 \tag{4.20}$$

with zero orders;

$$f(S_1,z_1|S_2,z_2)dS_1 = \frac{B(S_2,z_1)-B(S_2,z_2)}{\sqrt{2\pi}(S_1-S_2)^{3/2}}\exp\left[-\frac{[B(S_1,z_1)-B(S_2,z_2)]^2}{2(S_1-S_2)}\right]dS_1 \tag{4.21}$$

with infinite orders. All these equations have a simple analytical form that avoids the Taylor expansion.

4.4 Descendant Mass Function and Merger Rate

In literature there is not an explicit analytical form for the distribution of the descendent of dark matter haloes for the ellipsoidal collapse model. Here the procedure of Lacey & Cole (1993) is used to obtain such formula (see Section 3.3.3). Exploiting the Bayes relation for the conditional probability, the progenitor and two global mass functions are mixed to obtain the probability that a particle will resides in a halo of mass M_2 at time z_2 given that it is part of a halo of mass $M_1 < M_2$ at time $z_1 > z_2$. If expressed in the variables S and z one can write:

$$\begin{aligned} f(S_2, z_2 \quad | \quad S_1, z_1) = & \frac{1}{\sqrt{(2\pi)}} \left[\frac{S_1}{S_2(S_1 - S_2)}\right]^{\frac{3}{2}} \times \\ \times \quad & \exp\left\{-\frac{(B(S_1, z_1)S_2 - B(S_2, z_2)S_1)^2}{2S_1S_2(S_1 - S_2)}\right\} \frac{T(S_1|S_2)T(S_2)}{T(S_1)} \end{aligned} \tag{4.22}$$

Here the combination of the three Taylor series depends on how many orders one chooses for the three distributions.

In order to obtain the functional form for the merger rate (or instantaneous rate of destruction), the best choice to do is to consider the Taylor expansions with infinite terms into the descendant distribution and then follow the prescriptions explained in Section 3.3.5. The resulting distribution is:

$$\begin{aligned} \frac{\mathrm{d}^2 p(S_2, z)}{\mathrm{d}S_2 \mathrm{d}t} = & \frac{\sqrt{a}\left|\frac{\mathrm{d}\delta}{\mathrm{d}t}\right|\left(1 + \beta\left(\frac{S_2}{a\delta^2}\right)^{\alpha}(1 - 2\alpha)\right)}{\sqrt{2\pi}} \times \\ \times & \left[\frac{S}{S_2(S - S_2)}\right]^{\frac{3}{2}} \exp\left\{ - \frac{a\delta^2(S - S_2)\left(1 + \frac{\beta}{(a\delta^2)^{\alpha}}\left(\frac{S^{\alpha}S_2 - S_2^{\alpha}S}{S_2 - S}\right)\right)^2}{2SS_2}\right\} \end{aligned} \tag{4.23}$$

where the dependence on time is inherent to the density threshold. Also this result does not show the analytical complexity coming from the Taylor expansion; moreover, this distribution can not be derived using at the same time the method by LC93 and a generic order of the expansion in the progenitor mass function, because of mathematical difficulties.

4.5 Instanteneous Rate of Creation

The instantaneous rate of creation, as defined in Kitayama & Suto (1996) (see Section 3.3.5) is obtained with a time derivative of the progenitor mass function. Again,

here the Taylor expansion with an infinite number of terms is used:

$$\frac{\mathrm{d}^2 p(S_1,t)}{\mathrm{d}S_1 \mathrm{d}t} = \sqrt{a}\left|\frac{\mathrm{d}\delta}{\mathrm{d}t}\right| \frac{1+\beta\left(\frac{S}{a\delta^2}\right)^{\alpha}(1-2\alpha)}{\sqrt{2\pi}(S_1-S)^{\frac{3}{2}}} \tag{4.24}$$

Actually, for this distribution there exist a form by Moreno et al. (2009) [51] in the ellipsidal context; however these authors find it considering the square-root barrier.

Chapter 5

Statistical analysis of new distributions

In this chapter, the comparison between the analytical equations and the corresponding quantities found with the numerical simulations is described. In Chapter 4, there is the description of some distributions for ellipsoidal dark matter haloes; as already described, the common feature of all these formulae is a Taylor expansion series $T(S)$ (eq. (4.12),(4.16)), with a variable number of orders. In order to compare the theory and the simulations, the number of terms of the expansion series for each distribution is kept variable as well as the normalization of the entire distribution. For each quantity, a "matrix" of models is considered: one dimension represents a certain "ellipsoidal" distribution with the series truncated at orders from 0 to 100, plus the distribution with the entire series (∞ terms), and the corresponding "spherical" distribution; the other dimension has the order fixed and it represents the different normalizations, from 0.1 to 3.0, with step 0.01. In this way it is possible to obtain the curve that better fits the simulation data.

The choice of the best model is the result of a χ^2-test: the data coming from the simulations are divided into mass bins with an associated error; the χ^2-analysis is weighted on these poissonian uncertenties. The best model is associated to the minimum value of:

$$\chi^2 = \sum_{i=1}^{n} \frac{(D_i - A_i)^2}{nE_i} \tag{5.1}$$

where D_i indicates the value provided by the simulation data for the i-bin; E_i is the associated poissonian uncertainty; A_i is the value coming from the analytical models, that corresponds to the center of the i-bin; n is the number of the bins.

5.1 Unconditional Mass Function

For the global mass function the comparison is done between these analytical forms:
(i) Lacey & Cole 1993 mass function, eq. (3.17), for the spherical collapse, labelled as SC -spherical collapse-
(ii) Sheth & Tormen 1999 fit to the GIF simulations, eq. (4.4), labelled as FIT
(iii) Sheth & Tormen 2002 mass function, eq. (4.11), and all the other curves that descend from this equation, varying the number of terms of the Taylor expansion series, eq.(4.12), from 0 to 100, labelled as $EC_0, ..., EC_{100}$
(iv) Sheth & Tormen 2002 mass function with the entire expansion series, eq. (4.19), labelled as EC_∞.

Then, all the curves obtained by changing the natural normalization are considered: not all the distributions have the same "original" normalization, and some of them are also substantially different from the unit value (see Figure 5.1) that would represent the situation for which all the matter is bound in some haloes: this is due to the fact that the expansion series is just a "mathematical trick" introduced to obtain the progenitor mass function through an approximation of the exact solution (see Section 4.3). All the analytical functions are translated into the $\nu = \frac{\delta_c^2(z)}{S(M)}$ variable in order to obtain a degerenacy of the curves and data respect to the redshift: in this way one has a more robust statistics for each bin because can consider haloes that exist at different epochs. The conversion between the variables ν and S is provided by:

$$\nu f(\nu) = S f(S) \tag{5.2}$$

The models are compared with two simulations: the GIF2 and the Millennium, that are described in details in the Appendix. In Figure 5.2 there are the results for the GIF2 simulation: in this case, for increasing the statistics, we stack together the snapshots corresponding to: $z = 0.000$, 1.052, 2.000, 4.042. From the top-left panel to the bottom-right one, these curves are plotted: spherical collapse, GIF mass function, ST02 mass function with $|T(S)|$ truncated at the order $0, 1, 2, 5, 10$, mass function from ST02 with the entire $|T(S)|$ (infinite orders). Dotted blue lines refer to the mass functions with normalization equal to one and the blue number refers to the value of the χ^2 for that kind of curve. Solid red lines refer to unconditional mass functions with the best normalization (i.e. the normalization that minimizes the χ^2 for that model) for that kind of curve; the red number is the associated χ^2 and it is written following the form "value of χ^2 @ best normalization". In Figure 5.3 there are the results for the Millennium Simulation: in this case, we use the snapshots corresponding to: $z = 0.000$, 1.503, 3.060, 6.196, 10.073.

For both the GIF2 and the Millennium, the curve that best fit the points of simulations has a $|T(S)|$ truncated at low orders, and the normalization is higher than

χ^2_{SC}@BN	χ^2_{FIT}@BN	$\chi^2_{EC_5}$@BN	$\chi^2_{EC_\infty}$@ BN	χ^2_{BEST}@BN
236.7 @0.72	140.5@1.01	55.3@1.08	275@0.71	$EC_2$21.09@1.29
8318@0.7	5961@0.96	1973 @1.05	6036 @ 0.69	$EC_1$504.8@1.48
χ^2_{SC}@N	χ^2_{FIT}@N	$\chi^2_{EC_5}$@N	$\chi^2_{EC_\infty}$@N	
4551@1.00	146.2@1.00	1995@1.36	1394@0.5732	
$> 10^4$@1.00	6693 @1.00	$> 10^4$@1.36	$> 10^4$@0.57	

Table 5.1: In the first column, first cell (BN), the value of the best χ^2 provided by the SC model and the associated normalization; in second cell (N), the value of SC-χ^2 provided by the "original" normalization; in the second column, the χ^2s from the FIT99-model; in the third column the χ^2s from the EC_5-model and in fourth column the χ^2s provided by the EC_∞ model. In the last column, there is the best model with associated χ^2 and normalization. In each cell, the first row is the GIF2 result, the second row refers to the Millennium.

one (this is not a physical result!). In Figure 5.4 we compare the value of the χ^2s for various models (SC, FIT, EC_1,..., EC_{10}, EC_∞) with the best value, both for GIF2 and Millennium Simulation; each panel contains the results associated to the best normalization (no-crossed symbols) and those associated to the "original" normalization (crossed symbols). In table 5.1, we show the values of χ^2 provided by various models associated with the best (BN) and the original normalization (N), both for the GIF2 and the Millennium simulations.

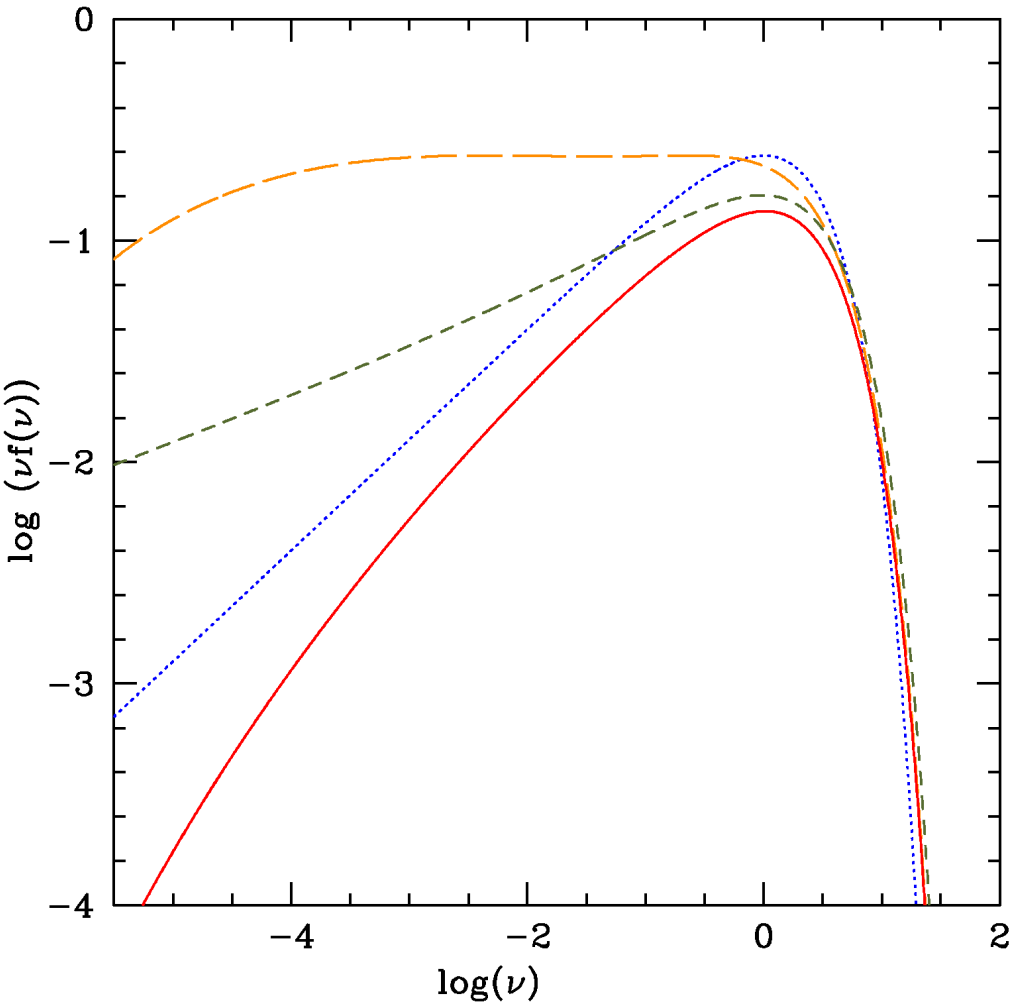

Figure 5.1: Theoretical global mass functions with their "original" normalization. Dotted blue curve refers to spherical collapse; solid red curve refers to ST02 with ∞ terms in $T(S)$; long-dashed orange curve is the ST02 with zero orders; short-dashed green curve is the ST99 fit to GIF simulation. The curves with orders between 0 and ∞ are not shown, but they take intermediate positions between the red and orange ones.

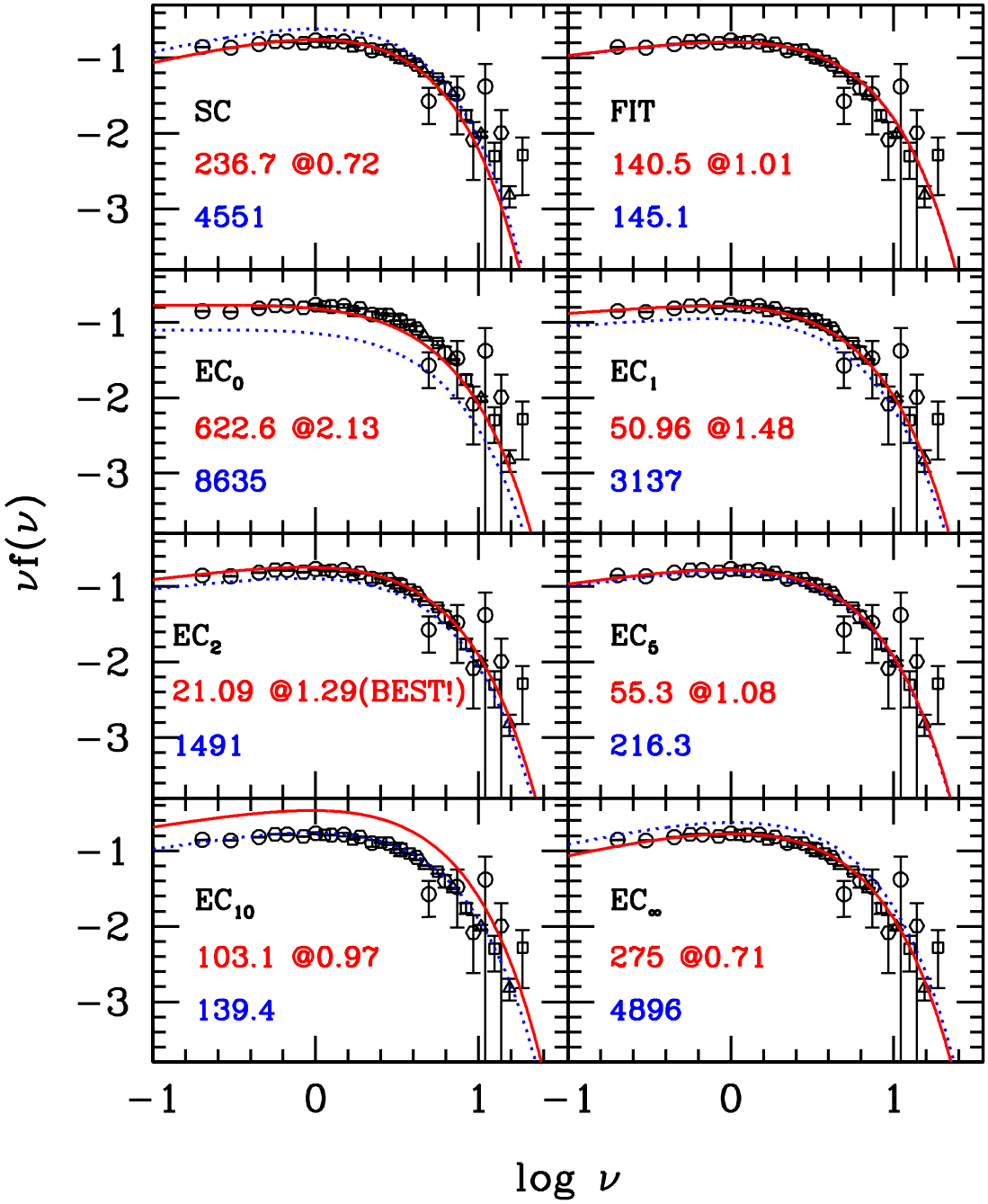

Figure 5.2: Unconditional mass function from GIF2 simulation (various black symbols for different redshifts ($z = 0.000$, 1.052, 2.000, 4.042) and poissonian error bars) and from different theoretical models. Dotted blue curves refer to distributions with a normalization equal to one; solid red curves refer to distributions with a normalization that provides the best fit to the data. The first red number is the value for the "χ^2@best normalization"; the second blue number is the value for the "χ^2 for the unit normalization". Here, EC_2 provides the best model among all.

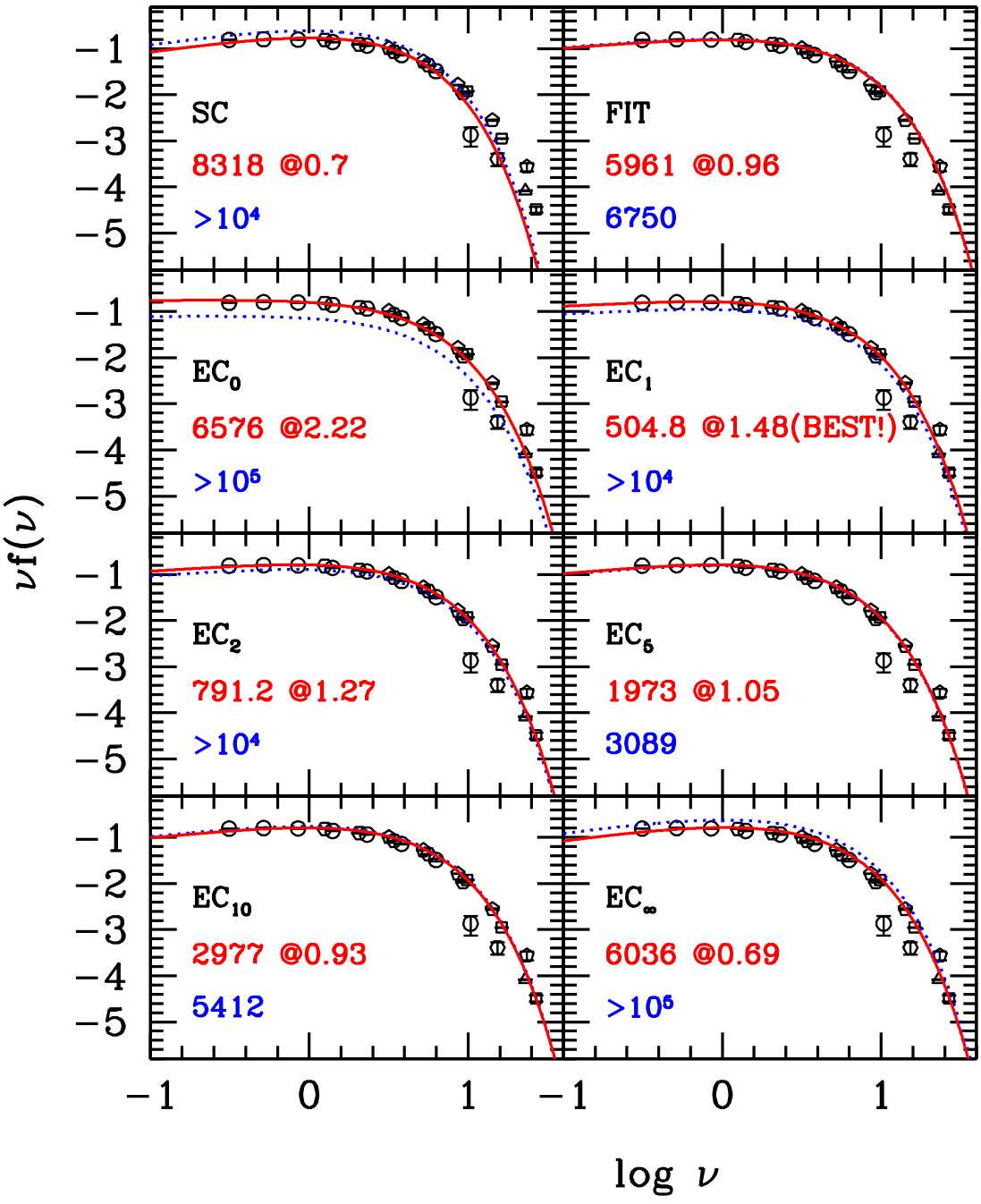

Figure 5.3: The same as in Figure 5.2, but using the Millennium Simulation at redshifts: $z = 0.000$, 1.503, 3.060, 6.196, 10.073. Here the best model among all is the EC_1.

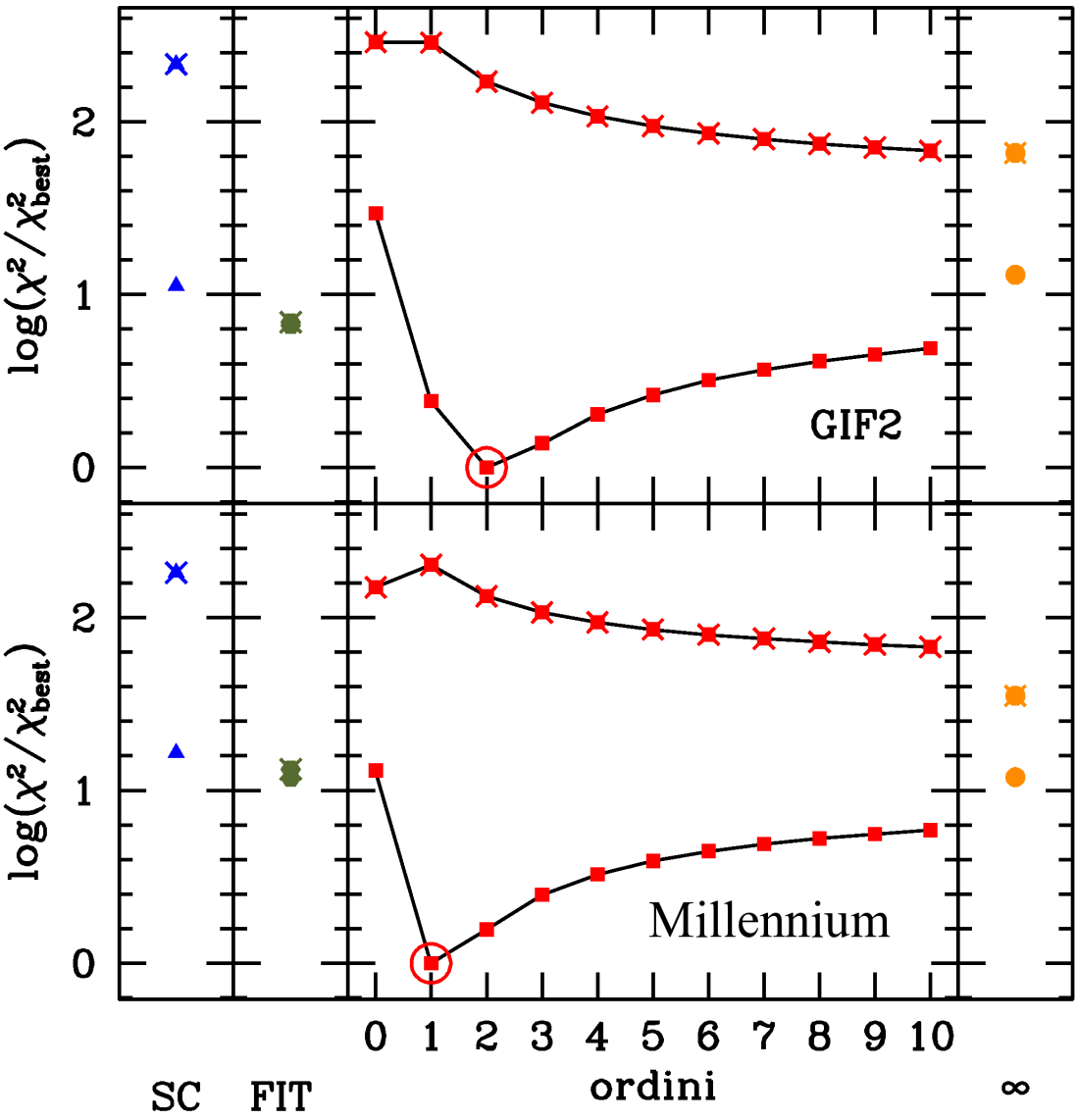

Figure 5.4: Upper panel: χ^2 associated to various models keeping the original normalization (crossed symbols) and with "best" normalization (no-crossed symbols), all compared with the "best" χ^2 (red circle). Blue triangles refers to spherical-collapse model; green exagones to the fitting formula ST99; red squares are results coming from various orders (from 1 to 10) of series expansion in eq. (4.11) and orange dots are the results from ∞ orders. This data refer to the GIF2 simulation.
Lower panel: the same as in the upper panel, but for the Millennium simulation.

z	M^* in $M_\odot$units	z	M^* in $M_\odot$units
0.00	8.956×10^{12}	0.52	1.829×10^{12}
0.06	7.518×10^{12}	1.05	3.505×10^{11}
0.13	6.120×10^{12}	2.00	2.155×10^{10}
0.27	3.973×10^{12}	4.04	1.382×10^{8}

Table 5.2: The value of M^* for a number of redshifts.

5.2 Progenitor Mass Function

The analytical equations for the progenitor mass function come from:
(i) LC93, eq. (3.25) (SC);
(ii) ST02, eq. (4.15), and all the other curves that descend from this equation, varying the numbers of terms of the Taylor expansion series, eq. (4.16), from 0 to 100 ($EC_0, ..., EC_{100}$);
(iii) ST02 with the entire expansion series, eq. (4.21) (EC_∞).
This distributions are considered in the variable M, instead of S. Hereafter, we use this notation: $M_1 \to m$ for the mass of the progenitor; $M_2 \to M$ for the mass of the halo at $z = 0$.

Then we consider all the curves obtained by changing the natural normalization of these models. The fitting analysis is the same as for the unconditional mass function, but here we used only the data provided by the GIF2 simulation. We decided to show the result for the progenitors -considered at various redshifts- of haloes that exist at $z = 0$, with mass in the intervals: $M \in [0.125M^*, 0.5M^*]$, labelled as $M = 0.25M^*$, $M \in [0.5M^*, 2M^*] \leftrightarrow M = M^*$, $M \in [2M^*, 8M^*] \leftrightarrow M = 4M^*$. M^* is the value of the mass determined imposing $\delta(t)^2 = S(M)$; in Table 5.2 there is the value of M^* for different redshifts.

A progenitor, in this case, is defined as a halo that contains the particles that are part of the considered halo at $z = 0$. To identify the progenitor, it is necessary to trace back in time the history of the single particles in the simulation. Contrary to the model, that contemplates only mergers without fragmentations, in the simulation one can notice the phenomenon of the break of a halo due to a merger: in this situation a halo contribute to the formation of another halo through merger events only with a limited number of its particles. So we are in the context in which a structure at $z = 0$ has more than one progenitor at another redshift, but the sum of the masses of all these progenitors is greater than the mass of the descendant object. In order to be consistent with the theory, we decided to label as "mass of the progenitor" the amount of mass actually donated to the descendant.

The theoretical curves are traced replacing the mass M of the halo at $z = 0$ with the mean value of the masses of haloes in each of the three intervals considered for the simulation data: $M \in [0.125M^*, 0.5M^*]$, $[0.5M^*, 2M^*]$, $[2M^*, 8M^*]$.

In the Figures 5.5, 5.6, 5.7, we show the results for 7 different redshifts ($z = 0.062$, 0.127, 0.271, 0.521, 1.052, 2.000, 4.042) of progenitors with mass m of a halo at $z = 0$, with mass M equal to $0.25M^*$, M^*, $4M^*$ respectively. Black dots, with poissonian error bars, represent the fraction of mass in progenitors of mass m vs the ratio of progenitor mass over halo mass $\log(m/M)$ provided by the simulation; dotted blue curves refers to SC; short dashed red lines refers to the ellipsoidal distribution with $|T(s|S)|$ truncated at 5^{th} order; solid orange ones describe EC_∞ (these lines often "hide" the red ones); long dashed green lines are the best matches to the data: they can represent the eq. (3.25) with a different normalization, or eq. (4.15) with free order of the expansion series and free normalization.

5.2.1 Quantitative analysis of χ^2

In order to associate the green curves (best models) of Figures 5.5, 5.6, 5.7 to one model or another, we show the comparison of the χ^2 associated to the best curve for a particular model (i.e. the curve describing SC with best normalization or the $EC_{0,\ldots,100,\infty}$ with the best normalization) with the χ^2 associated to the best fit among all, for a given reshift.

Figure 5.8, 5.9, 5.10 show the results for progenitors of haloes of mass $M = 0.25M^*$, $M = M^*$, $M = 4M^*$ respectively. Various panels on each figures represents the same progenitor-redshifts considered in the previous plots. The x-axis is divided into three parts: the left one (blue triangles) represents the curve associated to the spherical collapse model, for the best normalization; the central part (red squares) of the plot shows the results for the ellipsoidal progenitor mass function with $|T(s|S)|$ truncated at orders 0 to 10; the right panel (orange crossed-dots) of the plot considers the entire expansion series. On the y-axis we plot the ratio of the various χ^2 over the best χ^2 for that particular redshift, on a logarithmic scale. The best model is indicated by a green circle and has obvioulsy a value equal to zero on the y-axis.

There is a first result shown here: when the ellipsoidal model provide the best fit, the difference between the best χ^2 and the EC_∞-χ^2 is very small: so the error made assuming the progenitor mass function with infinite orders in the Taylor expansion series is small. Another important feature of these plots is the evidence that the curves coming from the spherical collapse theory (but with various normalizations) better match the progenitor mass function around $z = 0.5$ and $z = 1$: one can see, that, at those reshifts, the cut off for massive progenitors begin to be visible. We think that the distributions provided

by the spherical collapse have a shape that follows better that exponential cutoff: in fact, looking at the mass functions, one can see that the ST99 fit or the various EC are "flatter" than the SC. Maybe, using a larger simulation, one can find that this trend appear also for lower progenitor redshift where the cut off can be displayed.

5.3 Fitting the flat part of the function: χ^2 without $(m/M) > 0.5$

The χ^2 technique is a global analysis to find the best curve that approximates a set of data, so we obtain curves that "on average" are the best match; in this "average", the points of the simulation that have a higher weight are the ones with smaller error bars and higher y-value: considering that we start from a limited number of shapes, we can find situations where the best curve does not fit well all the points, but mostly those that have a higher weight. Since the ellipsoidal model fails expecially at large m/M, we tried also to fit the progenitor mass function without the high-mass tail, and excluding the points at $m/M > 0.5$. The results are shown in Figures 5.11, 5.12, 5.13, where labels, colors and marks are the same of Figures 5.5, 5.6, 5.7, and in Figures 5.14, 5.15, 5.16, similar to Figures 5.8, 5.9, 5.10.

We found that, excluding from the fit all points at $m/M > 0.5$, the ellipsoidal model becomes almost always the best one. The previous consideration about the similarity between the the best order and the "∞" order is still true, except at low progenitor-redshifts.

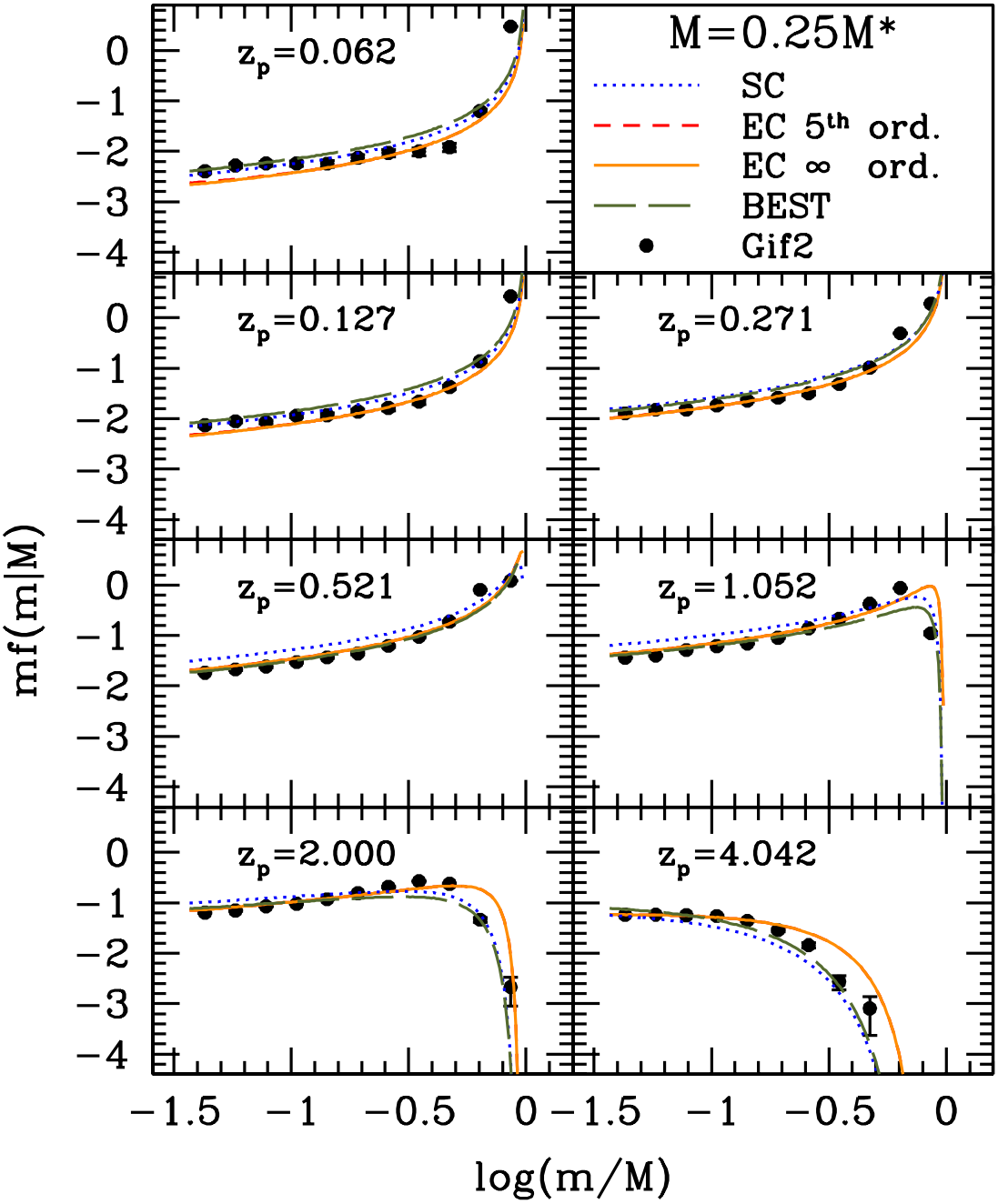

Figure 5.5: Progenitor mass function for haloes of mass $M = 0.25M^*$ at $z = 0$; progenitors are considered at 7 different redshifts: $z = 0.062$, 0.127, 0.271, 0.521, 1.052, 2.000, 4.042 . Dotted blue curves refer to Spherical Collapse; short dashed red lines to Ellipsoidal Collapse with 5 orders in the Taylor series expansion; solid orange to ellipsoidal collapse with all orders; long dashed green to the best fit; dots represent GIF2 simulations with poissonian error bars. On the x-axis: the ratio between the progenitor mass over halo mass.

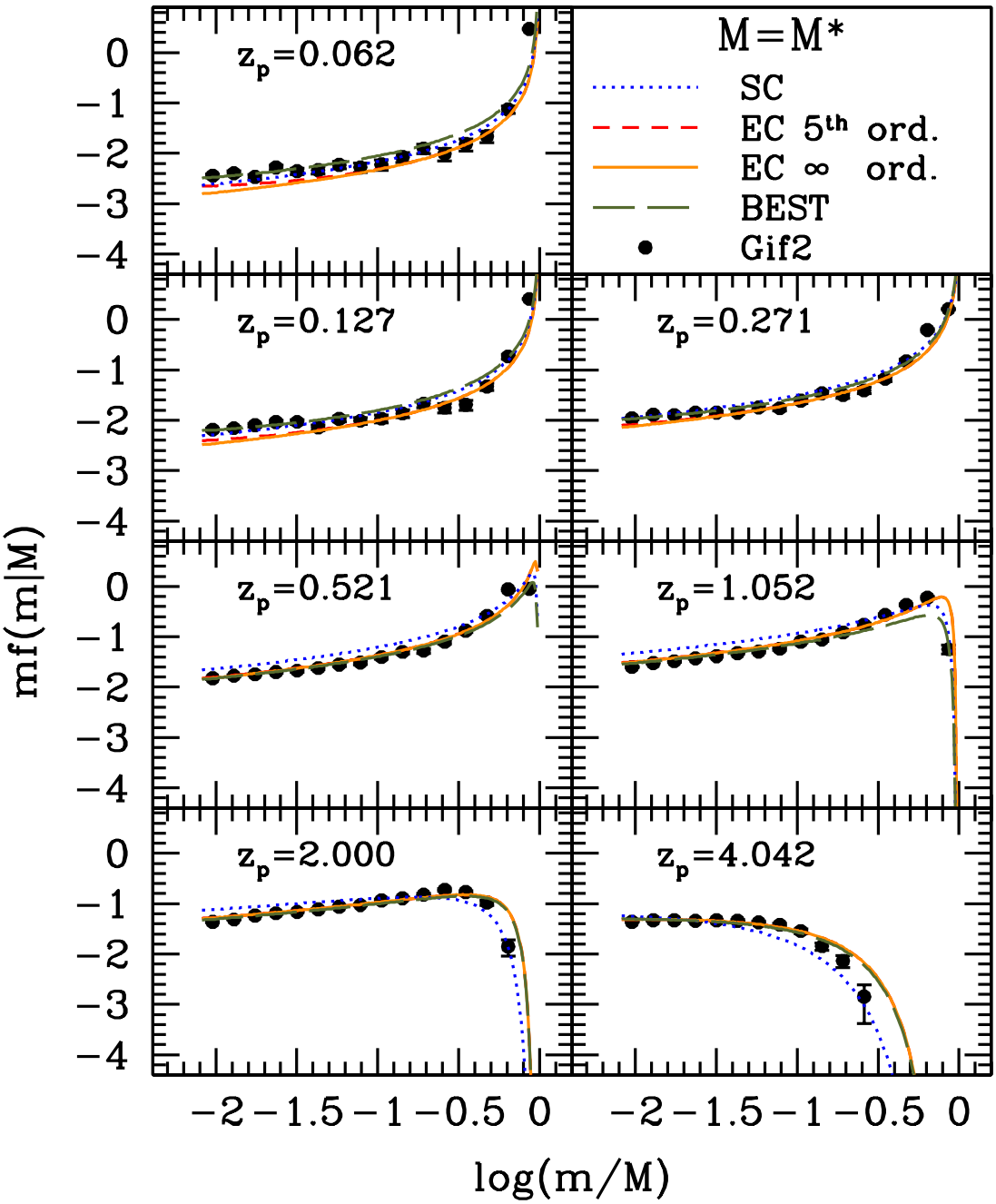

Figure 5.6: The same as Fig. 5.5, for haloes of mass $M = M^*$.

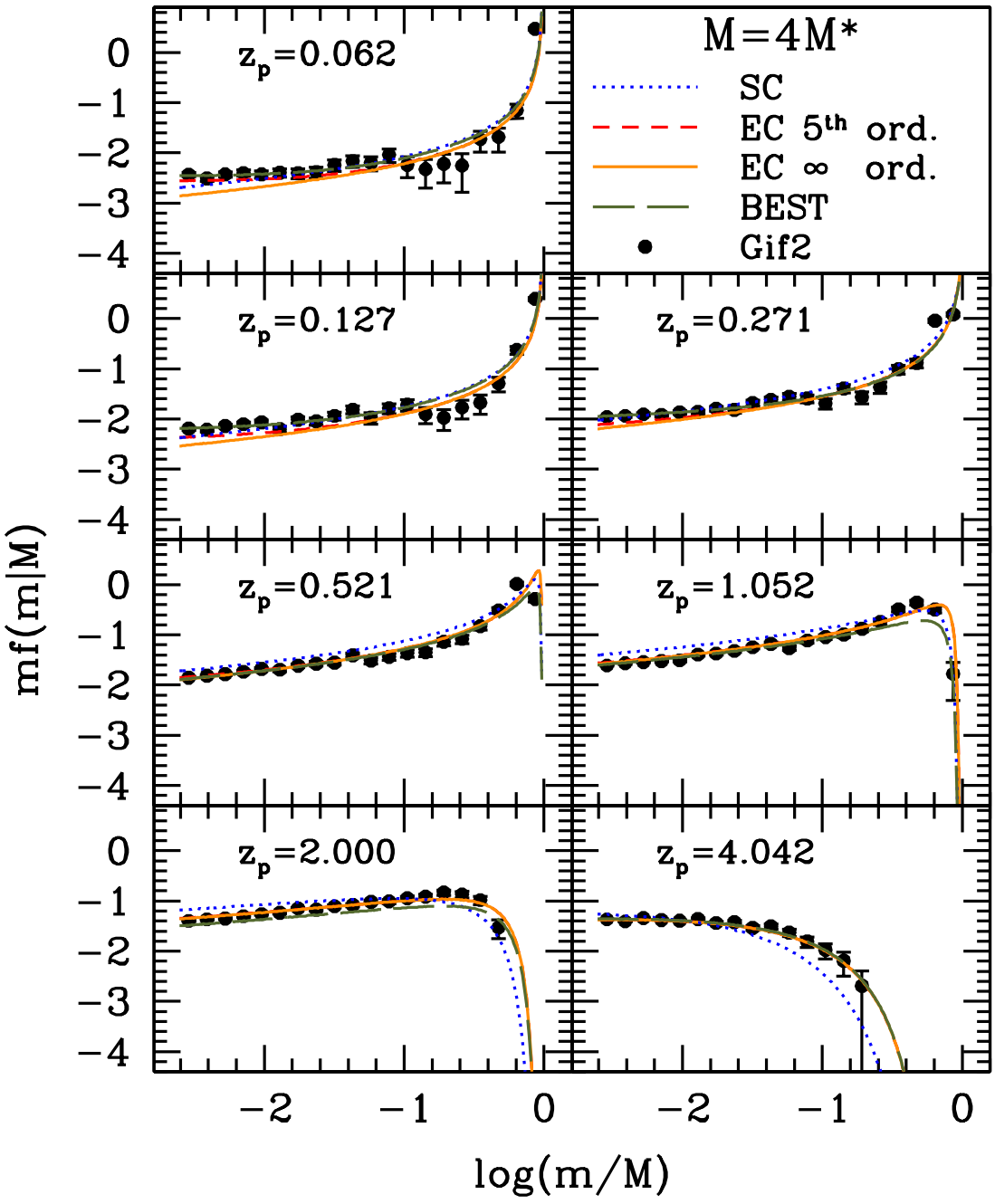

Figure 5.7: The same as Fig. 5.5, for haloes of mass $M = 4M^*$.

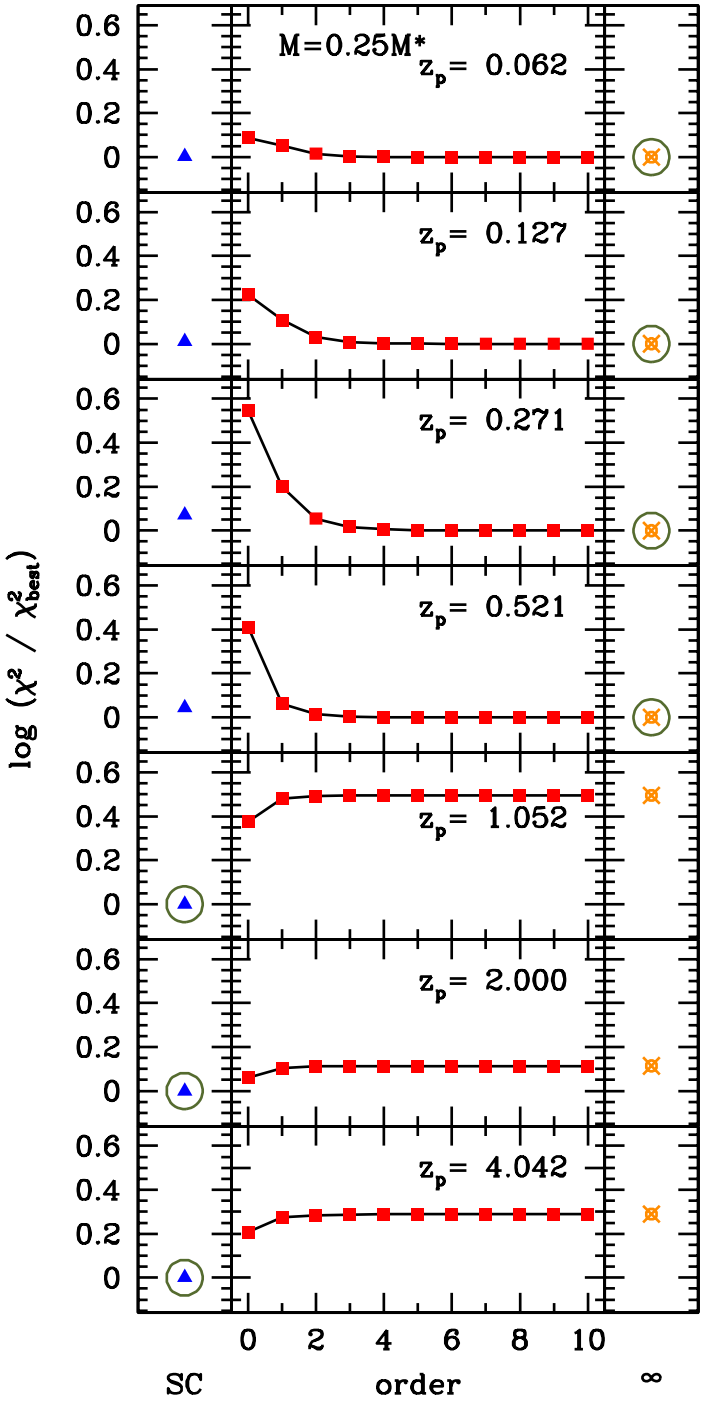

Figure 5.8: χ^2 for 7 redshifts (from top to bottom: $z = 0.062$, 0.127, 0.271, 0.521, 1.052, 2.000, 4.042) of progenitors of a halo of mass $M = 0.25M^*$. Blue triangles refer to (SC / best-χ^2); red squares to (EC (orders from 0 to 10) / best-χ^2); orange crossed dots to (EC all orders / best-χ^2). The green circles show the best χ^2s.

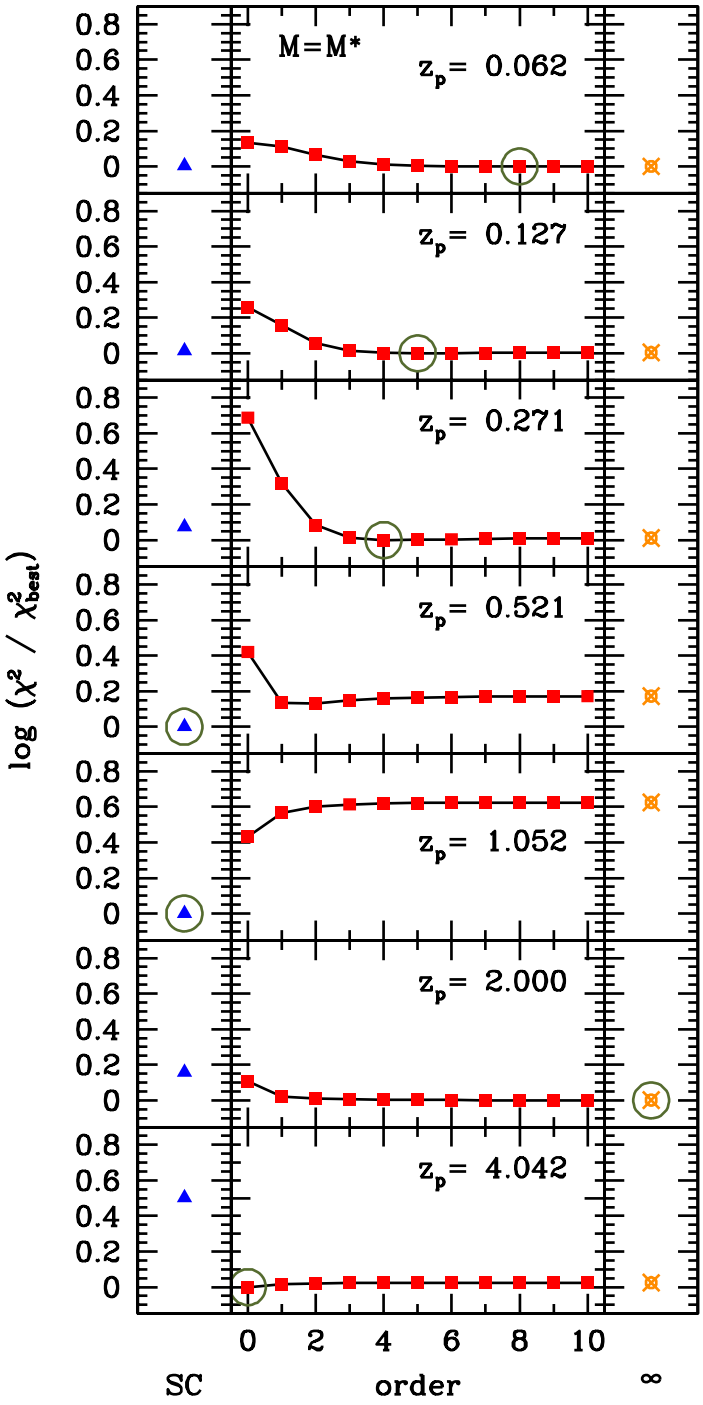

Figure 5.9: The same as Fig. 5.8, for haloes of mass $M = M^*$.

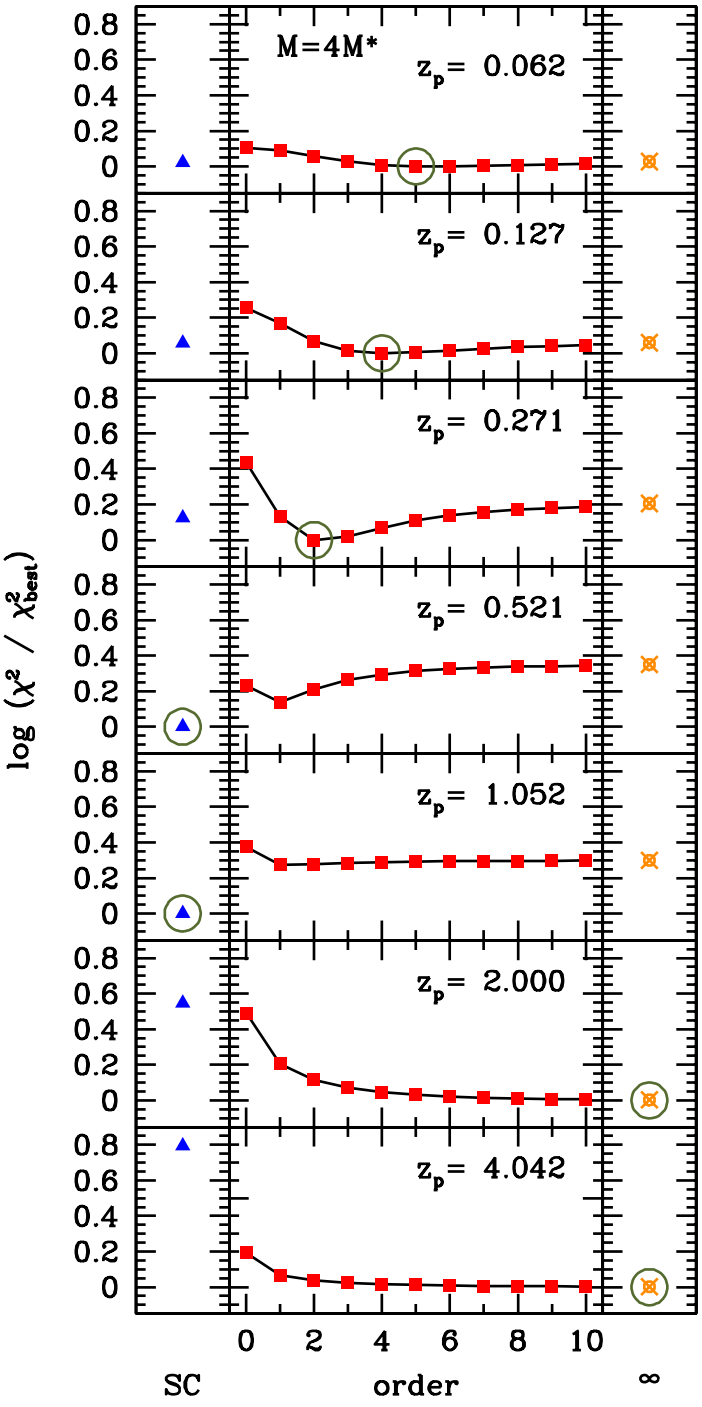

Figure 5.10: The same as Fig. 5.8, for haloes of mass $M = 4M^*$.

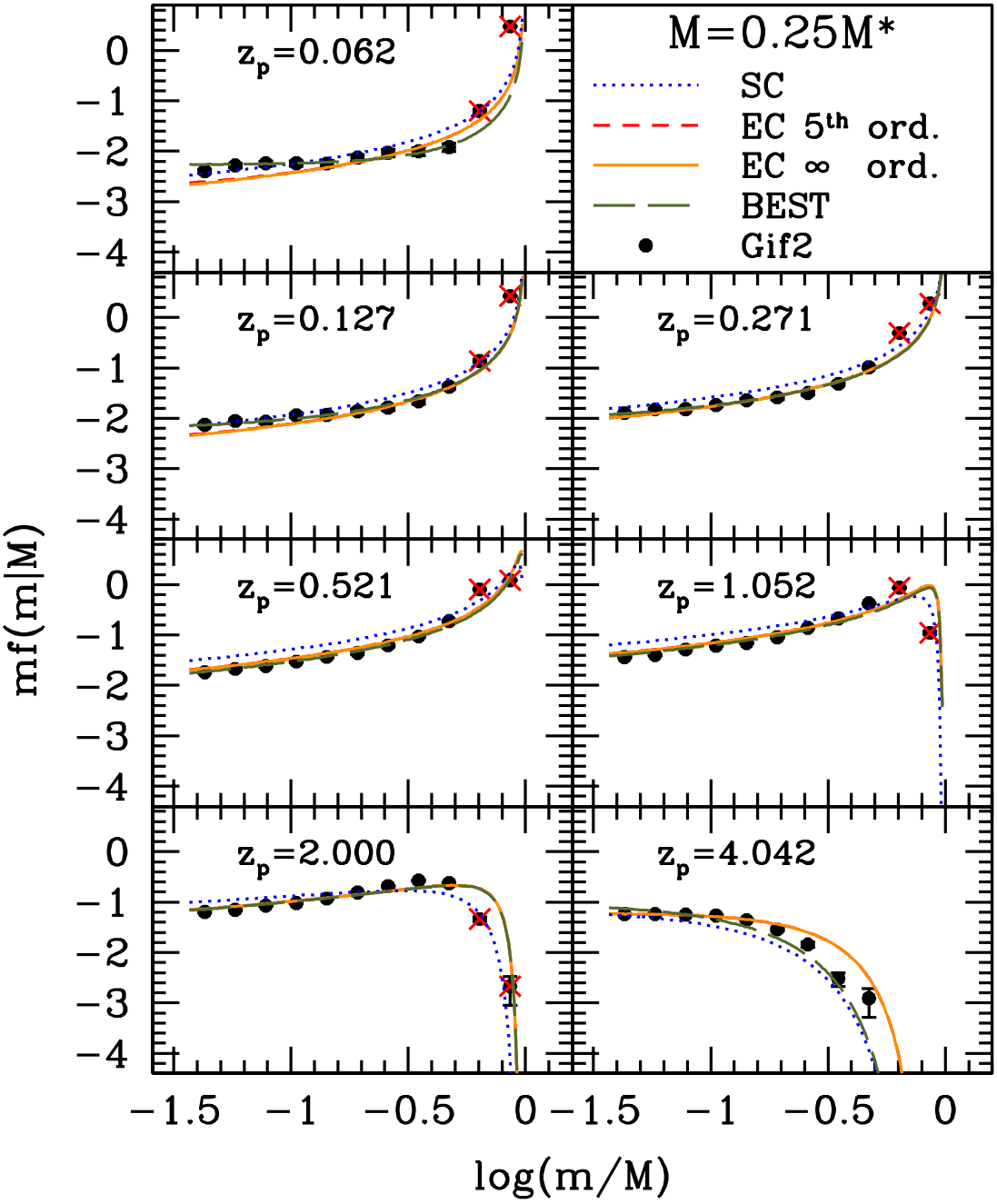

Figure 5.11: Progenitor mass function for haloes of mass $M = 0.25M^*$ at $z = 0$; progenitors are considered at 7 different redshifts: $z = 0.062$, 0.127, 0.271, 0.521, 1.052, 2.000, 4.042. Dotted blue curves refer to Spherical Collapse; solid red to Ellipsoidal Collapse with 5 orders in the Taylor series expansion; long-dashed orange to ellipsoidal collapse with all orders; dots represent GIF2 simulations with poissonian error bars. On the x-axis: the ratio between the progenitor mass over halo mass. The points marked with red crosses indicate the mass-bins that do not contribute to the calculation of χ^2.

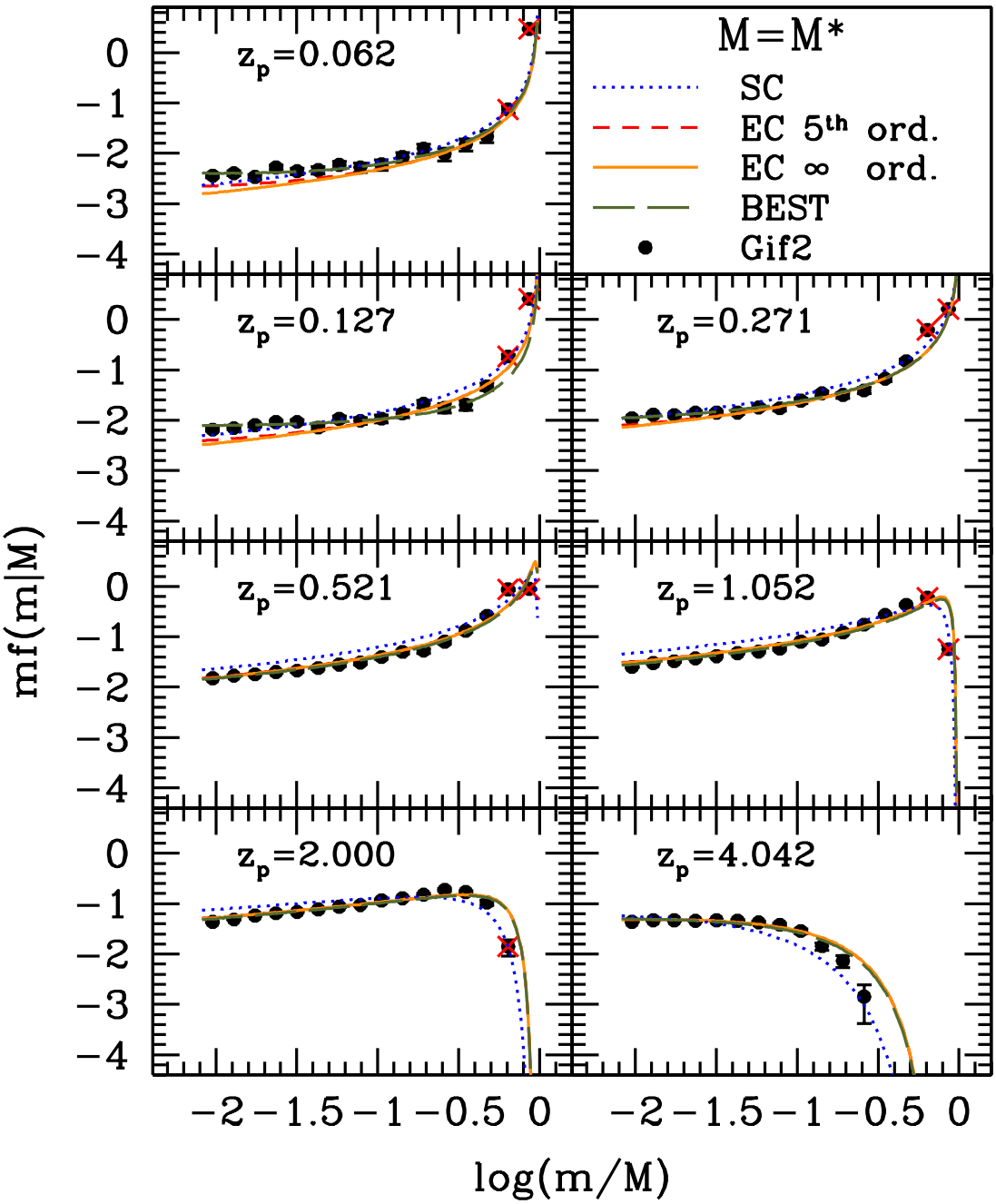

Figure 5.12: The same as Fig. 5.11, for haloes of mass $M = M^*$.

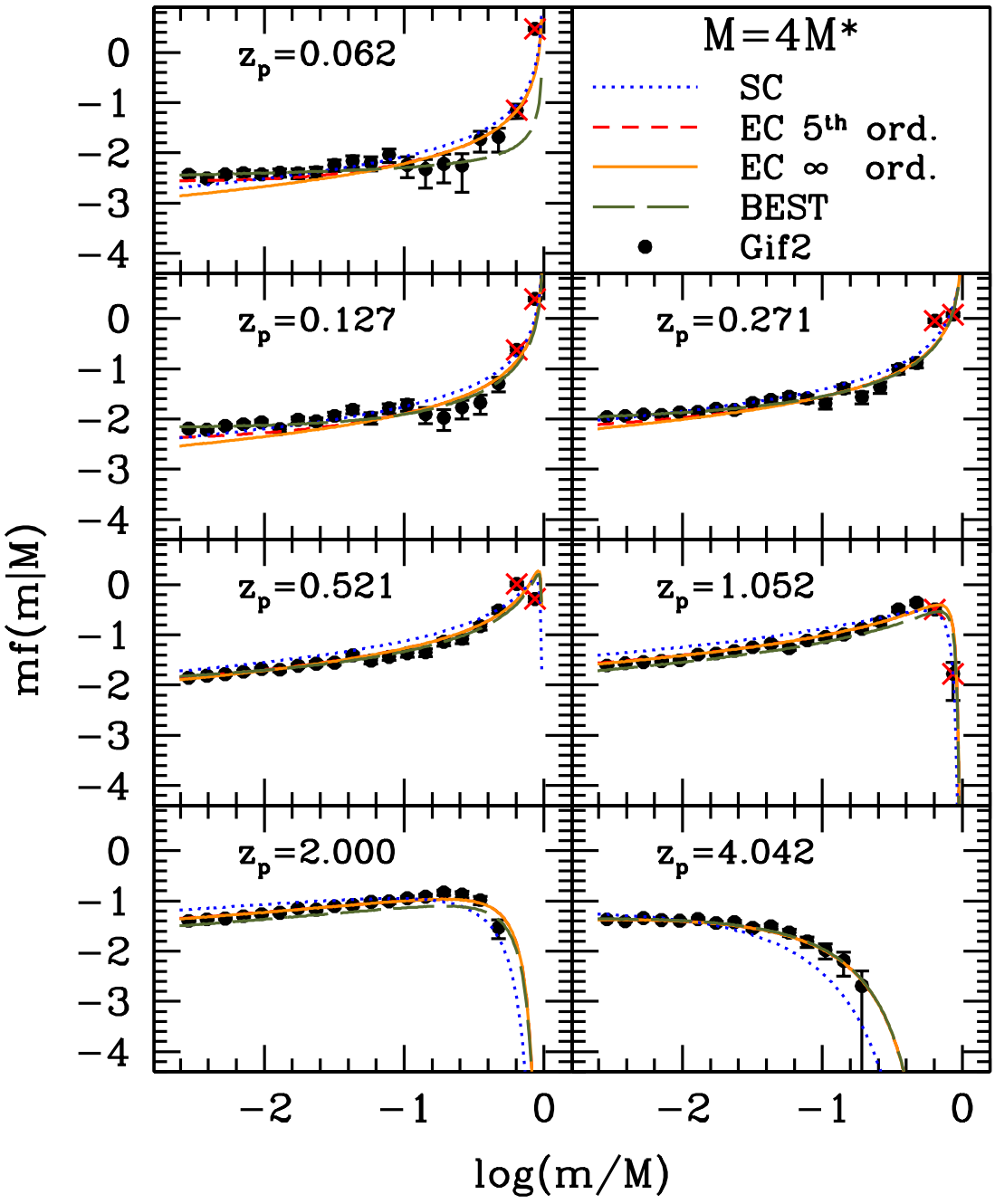

Figure 5.13: The same as Fig. 5.11, for haloes of mass $M = 4M^*$.

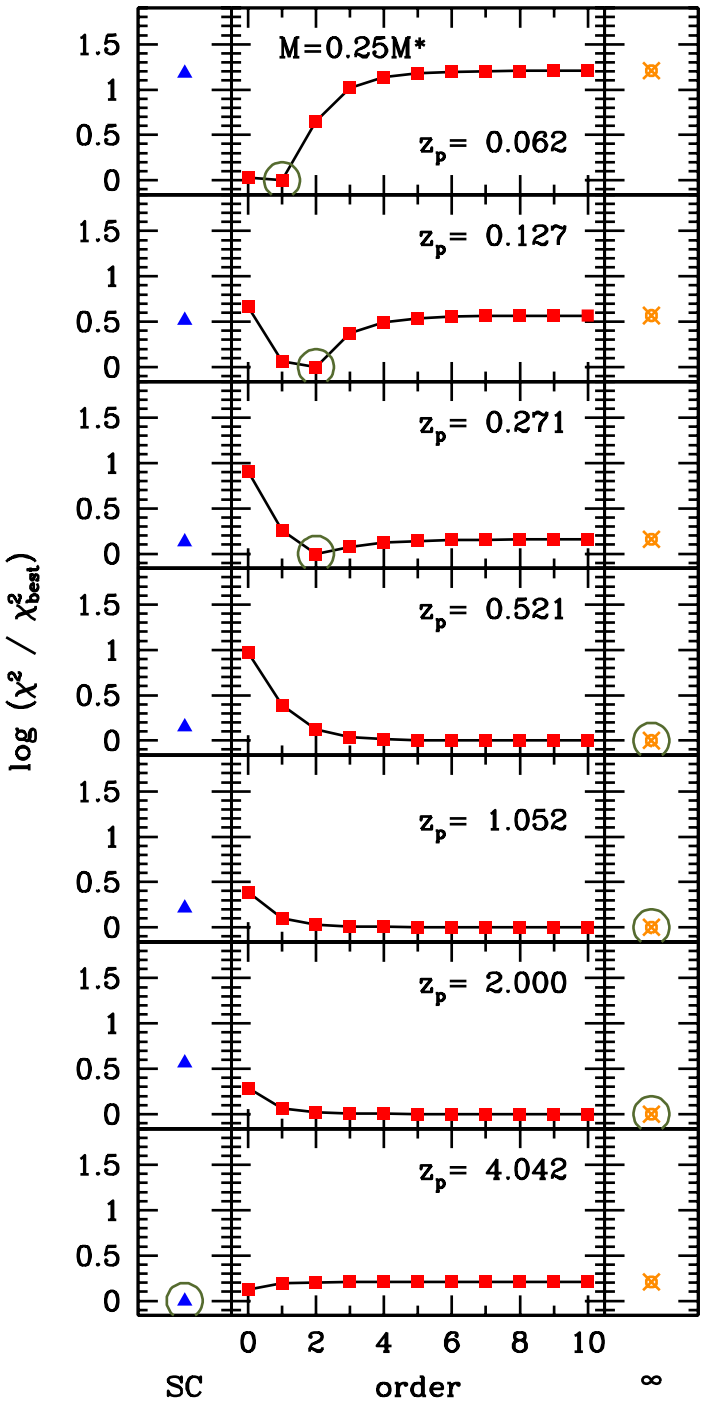

Figure 5.14: The same as Figure 5.8, but excluding the contribution of high mass progenitors ($m/M > 0.5$).

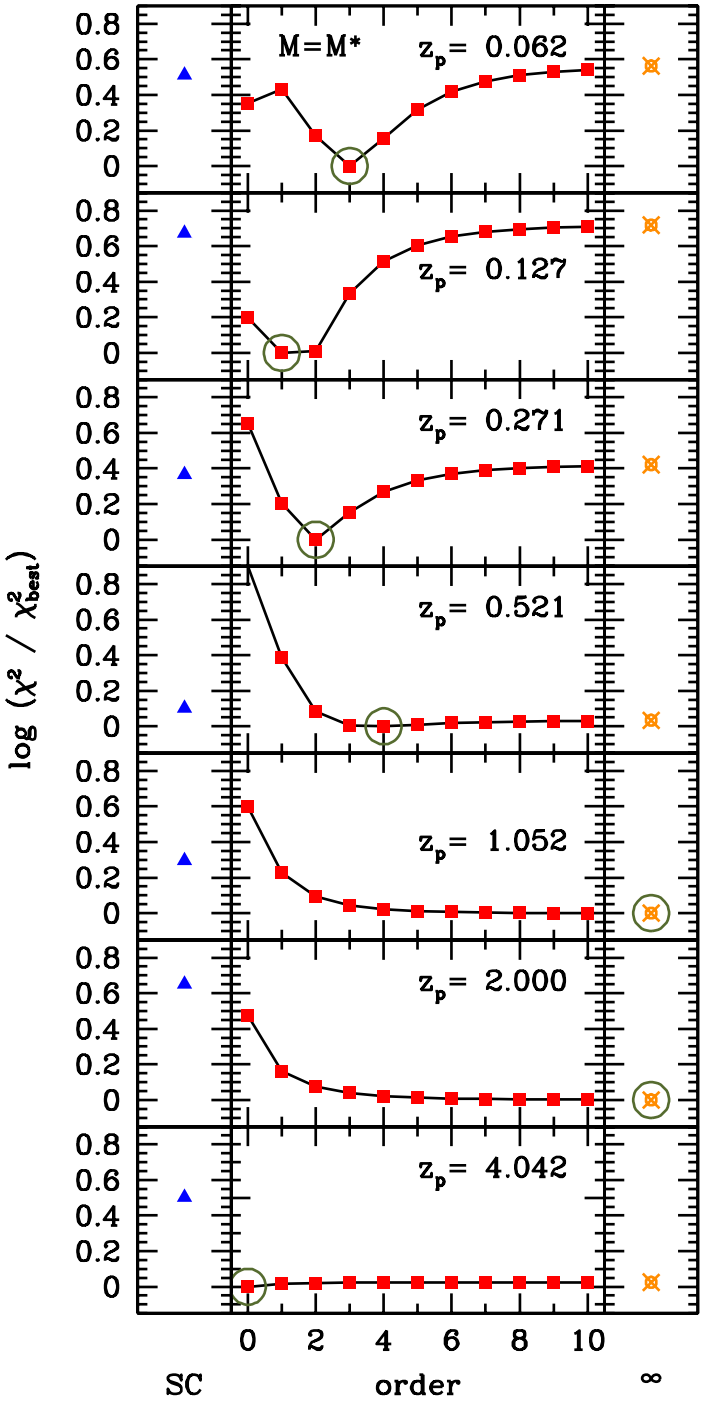

Figure 5.15: The same as Figure 5.8, for haloes of mass $M = M^*$, but excluding the contribution of high mass progenitors $(m/M > 0.5)$.

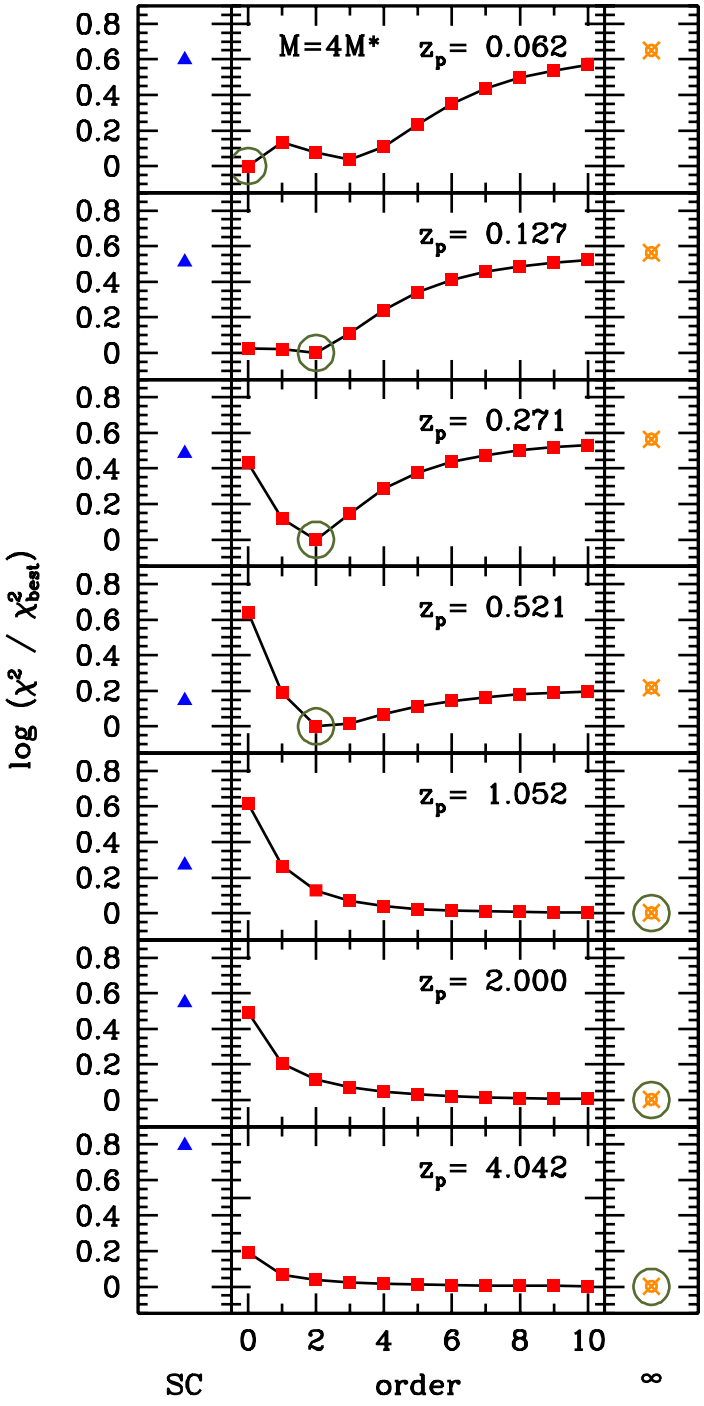

Figure 5.16: The same as Figure 5.8, for haloes of mass $M = 4M^*$, but excluding the contribution of high mass progenitors ($m/M > 0.5$).

5.4 Descendant Mass Function

The analytical equations for the descendant mass function are:
(i) for the SC, eq. (3.27) by LC93;
(ii) eq. (4.22), with $T(S) = T_0(S)$ (zero orders) for the unconditional mass function and all the other curves that descend from this equation, varying the numbers of terms of $T(S_1|S_2)$ for the progenitor mass function from 0 to 100;
(iii) eq. (4.22), with $T(S) = T_\infty(S)$ (all the series) for the unconditional mass function and all the other curves that descend from this equation, varying the numbers of terms of $T(S_1|S_2)$ for the progenitor mass function from 0 to 100;
(iv) eq. (4.22), with $T(S) = T_0(S)$ (zero orders) for the unconditional mass function and the whole $T(S_1|S_2)$ for the progenitor mass function;
(v) eq. (4.22), with $T(S) = T_\infty(S)$ (all the series) for the unconditional mass function and the whole $T(S_1|S_2)$ for the progenitor mass function.
This distributions are considered in the variable M, instead of S. Hereafter, we use this notation: $M_1 \to m$ for the mass of the halo at different redshifts; $M_2 \to M$ for the mass of the descendant at $z = 0$.

Then we consider all the curves obtained by changing the natural normalization of these models. We noted that the differences between the curves with T_0 and T_∞ are very small, and there is a degeneracy between type (ii) curve and corresponding type (iii) with different normalization (the same for type (iv) and (v)). For this reason, we consider only type (iii) and (v) curves with the whole expansion series for global mass function. Also for this distribution, we perform a χ^2 fitting analysis, using the data provided by the GIF2 simulation. We show the results for the descendant mass function at $z = 0$ of haloes constrained at different previous redshifts, i.e. we fix different ranges of masses calculated as fraction of M^* for different redshifts and we put the descendants always at present time. In this case, the mass interval for the haloes at different redshifts are not always the same, because, especially at high z, it is difficult to have a robust statistics for small objects. In Table 5.4 the used intervals for each redshift are shown.

Following the theory, a descendant is defined as the halo resulting from the mass-conservative merging between two or more progenitors. As already described for the progenitors, in the simulation, a halo can be the progenitor of more than a descendant, because of fragmentation. For this study, we trace every particles from the initial, to the final snapshot and we consider as "descendant" of a halo, the object that received more than 50% of the mass of the progenitor (raising this threshold, results don't change significantly). The mass of the descendant is its total mass. Also in this case, the theoretical curves are traced replacing the mass m of the halo with the mean value of the masses of haloes in the three intervals of the simulation.

$z = 0.062$	$z = 0.127$	$z = 0.271$	$z = 0.521$
$[0.125M^*, 0.5M^*]$	$[0.125M^*, 0.5M^*]$	$[0.125M^*, 0.5M^*]$	$[0.125M^*, 0.5M^*]$
$[0.5M^*, 2M^*]$	$[0.5M^*, 2M^*]$	$[0.5M^*, 2M^*]$	$[0.5M^*, 2M^*]$
$[2M^*, 8M^*]$	$[2M^*, 8M^*]$	$[2M^*, 8M^*]$	$[2M^*, 8M^*]$

$z = 1.052$	$z = 2.000$	$z = 4.042$
$[0.25M^*, 1M^*]$	$[5M^*, 20M^*]$	$[1000M^*, 4000M^*]$
$[0.5M^*, 2M^*]$	$[20M^*, 80M^*]$	$[4000M^*, 16000M^*]$
$[2M^*, 8M^*]$	$[80M^*, 320M^*]$	$[12000M^*, 48000M^*]$

Table 5.3: For each redshift at which we locate the haloes, the intervals of masses within which we choose the haloes are shown.

In Figure 5.17, 5.18, 5.19, we show the results for the descendant mass function, fixing the haloes at 7 different redshifts ($z = 0.062$, 0.127, 0.271, 0.521, 1.052, 2.000, 4.042), and considering the descendants at $z = 0$; the halo mass m corresponds to the three intervals defined in Table 5.4. Black dots, with poissonian error bars, represent the fraction of mass in descendants of mass M vs the ratio between descendant mass and halo mass, $\log(M/m)$, provided by the GIF2 simulation; dotted blue curves refers to SC; short dashed red lines refers to the ellipsoidal distribution with the entire $|T(s|S)|$; solid orange ones describe EC_0; long dashed green lines are the best matches to the data.

In Figure 5.20, 5.215.22, we show the comparison of the χ^2 associated to the best curve for a particular model (i.e. the curve describing SC with best normalization or the $EC_{0,\ldots,100,\infty}$ with the best normalization) with the χ^2 associated to the best fit among all, for a given reshift. The three figures show the result for different ranges of halo masses; in each plot, from top to bottom, there are the results for halo kept at redshift $z = 0.062$, 0.127, 0.271, 0.521, 1.052, 2.000, 4.042. The x-axis is divided into three parts: the left one (blue triangles) represents the curve associated to the spherical collapse model, for the best normalization; the central part (red squares) of the plot shows the results for the ellipsoidal progenitor mass function with $|T(s|S)|$ truncated at orders 0 to 10; the right panel (orange crossed-dots) of the plot considers the entire expansion series. On the y-axis we plot the ratio of the various χ^2 over the best χ^2 for that particular redshift, on a logarithmic scale. The best model is indicated by a green circle and has obvioulsy a value equal to zero on the y-axis.

From the plots of the descendant mass function, and from the analysis of the χ^2, we show that the ellipsoidal model provides the curves that best match the data; it happens for almost all the redshifts for the lower and upper intervals of halo masses. For the

intermediate halo mass interval, in three cases the spherical model is the best one. In all the cases when the EC_∞ is not the best choice, it provides a model that differs from the best one by a small amount. This means that one can use the the ellipsoidal dynamics (that is almost always the best representation) with the simplest analytical formulas (the ones with the whole Taylor expansion series), without making any big error, for every redshifts and mass ranges.

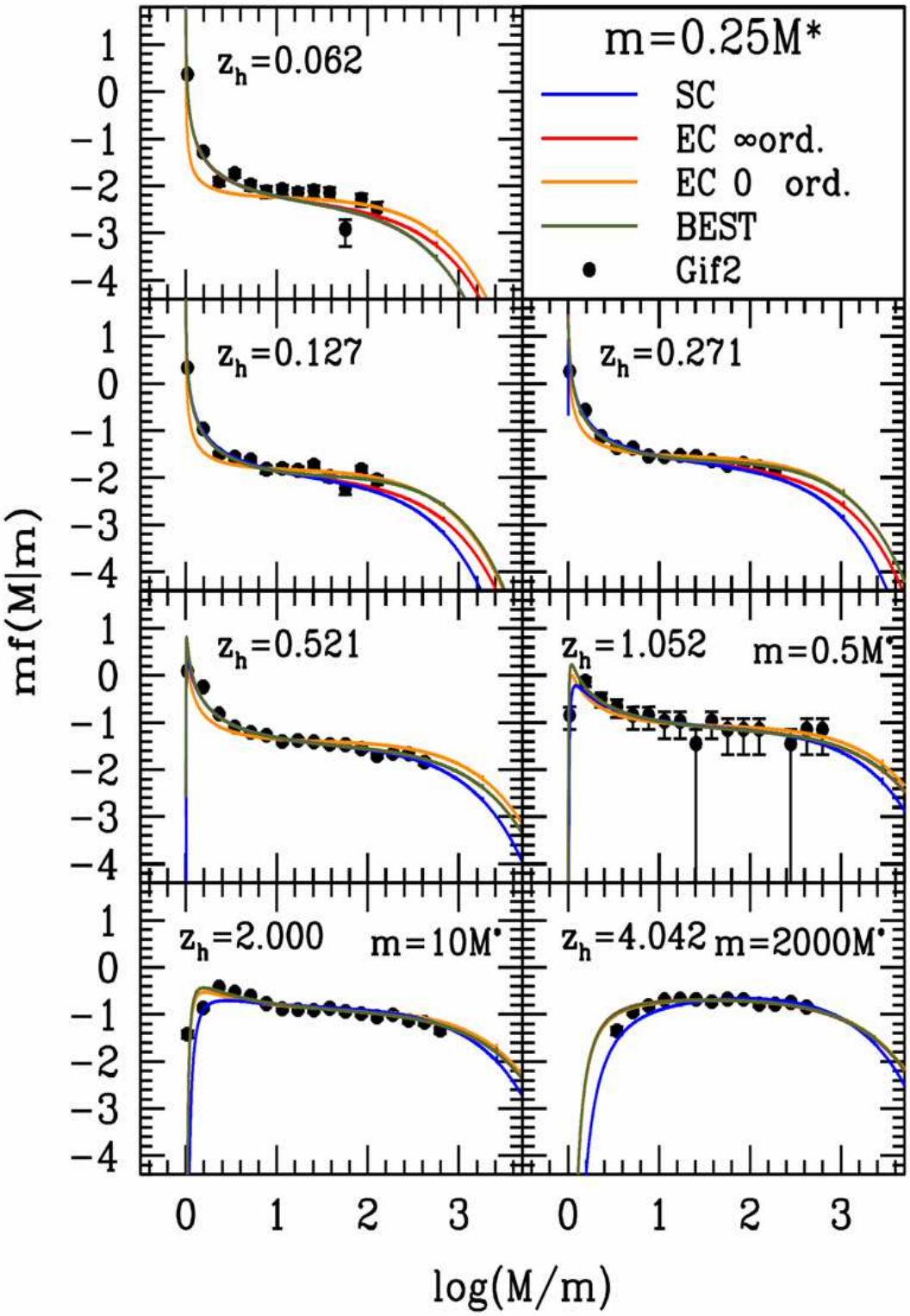

Figure 5.17: Descendant mass function for haloes of mass $m = 0.25M^*$ at $z = 0.062$, 0.127, 0.271, 0.521, $m = 0.5M^*$ at $z = 1.052$, $m = 10M^*$ at $z = 2.000$, $m = 2000M^*$ at $z = 4.042$; all the descendants are computed at $z = 0$. Blue curves refer to Spherical Collapse; orange curves to Ellipsoidal Collapse with 0 orders in the Taylor series expansion; red to Ellipsoidal Collapse with all orders; green to the best fit; dots represent GIF2 simulations with poissonian error bars. On the x-axis: the ratio between the progenitor mass over halo mass.

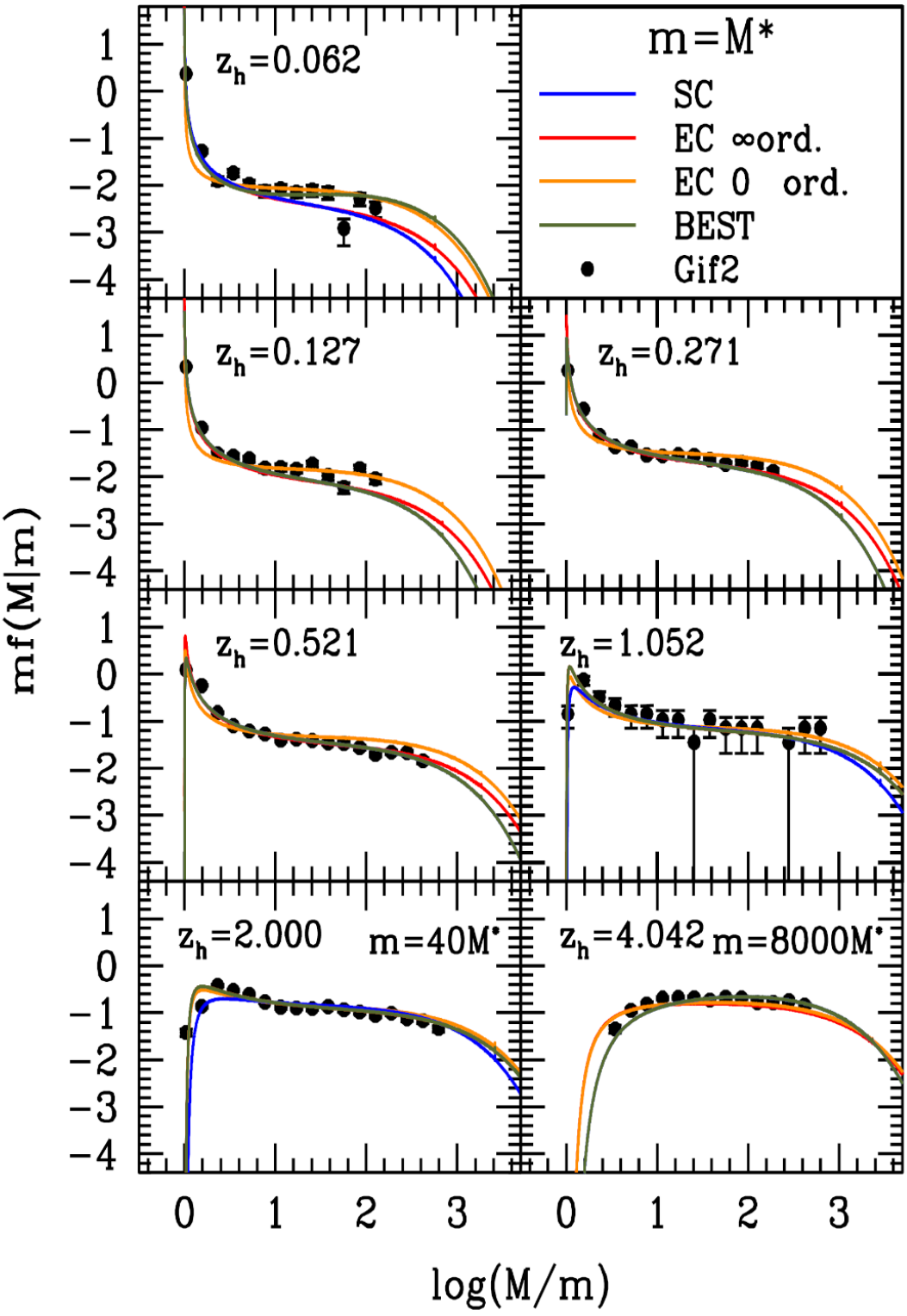

Figure 5.18: The same as 5.17, but with this halo-masses: $m = 1M^*$ at $z = 0.062$, 0.127, 0.271, 0.521, 1.05, $m = 40M^*$ at $z = 2.000$, $m = 8000M^*$ at $z = 4.042$.

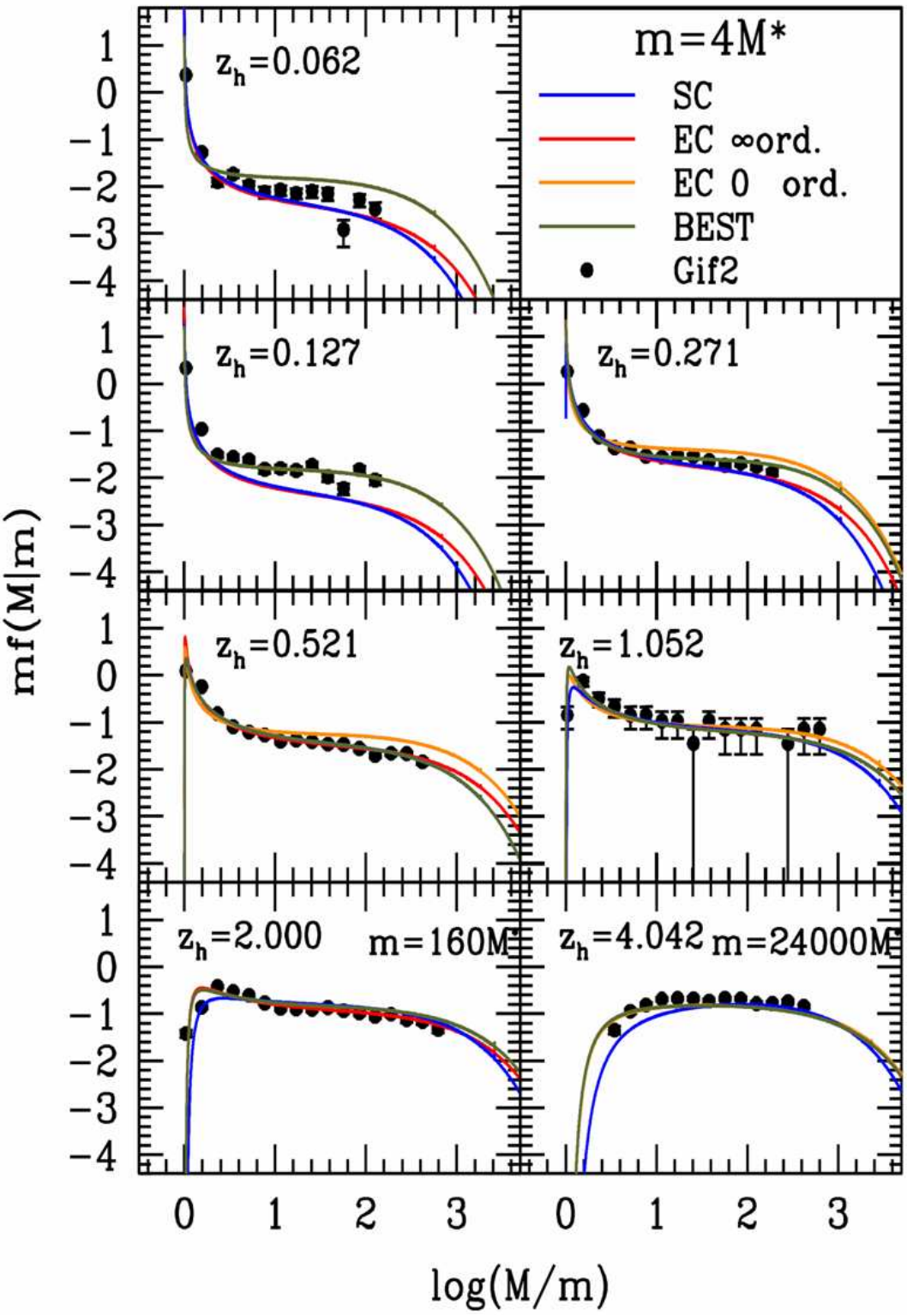

Figure 5.19: The same as 5.17, but with this halo-masses: $m = 4M^*$ at $z = 0.062$, 0.127, 0.271, 0.521, 1.05, $m = 160M^*$ at $z = 2.000$, $m = 24000M^*$ at $z = 4.042$.

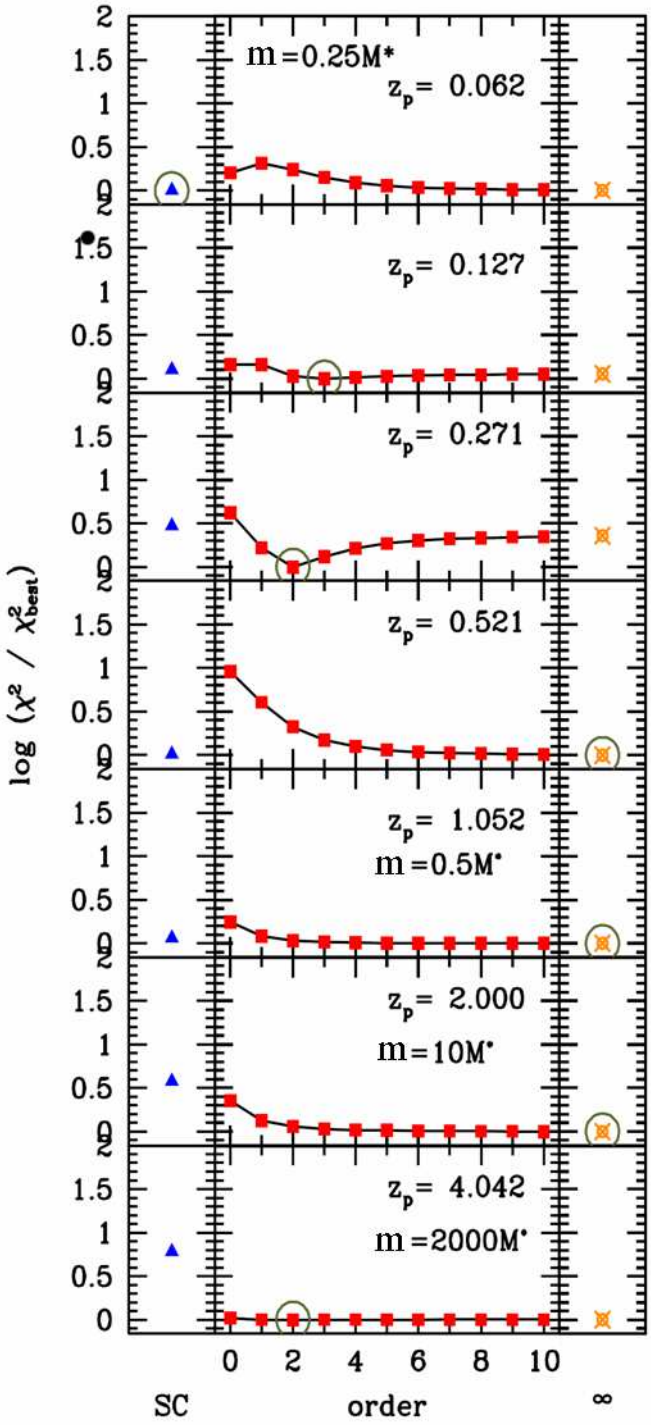

Figure 5.20: χ^2 for 7 halo redshifts of halo of mass (from top to bottom) $m = 0.25M^*$ at $z = 0.062$, 0.127, 0.271, 0.521, $m = 0.5M^*$ at $z = 1.052$, $m = 10M^*$ at $z = 2.000$, $M = 2000M^*$ at $z = 4.042$ and descendant at $z = 0$. Blue triangles refer to (SC / best-χ^2); red squares to (EC (orders from 0 to 10) / best-χ^2); orange crossed dots to (EC all orders / best-χ^2). The green circles show the best χ^2s.

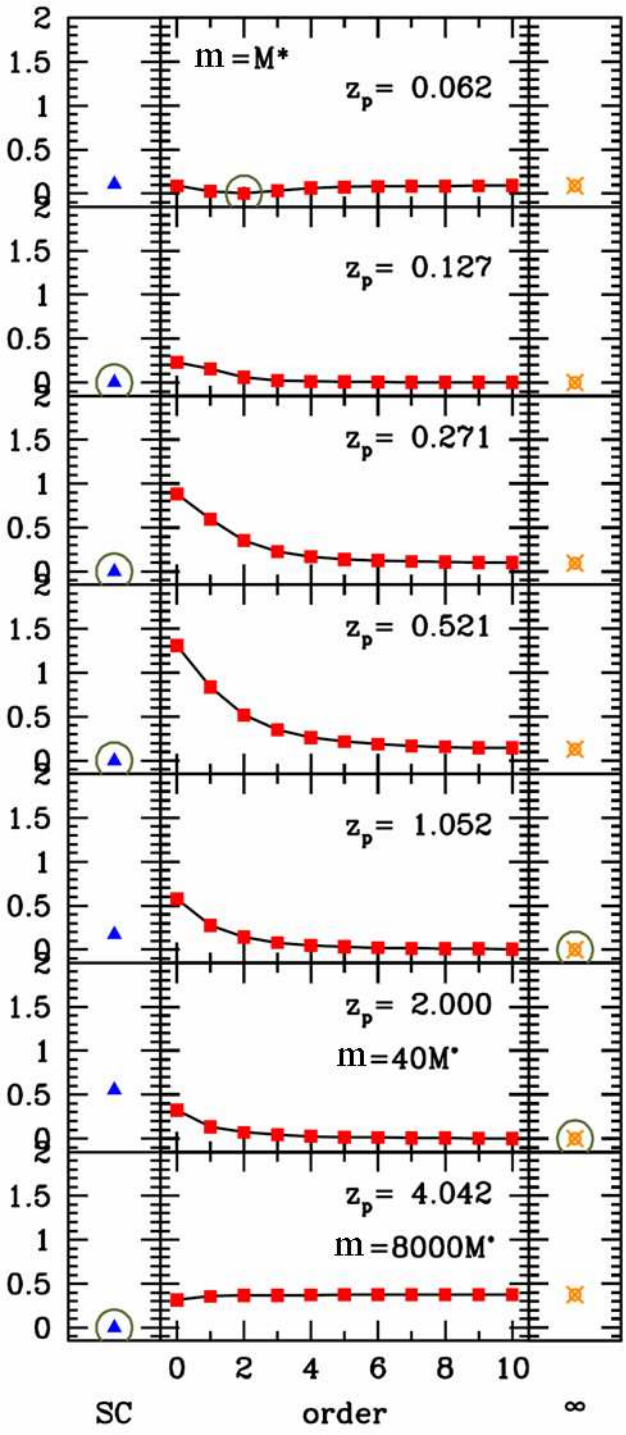

Figure 5.21: The same as 5.20, but with this halo-masses: $m = M^*$ at $z = 0.062$, 0.127, 0.271, 0.521, 1.05, $m = 40M^*$ at $z = 2.000$, $m = 8000M^*$ at $z = 4.042$.

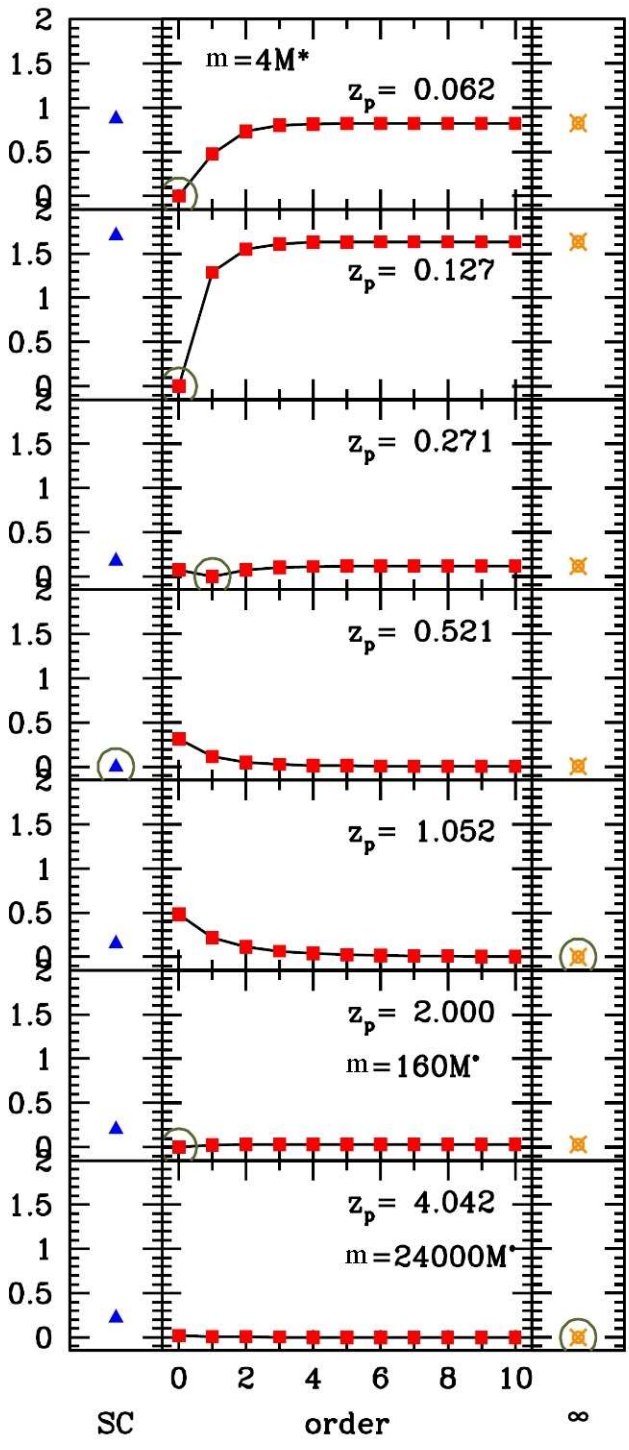

Figure 5.22: The same as 5.20, but with this halo-masses: $m = 4M^*$ at $z = 0.062$, 0.127, 0.271, 0.521, 1.05, $m = 160M^*$ at $z = 2.000$, $m = 24000M^*$ at $z = 4.042$.

5.4.1 Effect of finite box size on the descendant mass function

A look at the plots of the unconditional mass function, Figures 5.2 and 5.3, allows to understand how the finite size of the box, considered in running the simulations, can introduce a bias in the distribution. In fact, for the smaller GIF2 simulation, one can see that there exist some points, for masses greater than $\sim 10^{15} M_{\odot}$ that differ from the model of about one order of magnitude. This is due to the fact that the realizations of the Fourier modes for the power spectrum in the simulation have a robust statistics for scales smaller than the dimension of the box, but they are affected by big errors for scale ∼box scale (en example is shown in Figure 5.23).

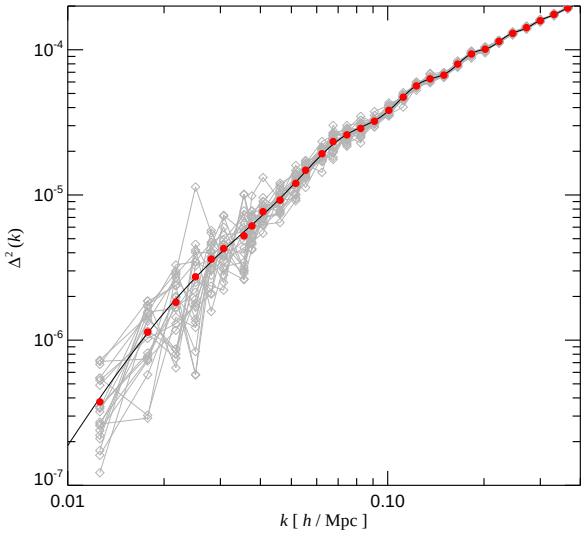

Figure 5.23: A realization of the initial power spectrum. One can see that for small k -bigger scales- there is a higher scatter of different realizations (grey lines) respect to the mean value (black line). From [77].

In this case there is an overprediction of the haloes of mass greater than $\sim 10^{15} M_{\odot}$ at $z = 0$. This can lead to overpredict also the descendant mass function, when the descendant are counted at present time. For this reason, we decide to calculate the descendant distribution only for haloes that are the progenitors of structure having $m <\sim 10^{15} M_{\odot}$. Figure 5.24 shows how the descendant mass function can be affected by this bias: for the GIF2 simulation (black dots) there is a plateau for the high mass tail that overpredicts the fraction of progenitor by an order of magnitude respect to both the spherical and ellipsoidal theoretical curve; this trend does not appear for the bigger Millennium simulation (red triangles).

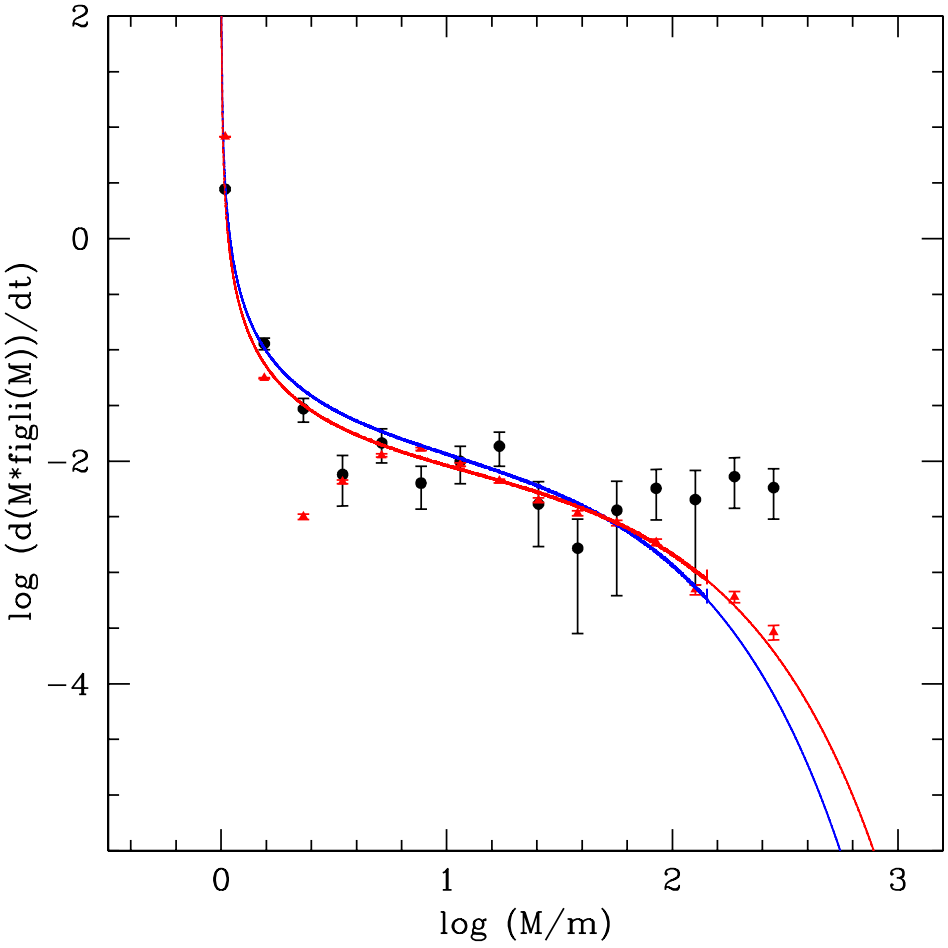

Figure 5.24: Descendant mass function for haloes with mass $m = M*$ at $z \sim 0.06$ and descendant at $z = 0$. Red and blue lines are ellipsoidal and spherical theoretical prediction. Black dots are the GIF2 data and red triangles are the Millennium data. The GIF2 overpredicts the number of descendants in the high mass range.

5.5 Merger Rates

The only way to extract the distribution of merger rates (instantaneous rates of destruction) in a numerical simulation is to build the descendant mass function considering two contiguous snapshots, and divide the result by the difference in cosmic time from one redshift to another. In this case we use both the GIF2 and the Millennium Simulation because we have informations about the descendants "at the next step" also for the bigger simulation. This comparison seems to be usefull because, when considering contiguous snapshots, the descendant mass function in GIF2 seems much noisy. We compare four analytical equations:
(i) the merger rate for the Spherical Collapse, eq. (3.31);
(ii) the merger rate for the Ellipsoidal Collapse eq. (4.23);
(iii) the spherical descendant mass function eq. (3.27), devided by the Δt coming from the relative snapshots of the simulation;
(iv) the ellipsoidal descendant mass function eq. (4.22), with $T(S) = T_\infty(S)$ (all the series) for the unconditional mass function and the whole $T(S_1|S_2)$ for the progenitor mass function, divided by the Δt coming from the relative snapshots of the simulation. For $\Delta z \to 0$, equation (iii) approaches (i), and (iv) approaches (ii). Figure 5.25 shows the differences between the two pairs of curves for three different Δz: increasing the redshift-difference between the halo-snapshot and the descendant-snapshot, the difference between the two pair of equations grows.

In this case, we consider the equations with their "original" normalizations, and we compare them with the distribution of descendants for haloes in three different mass intervals for each redshift. In Table 5.5 there are the values of the redshift of the considered haloes and the associated redshifts of the descendants "at the next snapshot" of the two simulations. The mass intervals are the same as for the descendant mass

GIF2	Millennium
$0.062 \to 0.000$	$0.064 \to 0.041$
$0.127 \to 0.062$	$0.116 \to 0.089$
$0.271 \to 0.197$	$0.279 \to 0.242$
$0.521 \to 0.433$	$0.508 \to 0.456$
$1.052 \to 0.933$	$0.989 \to 0.905$
$2.000 \to 1.940$	$2.070 \to 1.913$
$4.042 \to 3.748$	$4.179 \to 3.866$

Table 5.4: For the GIF2 and the Millennium simulations, the values of the redshifts at which we consider the haloes and the values of the following redshift at which we look for the descendants.

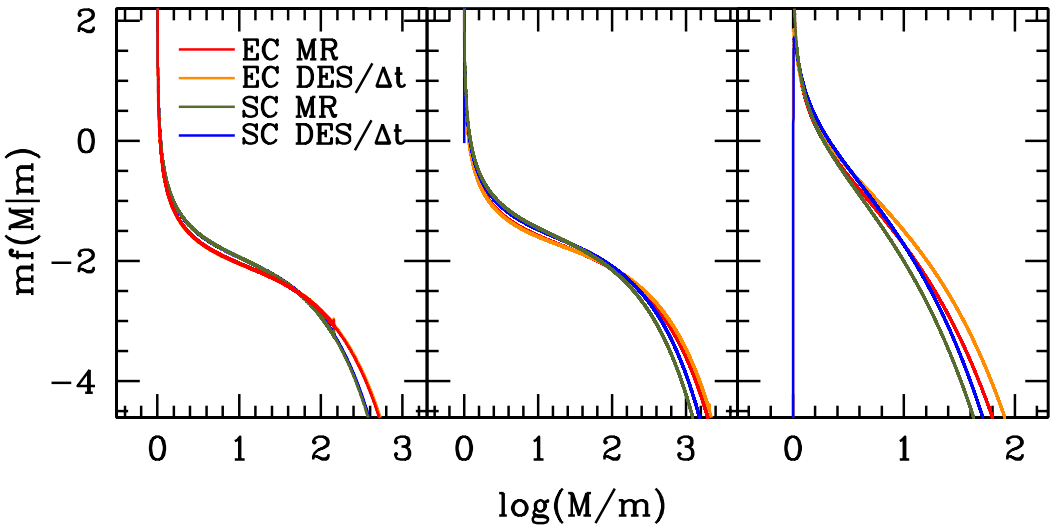

Figure 5.25: Comparison between the merger rate (spherical=green, ellipsoidal=red) and the "descendant mass function / Δt" (spherical=blu, ellipsoidal=orange), for different values of Δz: in the left panel $\Delta z = 0.062$; in the central panel $\Delta z = 0.119$; in the right panel $\Delta z = 0.294$.

function (see Section 5.4).

In Figure 5.5, 5.5, 5.5, we show the results for the three intervals of halo-masses. Taking into account the relation between the merger rates and the equation of "descendants over Δt", we plot only these second type of curves. Moreover, since the curves obtained using the parameters (halo mass, halo-redshift, descendant-redshift) resulting from the GIF2 simulation degenerate over the curves plotted using the Millennium parameters, we show the results only for one of the two sets. The blue curves represent

the spherical collapse model, and the orange ones, the ellipsoidal results; the black dots are the GIF2-data and the red triangles are the results of Millennium: the data from simulations have poissonian error bars.

For the merger rates we don't perform a deep statistical analysis, since the GIF2 simulation shows a big noise especially at high redshifts, and the Millennium have a "bump" that under-predicts the number of descendants for $\log(M/m) =\sim 0.4 \div \sim 0.8$: with these circumstaces, a χ^2 analysis would be useless. So, we consider the distributions from a qualitatively point of view, and we can assert that the ellipsoidal collapse provides the best approximation for the merger rates, except for the regimes where we do not have enough data (high redshifts).

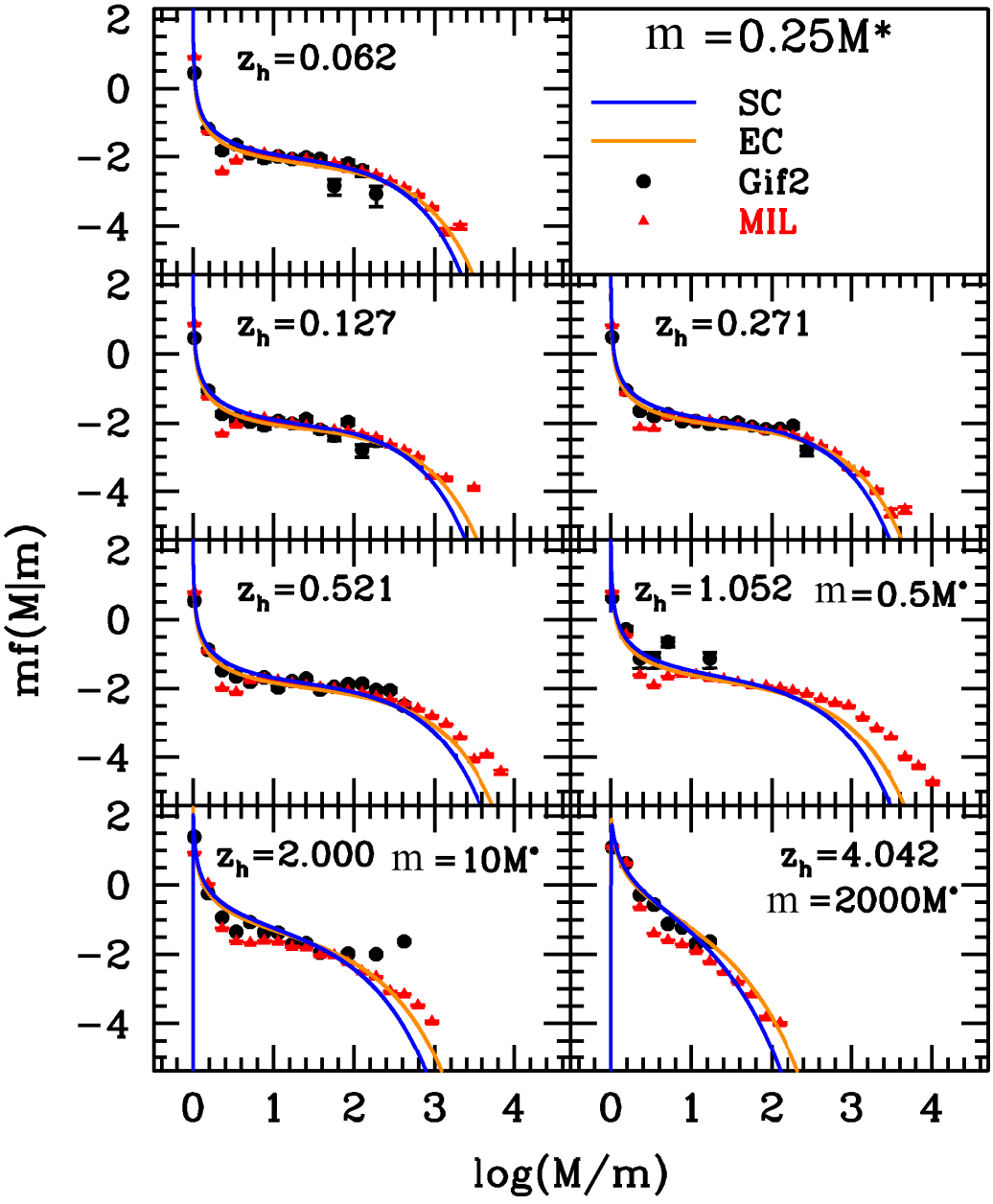

Figure 5.26: Blue and orange curves: merger rate from the spherical and ellipsoidal model respectively; black dots and red triangles: results from GIF2 and Millennium simulations respectively, with poissonian error bars. The haloes are kept at various redshift, and the descendants found at the next snapshots, see Table 5.5. The haloes have are chosen in the mass interval $m = [0.125M^*, 0.5M^*]$, except for $z = 1.052$ ($m = [0.25M^*, M^*]$), for $z = 2.000$ ($m = [5M^*, 20M^*]$), and for $z = 4.042$ ($m = [1000M^*, 4000M^*]$).

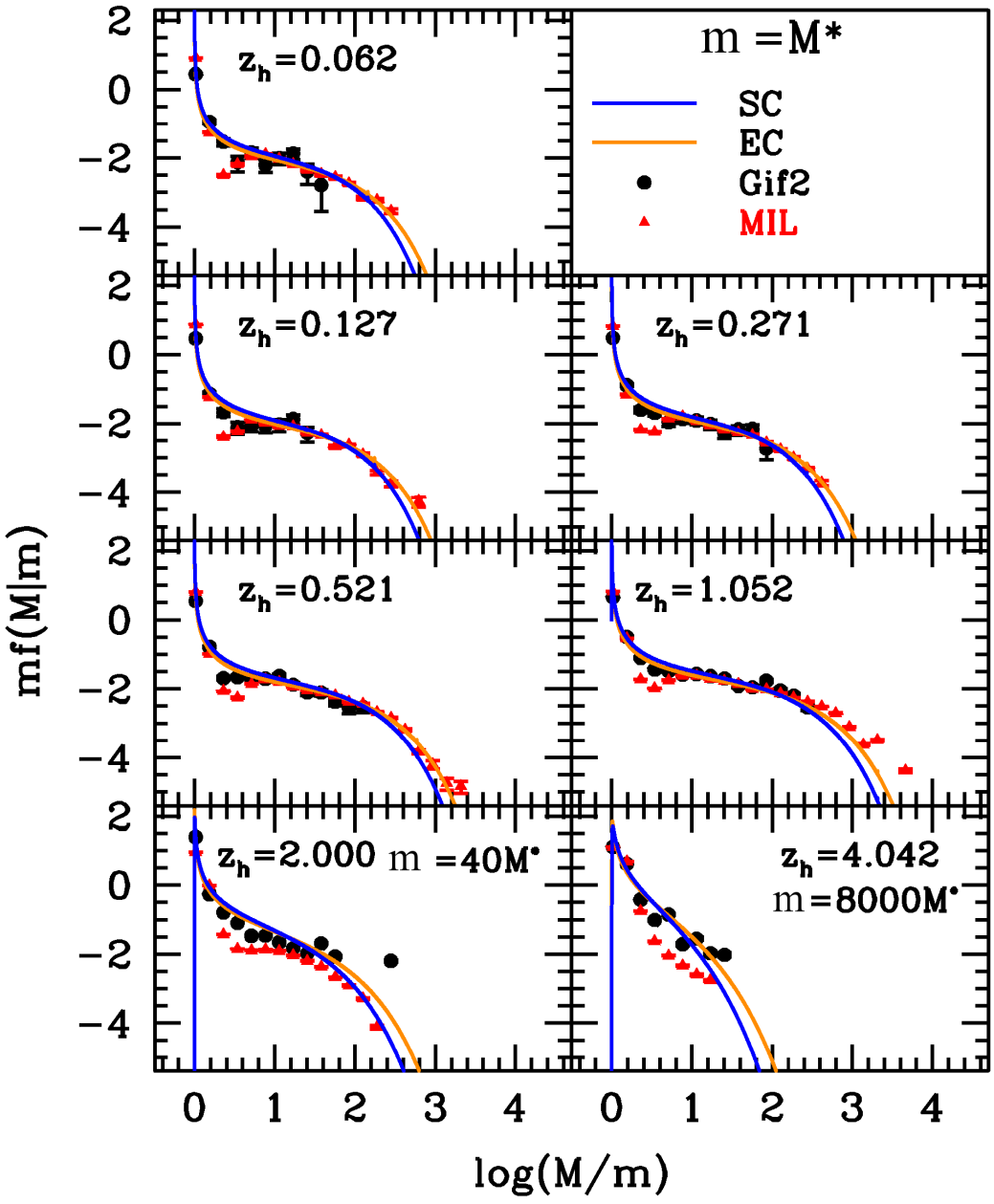

Figure 5.27: The same as fig 5.5, but with halo mass in these intervals: $m = [0.5M^*, 2M^*]$ for $z = 0.062$, $z = 0.127$, $z = 0.271$, $z = 0.521$, $z = 1.052$, $m = [20M^*, 80M^*]$ for $z = 2.0002$, $m = [4000M^*, 16000M^*]$ for $z = 4.042$.

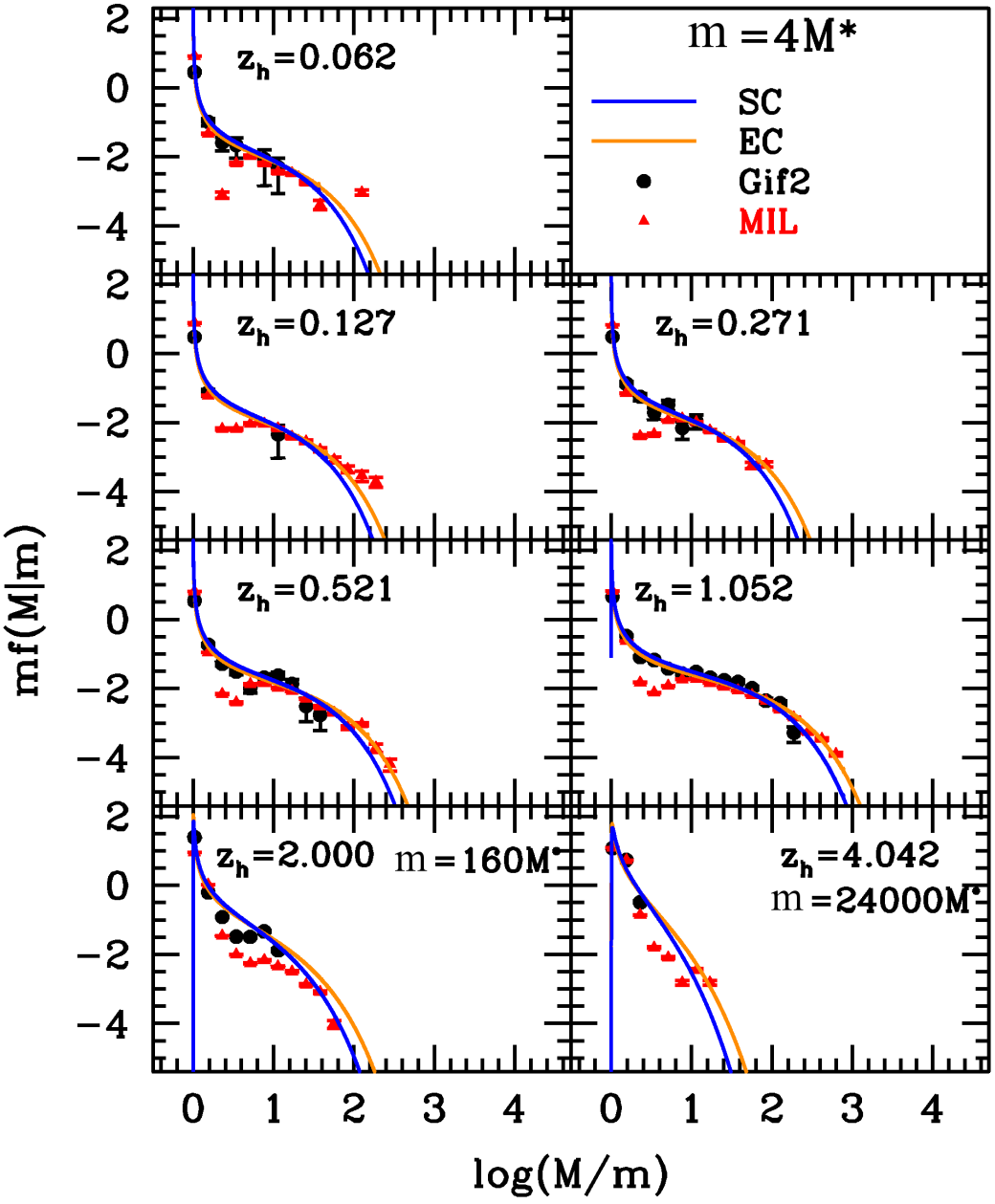

Figure 5.28: The same as fig 5.5, but with halo mass in these intervals: $m = [2M^*, 8M^*]$ for $z = 0.062$, $z = 0.127$, $z = 0.271$, $z = 0.521$, $z = 1.052$, $m = [80M^*, 320M^*]$ for $z = 2.0002$, $m = [12000M^*, 48000M^*]$ for $z = 4.042$.

Chapter 6

Maximum likelihood based new method

The χ^2-method, used to check how accurate are our equations, shows some limits in its application. One problem is linked with the creation of mass- (or ν-) bins, in which the information about a certain number of haloes in a simulation is grouped together providing only a mean information for each bin that depends on the size of the bin itself: this can lead to slightly different results in the determination of the best model. The second problem concerns with the presence, in a simulation, of particles that are not bound in haloes, that we call dust particle: in the previous analysis, we consider the presence of these particles, but only in order to normalize the theoretical curves considering all the matter in the simulation; so the dust particles did not contribute to the determination of the best model. To improve the statistics and the precision of the results, we introduce a method based on the maximum likelihood analysis that takes into account unbinned data and considers also the dust particles in the discrimination of the best curve.

The maximum likelohood method is based on the construction of a probability distribution (likelihood function) parameterized by a set of unknown parameters $\vec{\theta}$, associated with a known probability mass function, denoted as $f_{\vec{\theta}}$. With a sample x_1,x_2,...,x_n of n values from this distribution, one can compute the probability density associated with the observed data, $f_{\vec{\theta}}(x_1, \ldots, x_n)$. The likelihood function, with x_1, ..., x_n fixed and as a function of $\vec{\theta}$ is:

$$\mathcal{L}(\vec{\theta}) = f_{\vec{\theta}}(x_1, \ldots, x_n). \tag{6.1}$$

The method estimates $\vec{\theta}$ by finding the value of $\vec{\theta}$ that maximizes $\mathcal{L}(\vec{\theta})$. This is the maximum likelihood estimator of $\vec{\theta}$:

$$\widehat{\vec{\theta}} = \arg\max \mathcal{L}(\vec{\theta}). \tag{6.2}$$

If the data drawn from a particular distribution are independent, identically distributed with unknown parameters, the likelihood can then be written as a product of n univariate probability densities:

$$\mathcal{L}(\vec{\theta}) = \prod_{i=1}^{n} f_{\vec{\theta}}(x_i); \tag{6.3}$$

one can take the logarithm of this expression to turn it into a sum:

$$\log\mathcal{L}(\vec{\theta}) = \sum_{i=1}^{n} \log f_{\vec{\theta}}(x_i). \tag{6.4}$$

6.1 Statistics on the Mass Function

As probability distribution, we consider the unconditional mass function. The probability for all the particles to be in haloes of a certain mass m is:

$$\prod_{i=1}^{N_{part}} f(m_i|\vec{\theta}) \tag{6.5}$$

where N_{part} is the total number of particles. If the i-halo contains N_i particles, we can write:

$$\prod_{i=1}^{N_h} f(m_i|\vec{\theta})^{N_i} \tag{6.6}$$

where N_h is the total number of haloes. The probability for a particle in the dust is:

$$F(\vec{\theta}) = \int_0^{M_{dust}} f(m)\mathrm{d}m \tag{6.7}$$

so the probability for all particles is obtained by raising the integral to the N_d, the total number of dust particles. So, the logarithm of the likelihood function is:

$$\ln\mathcal{L} = N_d \ln F(\vec{\theta}) + \sum_{i=1}^{N_h} N_i \ln f_i(\vec{\theta}). \tag{6.8}$$

Using this method we can go beyond the two problems coming from the previous analysis: the binning disappears and each particle has the same weight in the determination of the best parameter for the mass function; besides, also the dust particles (considered together) matter to this determination, because their integral appears in the likelihood function.

We choose to use the mass function by Sheth & Tormen (1999) [69] that contains 2 parameters: a and p, (while ν is the 'observed' quantity that comes from the simulations):

$$\nu f(\nu|a,p) = A\sqrt{\frac{a}{2\pi\nu}}\exp\left[-\frac{a\nu}{2}\right](1+(a\nu)^{-p}) \tag{6.9}$$

In this case the likelihood function becomes:

$$\begin{aligned}\ln\mathcal{L} &= N_d \ln\left(\frac{A}{\sqrt{\pi}}\int_0^{\frac{a\nu_d}{2}} x^{-0.5}\exp(-x)\left(1+\frac{1}{(2x)^p}\right)\mathrm{d}x\right) + \\ &+ \sum_{i=1}^{N_p}\ln\left(A\sqrt{\frac{a}{2\pi\nu_i}}\exp\left(-\frac{a\nu_i}{2}\right)\left(1+(a\nu_i)^{-p}\right)\right)\end{aligned} \tag{6.10}$$

To find the parameters a and p that maximize the likelihood function, we need the expressions for the derivative respect to a and respect to p:

$$\begin{aligned}\frac{\partial\ln\mathcal{L}}{\partial a} &= \frac{1}{a}\left\{\left[N_d\frac{\sqrt{\frac{a\nu_d}{2}}\exp(-\frac{a\nu_d}{2})(1+(a\nu_d)^{-p})}{\gamma\left(\frac{1}{2},\frac{a\nu_d}{2}\right)+\frac{1}{2^p}\gamma\left(\frac{1}{2}-p,\frac{a\nu_d}{2}\right)}\right] + \right. \\ &+ \left.\sum_{i=1}^{N_p}\left(\frac{1}{2}-\frac{a\nu_i}{2}-\frac{p}{(a\nu_i)^p+1}\right)\right\}\end{aligned} \tag{6.11}$$

$$\begin{aligned}\frac{\partial\ln\mathcal{L}}{\partial p} &= N_d\left(\frac{\ln 2+\digamma(\frac{1}{2}-p)}{\frac{2^p\Gamma(\frac{1}{2})}{\Gamma(\frac{1}{2}-p)}+1}+\frac{\partial_p\ln\gamma\left(\frac{1}{2}-p,\frac{a\nu_d}{2}\right)-\ln 2}{\frac{2^p\gamma(\frac{1}{2},\frac{a\nu_d}{2})}{\gamma(\frac{1}{2}-p,\frac{a\nu_d}{2})}+1}\right)+ \\ &+ \sum_{i=1}^{N_p}\left(\frac{\ln 2+\digamma(\frac{1}{2}-p)}{\frac{2^p\Gamma(\frac{1}{2})}{\Gamma(\frac{1}{2}-p)}+1}-\frac{\ln(a\nu_i)}{(a\nu_i)^p+1}\right)\end{aligned} \tag{6.12}$$

where $\Gamma(z)$ is the Gamma function[1], $\gamma(s,x)$ is the lower incomplete gamma function[2] and $\digamma$ is the digamma function.[3]

In order to check if the method works, we consider a Monte Carlo simulation of the mass function, following the way described by Kundu & Gupta (2006) [40] to generate gamma random variables using generalized exponential distributions and a routine of the software supermongo to generate a gaussian distribution; in these simulations we fix the parameters $a=1$ and $p=0.3$ (Fig. 6.1).

Solving the equations $\frac{\partial\ln\mathcal{L}}{\partial a}=0$ and $\frac{\partial\ln\mathcal{L}}{\partial p}=0$ (i.e. looking for the maximum), we can find the best parameters that describe the analytical equation of the mass function.

[1] $\Gamma(z) = \int_0^\infty t^{z-1}\exp^{-t}\mathrm{d}t$
[2] $\gamma(s,x) = \int_0^x t^{s-1}\exp^{-t}\mathrm{d}t$
[3] $\digamma(z) = \frac{\mathrm{d}}{\mathrm{d}z}\ln\Gamma(z) = \frac{\Gamma'(z)}{\Gamma(z)}$

The errors associated to the best values of the parameters are obtained using the Fisher information matrix:

$$\left(\mathcal{I}\left(\theta\right)\right)_{i,j} = -\left[\frac{\partial^2}{\partial\theta_i\partial\theta_j}\ln f(X;\theta)\middle|\,\theta\right] \tag{6.13}$$

evaluated in $\widehat{\vec{\theta}}$: it is the of the probability surface in the parameter space calculated in the point defined by $\widehat{\vec{\theta}}$. To apply the Fisher matrix we need the expressions of the second derivatives of the likelihood function; we obtain:

$$\begin{aligned}\frac{\partial^2\ln\mathcal{L}}{\partial a^2} &= \frac{1}{a^2}\Bigg\{N_d\sqrt{\frac{a\nu_d}{2}}\exp\left(-\frac{a\nu_d}{2}\right)\left(1+(a\nu_d)^{-p}\right)\times \\ &\times \frac{\frac{1}{2}-\frac{a\nu_d}{2}-\frac{p}{(a\nu_d)^p+1}-\sqrt{\frac{a\nu_d}{2}}\exp\left(-\frac{a\nu_d}{2}\right)\left(1+(a\nu_d)^{-p}\right)}{\gamma\left(\frac{1}{2},\frac{a\nu_d}{2}\right)+\frac{\gamma\left(\frac{1}{2}-p,\frac{a\nu_d}{2}\right)}{2^p}}+ \\ &+ \sum_{i=1}^{N_p}\left(\frac{p^2(a\nu_i)^p}{((a\nu_i)^p+1)^2}-0.5\right)\Bigg\}\end{aligned} \tag{6.14}$$

$$\begin{aligned}\frac{\partial^2\ln\mathcal{L}}{\partial p^2} &= \\ &= N_d\Bigg[\frac{\partial_p\Gamma\left(\frac{1}{2}-p\right)}{\frac{2^p\Gamma\left(\frac{1}{2}\right)}{\Gamma\left(\frac{1}{2}-p\right)}+1}-\frac{\left[\ln 2+\Gamma\left(\frac{1}{2}-p\right)\right]^2}{\left[\frac{2^p\Gamma\left(\frac{1}{2}\right)}{\Gamma\left(\frac{1}{2}-p\right)}+1\right]^2\frac{\Gamma\left(\frac{1}{2}-p\right)}{2^p\Gamma\left(\frac{1}{2}\right)}}+\frac{\partial^2\ln\gamma\left(\frac{1}{2}-p,\frac{a\nu_d}{2}\right)}{\frac{2^p\gamma\left(\frac{1}{2},\frac{a\nu_d}{2}\right)}{\gamma\left(\frac{1}{2}-p,\frac{a\nu_d}{2}\right)}+1}+ \\ &+ \frac{\left[\ln 2-\partial\ln\gamma\left(\frac{1}{2}-p,\frac{a\nu_d}{2}\right)\right]^2}{\left[\frac{2^p\gamma\left(\frac{1}{2},\frac{a\nu_d}{2}\right)}{\gamma\left(\frac{1}{2}-p,\frac{a\nu_d}{2}\right)}+1\right]^2\frac{\gamma\left(\frac{1}{2}-p,\frac{a\nu_d}{2}\right)}{2^p\gamma\left(\frac{1}{2},\frac{a\nu_d}{2}\right)}}\Bigg]+ \\ &+ \sum_{i=1}^{N_p}\left(\frac{\partial_p\Gamma\left(\frac{1}{2}-p\right)}{\frac{2^p\Gamma\left(\frac{1}{2}\right)}{\Gamma\left(\frac{1}{2}-p\right)}+1}-\frac{\left[\ln 2+\Gamma\left(\frac{1}{2}-p\right)\right]^2}{\left[\frac{2^p\Gamma\left(\frac{1}{2}\right)}{\Gamma\left(\frac{1}{2}-p\right)}+1\right]^2\frac{\Gamma\left(\frac{1}{2}-p\right)}{2^p\Gamma\left(\frac{1}{2}\right)}}+\frac{\left[\ln(a\nu_i)\right]^2(a\nu_i)^2}{\left[(a\nu_i)^p+1\right]^2}\right)\end{aligned} \tag{6.15}$$

$$\begin{aligned}\frac{\partial^2\ln\mathcal{L}}{\partial a\partial p} &= \\ &= \frac{1}{a}\Bigg\{N_d\Bigg(\frac{\left(\frac{a\nu_d}{2}\right)^{\frac{1}{2}-p}\exp\left(-\frac{a\nu_d}{2}\right)\left[-\ln\left(\frac{a\nu_d}{2}\right)-\ln 2\right]}{2^p\gamma\left(\frac{1}{2},\frac{a\nu_d}{2}\right)+\gamma\left(\frac{1}{2}-p,\frac{a\nu_d}{2}\right)}+ \\ &- \frac{\gamma\left(\frac{1}{2}-p,\frac{a\nu_d}{2}\right)\left[\partial_p\ln\gamma\left(\frac{1}{2}-p,\frac{a\nu_d}{2}\right)-\ln 2\right]\left[\left(\frac{a\nu_d}{2}\right)^{\frac{1}{2}}2^p+\left(\frac{a\nu_d}{2}\right)^{\frac{1}{2}-p}\right]\exp\left(-\frac{a\nu_d}{2}\right)}{\left[2^p\gamma\left(\frac{1}{2},\frac{a\nu_d}{2}\right)+\gamma\left(\frac{1}{2}-p,\frac{a\nu_d}{2}\right)\right]^2}\Bigg)+ \\ &+ \sum_{i=1}^{N_p}\left(\frac{p\ln(a\nu_i)(a\nu_i)^p}{\left[(a\nu_i)^p+1\right]^2}-\frac{1}{(a\nu_i)^p+1}\right)\Bigg\}\end{aligned} \tag{6.16}$$

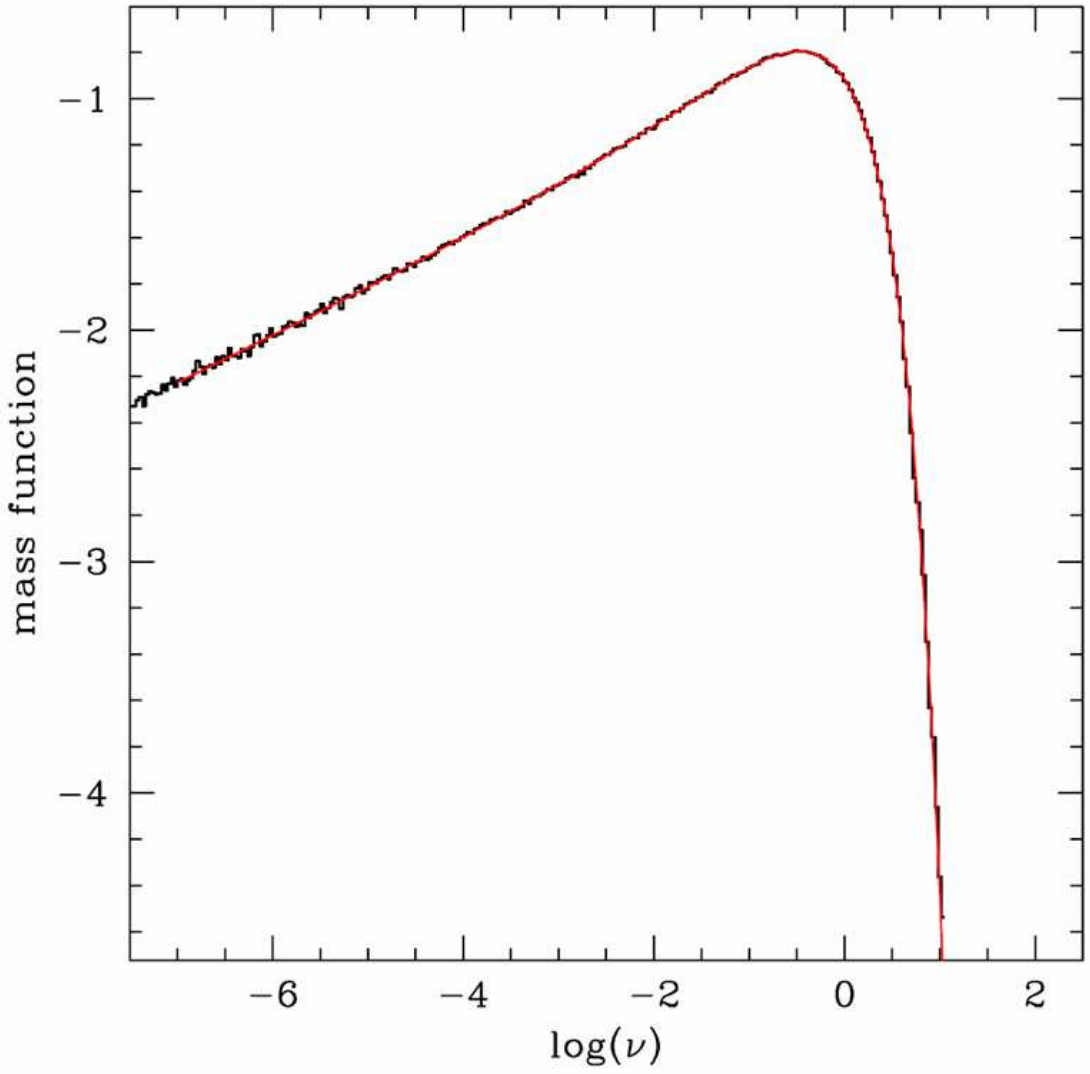

Figure 6.1: The analytical mass function -red line- is compared with the results of a Monte Carlo simulation -black histograms-, run following Kundu & Gupta (2006) [40].

6.2 Results of the test

In Figures 6.2, 6.3, 6.4, we show the results of the best parameters a and p found with our algorithm, that describe the results of a number of Monte Carlo simulations, run assuming $a_{input} = 1$ and $p_{input} = 0.3$, and three different values of the dust threshold: $\nu_d = 0.1$, 1.0, 2.0. In the plot the red line is the locus of points where the derivative respect to p is equal to zero (within a certain error due to numerical approximations of some equations); the blu line represents the locus of points where the derivative respect to a is equal to zero; we consider the intersection of this two lines as the maximum

likelihood point that describes the components of the vector of the best parameters: this point corresponds also to the center of the 'higher contour' of the function log$\mathcal{L}$ (not shown in the plot). Besides, there are the error bars associated to the two parameters and their values as well as the number of particles in the simulation.

From the three plots, one can see that the analytical equations and the routine used to obtain the best values for the parameters a and p, starting from the results of different Monte Carlo realization of the mass function, work. The a and p found are in agreement with the input values, within the error bars.

This is only a preliminary test, the first that has to be run before applying the method to a numerical simulation.

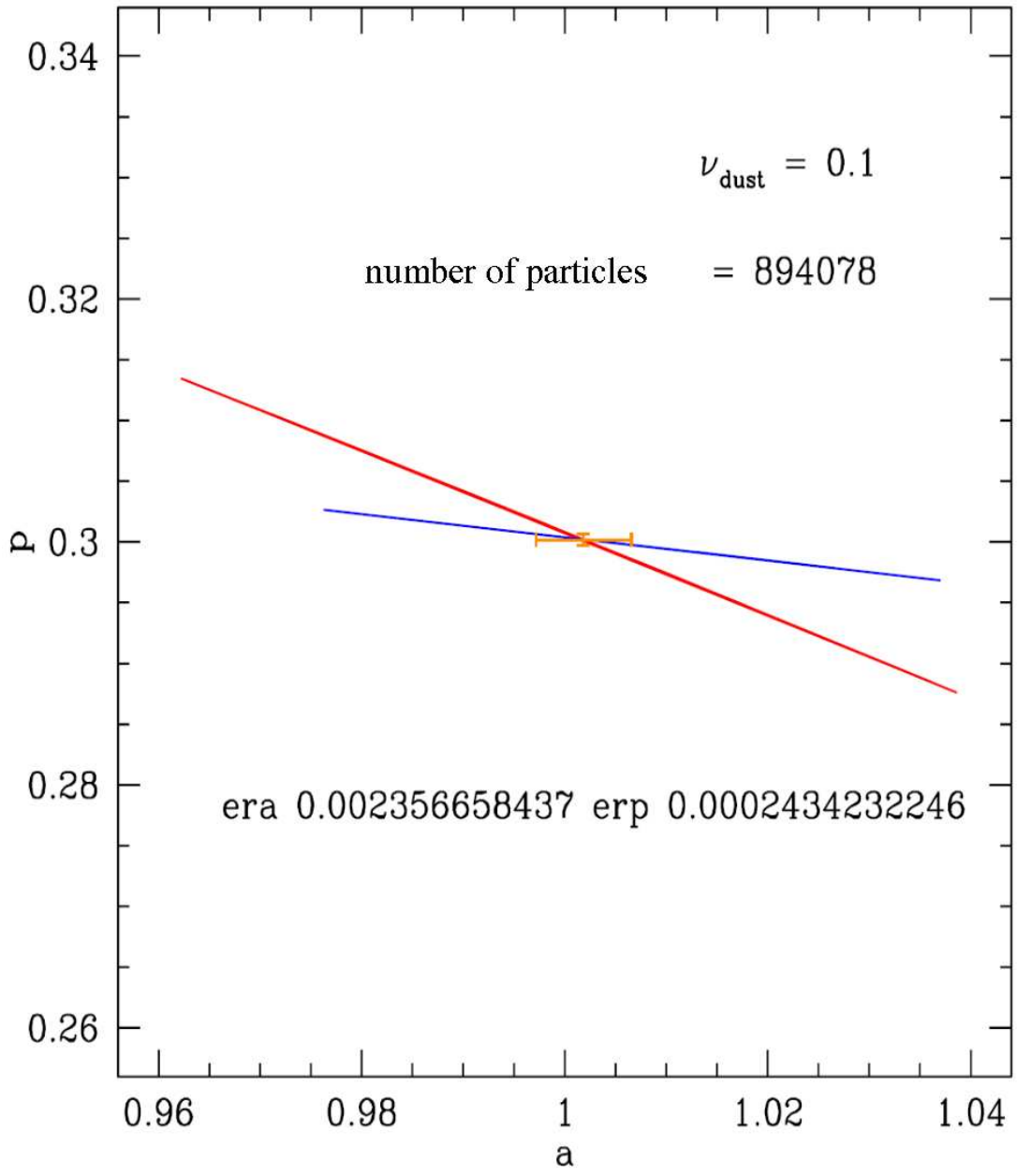

Figure 6.2: The best value of the parameters a and p are the coordinates of the intersection between the red and the blue lines. The red line represents the solution of $\frac{\partial \mathcal{L}}{\partial p} = 0$; the blue line represents the solution of $\frac{\partial \mathcal{L}}{\partial a} = 0$; in orange, there are the associated error bars. This is the result found assuming $\nu_{dust} = 0.1$.

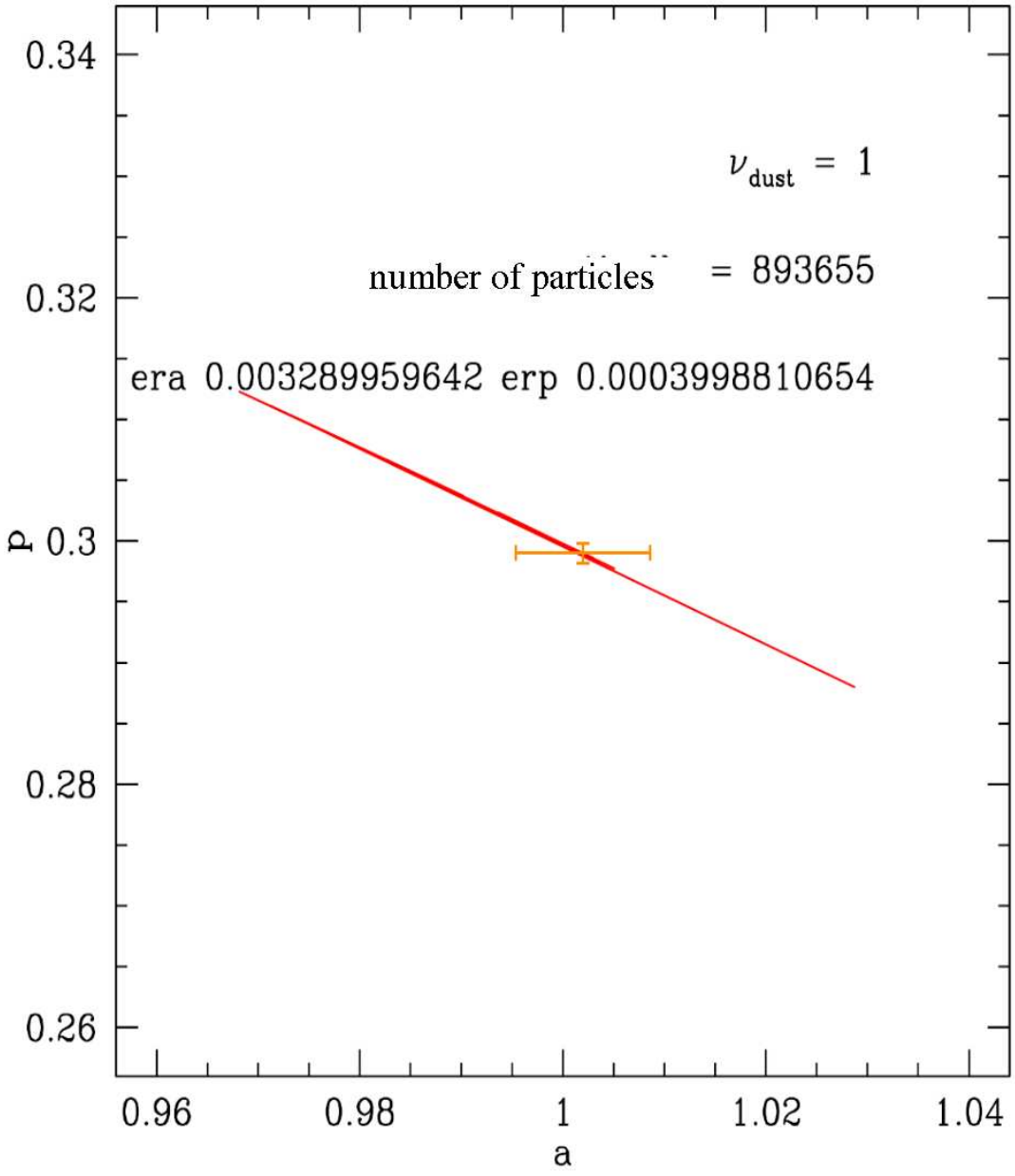

Figure 6.3: The same as Fig. 6.2, but assuming $\nu_{dust} = 1$.

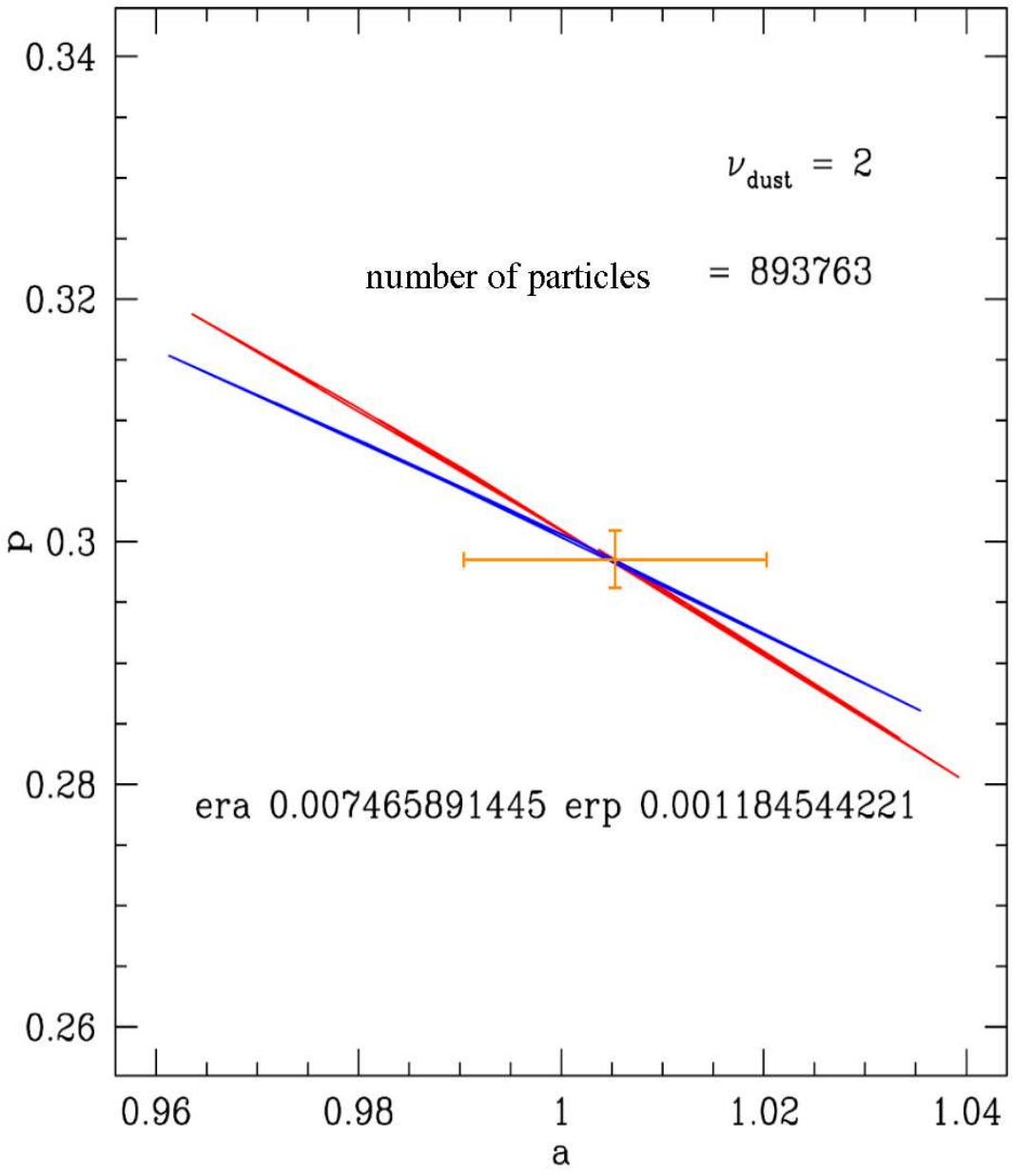

Figure 6.4: The same as Fig. 6.2, but assuming $\nu_{dust} = 2$.

Conclusions

In this dissertation, after an introduction on the best models describing the homogeneous and isotropic universe and the formation of cosmic structures, we consider the differences between the main two paradigms that trace the dynamics of the formation of the dark matter haloes: the spherical and the ellipsoidal model, and we highlight the better accuracy of the second one in reproducing the results of numerical simulations. Since in the literature there is a complete picture of the distributions of dark matter haloes only in the spherical context, we face the demand of having analytical equations also for the more precise ellipsoidal collapse, and we briefly show how useful can be such new distributions to better understand the behaviour both of the dark and baryonic matter when they organize into cosmic strutures.

The first goal of our work is to find new analytical equations for a number of distributions, staying within the context outlined by the ellipsoidal dynamics, and using as a tool the excursion sets formalism. We find forms for the global mass function, for the progenitor and descendant mass functions, and for the instantaneous rate of creation and destruction.

Since the analytical part of the work is based on the use of a Taylor expansion series, for each distribution we have a number of equations, depending on the order of this expansion. In order to choose the best formulas, we exploit the results of the GIF2 and of the Millennium simulations; models and data are compared using a χ^2 technique. The results about the best model are not unique, varying the redshifts or the mass range, but there is a tendency toward the ellipsoidal model to be the best one. Within the various choices provided by stopping the series at different orders, we found that the use of the whole Taylor expansion series, when it is not the best formula, it is affected by a very small error compared to the most accurate distribution. This is an important result, since the equations with ∞ terms in their expansion series are the most analytically simple.

In the last part of the dissertation we try to solve two inconvenients that come from the χ^2 method: in the process of the binning of the data, the amplitude of the bin can bias the results of the test; moreover, the approach do not allow to use the particle that

are not bound in haloes (dust) in the determination of the best model. To overcome these two problems, we consider a new statistical method based on the maximum likelihood technique, that allows both to consider unbinned data and to include the dust particles in the determination of the best parameters of the mass function. Starting from a two parameters mass function, we provide all the analytical equations necessary to determine the best parameters and the associated errors. We first run a test simulating a mass function with a Monte Carlo method: for different choices of the threshold for the value of the dust-mass, the results of our routine for the two parameters are in agreement with the input parameter, within the error bars.

The natural continuation of this work is the comparison of other analytical quantities (e.g. the instantaneous rates of creation, and the integrated rate of creation and destruction) with the results of numerical simulation. Then, in order to apply a more robust an accurate statistics to the data, it is necessary to conclude the tests on the new maximum likelihood method, e.g. the dependence of the results on the number of particles, or on the number of parameters. Moreover we need to performe the relative equations also for other distributions.

Appendix

Numerical Cosmology

In Section 2.3.3 the basic equations that describe the structures formation and evolution in the gravitational instability scenario were introduced. The substantial difficulty of this problem is exacerbated by the inherent three-dimensional character of structure formation in a ΛCDM universe, where, due to the shape of the primordial power spectrum, a large range of wave modes becomes nonlinear in a very short time, resulting in the rapid formation of objects with a wide range of masses which merge in geometrically complex ways into ever more massive systems. This complexity of the physical behaviour of the fluctuations makes the analytical models unsuitable for a detailed description of non-linear regime. Therefore, direct numerical simulations of structure formation provide the only method for studying this problem in its full generality.

Gravitational force description: N-body simulations

It is possible to represent part of the expanding Universe as a 'box' containing a large number N of point masses interacting through their mutual gravity. This box, typically a cube, must be at least as large as the scale at which the Universe becomes homogeneous if it is to provide a 'fair sample' which is representative of the Universe as a whole. It is common practice to take the cube as having periodic boundary conditions in all directions, which also assists in some of the computational techniques by allowing Fourier methods to be employed in summing the N-body forces. A number of numerical techniques are available at the present time; they differ, for the most part, only in the way the forces on each particle are calculated. We describe some of the most popular methods here:

Direct summation

The simplest way to compute the non-linear evolution of a cosmological fluid is to represent it as a discrete set of particles, and then sum the (pairwise) interactions between them directly to calculate the Newtonian forces. Such calculations are often called particle-particle, or PP, calculations. With the adoption of a small timestep, one can use the resulting acceleration to update the particle velocity and then its position. New positions can then be used to recalculate the interparticle forces, and so on. However, there is a numerical problem with summation of the forces: the Newtonian gravitational force between two particles increases as the particles approach each other and it is therefore necessary to choose an extremely small timestep to resolve the large

velocity changes this induces. A very small timestep would require the consumption of enormous amounts of CPU time and, in any case, computers cannot handle the formally divergent force terms when the particles are arbitrarly close to each other. One usually avoids these problems by treating each particle not as a point mass, but as an extended body. The practical upshot of this is that one modifies the Newtonian force between particles by putting

$$\mathbf{F}_{\rm ij} = \frac{Gm^2(\mathbf{x}_{\rm j} - \mathbf{x}_{\rm i})}{\left(\epsilon^2 + |\mathbf{x}_{\rm i} - \mathbf{x}_{\rm j}|^2\right)^{3/2}}, \tag{17}$$

where the particles are at positions $\mathbf{x}_{\rm i}$ and $\mathbf{x}_{\rm j}$ and they all have the same mass m; the form of this equation avoids infinite forces at zero separations. The parameter ϵ in Equation (17) is usually called the *softening length* and it acts to suppress two-body forces on small scales. This is equivalent to replacing point masses by extended bodies with a size of order ϵ. Since we are not supposed to be dealing with the behaviour of a set of point masses anyway, the introduction of a softening length is quite reasonable but it means one cannot trust the distribution of matter on scales of order ϵ or less. The crucial limitation of these methods is that they tend to be very slow, with the computational time required scaling roughly as N^2 (where N is the number of particles and $N(N-1)/2$ are the evaluations of Eq. (17) required at each timestep).

Particle-mesh techniques

The usual method for improving upon direct N-body summation for computing inter-particle forces is some form of 'particle-mesh', or PM, scheme. In this scheme the forces are solved by assigning mass points to a regular grid and then solving Poisson's equation on it. The use of a regular grid with periodic boundary conditions allow one to use Fast Fourier Transform (*FFT*) methods to recover the potential, which leads to a considerable increase in speed. Without enter in details, the calculation of the forces between particles can be speeded up by computing them in Fourier space. A FFT is basically of order $N \log N$ in the number of grid points and this represents a substantial improvement for large N over the direct particle-particle summation technique. The price to be paid for this is that the Fourier summation method implicitly requires that the simulation box has periodic boundary conditions: this is probably the most reasonable choice for simulating a 'representative' part of the Universe, so this does not seem to be too high price. The potential weakness of this method is the comparatively poor force resolution on small scales because of the finite spatial size of the mesh. A substantial increase in spatial resolution can be achieved by using instead a hybrid 'particle-particle-particle-mesh' method, which solves the short range forces directly (PP) but uses the mesh to compute those of longer range (PM); hence PP + PM =

P^3M, the usual name of such codes. Here, the short-range resolution of the algorithm is improved by adding a correction to the mesh force. This contribution is obtained by summing directly all the forces from neighbours within some fixed distance r_s of each particle. A typical choice for r_s will be around three grid units. Alternatively, one can use a modified force law on these small scales to assign particular density profile to the particles, similar to the softening procedure demonstrated in Equation (17). This part of the force may well be quite slow, so it is advantageous merely to calculate the short-range force at the start for a large number of points spaced linearly in radius and then find the actual force by simple interpolation. The long-range part of the force calculation is done by a variant of the PM method described earlier.

Tree codes

An alternative procedure for enhancing the force resolution of a particle code whilst keeping the necessary demand on computational time within reasonable limits is to adopt a hierarchical subdivision procedure. The generic name given to this kind of technique is 'tree code'. The basic idea is to treat distant clumps of particles as single massive pseudo-particles. The usual algorithm involves a mesh which is divided into cells hierarchically in such a way that every cell which contains more than one particle is divided into 2^3 sub-cells. If any of the resulting sub-cells contains more than one particle, that cell is subdivided again. There are some subtleties involved with communicating particle positions up and down the resulting 'tree', but it is basically quite straightforward to treat the distant forces using the coarsely grained distribution contained in the high level of the tree, while short-range forces use the finer grid. The greatest problem with such codes is that, although they run quite quickly in comparison with particle-mesh methods with the same resolution, they do require considerable memory resources. Their use in cosmological contexts has so far therefore been quite limited, one of the problems being the difficulty of implementing periodic boundary conditions in such algorithms.

GIF2 simulation

Gao et al. (2004) [25] performed and described the Gif2 simulation that is a cosmological simulation of a flat ΛCDM universe in a periodic cube of side $110h^{-1}$Mpc. The total number of particles considered is 400^3, with an individual mass of $m_p = 1.73 \times 10^9 M_\odot/h$. The cosmological parameters adopted are: $\Omega_m = 0.3$, $\Omega_\Lambda = 0.7$, $\sigma_8 = 0.9$ and $h = 0.7$. The initial fluctuation power spectrum index has been chosen to be $n = 1$, and the transfer function has been produced using CMBFAST (Seljak &

Zaldariaga, 1996 [66]) for $\Omega_b h^2 = 0.0196$. The initial conditions were produced by perturbing an initially uniform state represented by a 'glass' distributionof particles. The particle distribution has been generated with the method developed by White (1993) [88] which involves evolution from a Poisson distribution with the sign of Newton's constant changed when calculatinf peculiar gravitational forces. Fluctuations are imposed using the algorithm described in Efstathiou et al. (1985) [20]. Based on Zel'Dovich (1970) approximation [93], a Gaussian random field has been set up by perturbing the particle positions and by assigning them veocities according to the growing mode solution of linear theory. In order to save computational time, the simulation has been performed in two steps:

- from high redshift until $z = 2.2$ the simulation has been run with SHMEM (parallel version of HYDRA, Couchman et al. 1995 [16]). At these times the particle distributions are lightly clustered and thus the P3M-based gravity solver is quite efficent;
- from $z = 2.2$ to $z = 0$ the simulation has been completed with a tree-based parallel code, GADGET, by Springel at al. (2001) [76], which has better performance in the heavily cluster regime.

However the two codes adopt different force-softening schemes, so it is necessary to match the force shape at the time of switch from one code to the other. Experimentations showed that $\epsilon_{HYDRA} = 1.06\epsilon_{GADGET}$ produces an excellent match of the two force laws. To take into account this difference from $z = 49$ to $z = 2.2$, the simulation has been performed with a gravitational softening $\epsilon = 7$kpc/h in comoving units, while from $z = 2.2$ to $z = 0$, $\epsilon = 6.604$kpc/h using GADGET.

The numerical data for GIF2 simulation are publicy available at: *http://www.mpa-garching.mpg.de/Virgo*.

The GIF2-haloes are identified, at each snapshot, using the spherical overdensity criterion (Lacey & Cole, 1994 [42]). For each output time the local dark matter density is estimate at the position of each particle by calculating the distance to the tenth closest neighbour. A local density is assigned to each particle; the particles are then sorted in density and the center of the first halo is the position of the densest particle. A sphere of matter is then built around this center and stopped when the mean density within the sphere first fall below the virial value appropriate for the cosmological model at that redshift. For the definition of virial density the model of Eke et al. (1996) [21] is adopted; e.g. at $z = 0$ a newly formed halo formed when the its density is 324 times the background. At this point, the particles assigned to the first halo are removed from the list. The center of the next halo is the position of the densest particle among the remaining ones. A second sphere is built and so on, until all particles are screened.

A halo must contain at least 10 particles. The particles non ending up in haloes are considered as 'field' or 'dust' particles.

Millennium Simulation

The Millennium Simulation (Springel et al. 2005 [77]) was carried out with a customized version of the GADGET2 code, using the TreePM method (Xu, 1995) [] for evaluating gravitational forces. This is a combination of a hierarchical multipole expansion, or tree algorithm, and a classical Fourier transform particle-mesh method. This is a ΛCDM simulation with cosmological parameters: $\Omega_m = \Omega_{DM} + \Omega_b = 0.25$, $\Omega_b = 0.045$, $\Omega_\Lambda = 0.75$, $h = 0.73$, $n = 1$, $\sigma_8 = 0.9$. The simulation volume is a periodic box of size $500h^{-1}$Mpc and individual particles have a mass of $8.6 \times 10^8 h^{-1} M_\odot$. The gravitational force law is softened isotropically ona co-moving scale of $5h^{-1}$kpc. Initial conditions were laid down by perturbing a homogeneous 'glass-like' particle distribution witha realization f a gaussia random field with the ΛCDM power spectrum as give by the code CMBFAST [66]. The displacement field in Fourier space was constructed using the Zel'Dovich approximation, with the amplitude of each random ohase mode drawn from a Rayleigh distribution. The simulation started at redshift $z = 127$ and was evolved to the present.

Within the simuation a Friend-of-friend (FOF) group finder was built in order to find large virialized structures. These FOF groups found are equivalence classes in which ny pair of particles belongs to the same groups if their separation is less than 0.2 of the mean particle separation. This criterion combines particles into groups with a mean overdensity that corresponds approximately to the expected density of virialized groups. However, the FOF algorithm is not able to identify subhaloes, that are structures of gravitationally bound dark matter orbiting within the larger FOF-haloes. The subhaloes are found with an improved version of the SUBFIND algorithm.

Bibliography

[1] Begeman K. B., Broeils A. H., Sanders R. H., 1991, MNRAS, 249, 523

[2] Bennett C.L., Halpern M., Hinshaw G., Jarosik N., Kogut A., Limon M., Meyer S.S., Page L., Spergel D. N., Tucker G.S., Wollack E., Wright E.L., Barnes C., Greason M.R., Hill R.S., Komatsu E., Nolta M.R., Odegard N., Peiris H.V., Verde L., Weiland J.L., 2003ApJS..148....1B

[3] Benson A.J., Lacey C.G., Baugh C.M., Cole S., Frenk C.S., 2002MNRAS.333..156B

[4] Benson A.J., Kamionkowski M., Hassani S.H., 2005MNRAS.357..847B

[5] Benson A.J., 2008MNRAS.388.1361B

[6] Blain, A. W.; Longair, M. S., 1993MNRAS.265L..21B

[7] Bond J.R., Cole S., Efstathiou G., Kaiser N., 1991, ApJ, 379, 440

[8] Bond J.R. & Myers S.T., 1996, 1996ApJS..103....1B

[9] Bond J.R. & Myers S.T., 1996, ApJ Supplement Series, 103, 41

[10] Bond J.R. & Myers S.T., 1996, ApJ Supplement Series, 103, 63

[11] Bullock J.S., Kravtsov A.V., Weinberg D.H., 2000ApJ...539..517B

[12] Cavaliere, A., Colafrancesco, S., Scaramela, R.1991ApJ...380...15C

[13] Chandrasekhar S., 1943, Rev. Mod. Phys., 15, 1

[14] Coles P. & Lucchin F., "Cosmology (The Origin and Evolution of Cosmic Structure)", Second Edition, John Wiley & Sons, Chichester, 2003

[15] Conroy C., Wechsler R.H., Kravtsov A.V., 2007ApJ...668..826C

[16] Couchman H.M.P., Thomas P.A., Pearce F.R., 1995ApJ...452..797C

[17] De Lucia G., Blaizot J., 2007MNRAS.375....2D

[18] Dunkley J, Spergel D.N., Komatsu E., Hinshaw G., Larson D., Nolta M.R., Odegard N., Page L., Bennett C.L., Gold B., Hill R.S., Jarosik N., Weiland J.L., Halpern M., Kogut A., Limon M., Meyer S.S., Tucker G.S., Wollack E., Wright E.L., 2009ApJ...701.1804D

[19] Eisenstein D.J., Loeb A., 1995ApJ...439..520E

[20] Efstathiou G., Davis M., White S. D. M., Frenk C. S., 1985ApJS...57..241E

[21] Eke V.R., Cole S., Frenk C.S. 1996MNRAS.282..263E

[22] Erdelyi A., Higher Trascendental Functions, Vol 2, 1953, MacGraw Hill Books Company, New York

[23] Fakhouri O., Ma C.P., 2008MNRAS.386..577F

[24] Gabici S., Blasi P., 2003ApJ...583..695G

[25] Gao L., White S.D.M., Jenkins A., Stoehr F., Springel V., 2004MNRAS.355..819G

[26] Giocoli C, Moreno J, Sheth R. K., Tormen, G., 2007MNRAS.376..977G

[27] Gottlober S., Klypin A., Kravtsov A., 1999ApSS.269..345G

[28] Guth A.H., 1981, Phys. Rev. D, 23, 347

[29] Guth A.H. & Pi S.-Y., 1982, Phys. Rev. Lett., 49, 1110

[30] Haehnelt M.G., 1994MNRAS.269..199H

[31] Hernquist L., 1989Natur.340..687H

[32] Hu W. http://background.uchicago.edu/ who/metaanim.html

[33] Jenkins A., Frenk C.S., White S.D.M., Colberg J.M., Cole S., Evrard A.E., Couchman H.M.P., Yoshida N., 2001MNRAS.321..372J

[34] Kamionkowski M., Liddle A.R., 2000PhRvL..84.4525K

[35] Kauffmann G., Colberg J. M., Diaferio A., White S. D. M., 1999MNRAS.303..188K

[36] Kitayama T. & Suto Y., 1996a, MNRAS, 280, 638

[37] Kitayama T. & Suto Y., 1996b, ApJ, 469, 480

[38] Kolatt T.S., Bullock J.S., Somerville R.S., Sigad Y., Jonsson P., Kravtsov A.V., Klypin A.A., Primack J.R., Faber S.M., Dekel A., 1999ApJ...523L.109K

[39] Komatsu E., Dunkley J., Nolta M.R., Bennett C.L., Gold B., Hinshaw G., Jarosik N., Larson D., Limon M., Page L., Spergel D.N., Halpern M., Hill R.S., Kogut A., Meyer S.S., Tucker G.S., Weiland J.L., Wollack E., Wright E.L. 2009ApJS..180..330K

[40] Kundu D., Gupta R. D., 2006 Journal of Modern Applied Statistical Methods, vol. 5, no. 1, 300-306

[41] Lacey C. & Cole S., 1993, MNRAS, 262, 627

[42] Lacey C. & Cole S., 1994, MNRAS, 271, 676

[43] Lapi A., Shankar F., Mao J., Granato G.L., Silva L., De Zotti G., Danese L., 2006ApJ...650...42L

[44] Lukic Z., Heitmann K., Habib S., Bashinsky S., Ricker P.M., 2007ApJ...671.1160L

[45] Mahmood A. & Rajesh R., 2005, ArXiv Astrophysics e-prints, arXiv:astro-ph/0502513

[46] Peacock J.A., "Cosmological Physics", Fifth Reprint, Cambridge University Press, Cambridge, 2003

[47] Menou K., Haiman Z., Narayanan V.K., 2001ApJ...558..535M

[48] Mihos J.C., Hernquist L., 1996ApJ...464..641M

[49] Milosavljevic, M., Merritt D., 2001ApJ...563...34M

[50] Moreno J., Giocoli C., Sheth R.K., 2008MNRAS.391.1729M

[51] Moreno J., Giocoli C., Sheth R.K., 2009MNRAS.397..299M

[52] Neistein, E., Dekel A., 2008MNRAS.388.1792N

[53] Pan J., 2007MNRAS.374L...6P

[54] Pan J., Wang Y., Chen X., Teodoro L.F.A., 2008MNRAS.389..461P

[55] Peacock J.A. & Dodds S.J., 1996, MNRAS, 280, L19

[56] Percival W.J., Scott D., Peacock J.A., Dunlop J.S., 2003MNRAS.338L..31P

[57] Percival W., Miller L., 1999MNRAS.309..823P

[58] Press W.H. & Schechter P., 1974, ApJ, 187, 425

[59] Risken H., "The Fokker-Planck Equation (Methods of Solution and Applications)", Second Edition, Springer-Verlag, Berlin, 1989

[60] Reed D., Gardner J., Quinn T., Stadel J., Fardal M., Lake G., Governato F., 2003MNRAS.346..565R

[61] Reed D.S., Bower R., Frenk C.S., Jenkins A., Theuns T. 2007ASPC..379...12R

[62] Rubiño-Martín J.A., Betancort-Rijo J., Patiri S.G., 2008MNRAS.386.2181R

[63] Santos M.R., Bromm V., Kamionkowski M., 2002MNRAS.336.1082S

[64] Sasaki S., 1994, PASJ, 46, 427

[65] Scannapieco E., Schneider R., Ferrara A., 2003ApJ...589...35S

[66] Seljak U., Zaldarriaga M., 1996ApJ...469..437S

[67] Sheth R.K., 1998, MNRAS 300, 1057

[68] Sheth R.K., Mo H.J., Tormen G., 2001, MNRAS, 323, 1

[69] Sheth R.K. & Tormen G., 1999, MNRAS, 308, 119

[70] Sheth R.K. & Tormen G., 2002, MNRAS, 329, 61

[71] Sheth R.K. & Tormen G., 2004, MNRAS, 350, 1385

[72] Smoluchowski M. V., 1916ZPhy...17..557S

[73] Somerville R.S., 2002ApJ...572L..23S

[74] Spergel D.N., Verde L., Peiris H.V., Komatsu E., Nolta M.R., Bennett C.L., Halpern M., Hinshaw G., Jarosik N., Kogut A., Limon M., Meyer S.S., Page L., Tucker G.S., Weiland J.L., Wollack E., Wright E. L. 2003ApJS..148..175S

[75] Spergel D.N., Bean R., Doré O., Nolta M.R., Bennett C.L., Dunkley J., Hinshaw G., Jarosik N., Komatsu E., Page L., Peiris H.V., Verde L., Halpern M., Hill R.S., Kogut A., Limon M., Meyer S.S., Odegard N., Tucker G.S., Weiland J.L., Wollack E., Wright E.L., 2007ApJS..170..377S

[76] Springel V., Yoshida N., White S.D.M., 2001NewA....6...79S

[77] Springel V., White S.D.M., Jenkins A., Frenk C.S., Yoshida N., Gao L., Navarro J., Thacker R., Croton D., Helly J., Peacock J.A., Cole S., Thomas P., Couchman H., Evrard A., Colberg J., Pearce F., 2005Natur.435..629S

[78] Stiff D., Widrow L.M., Frieman J., 2001PhRvD..64h3516S

[79] Taruya A. & Suto Y., 2000, ApJ, 542, 559

[80] Tormen G., 1998, MNRAS, 297, 648

[81] Tormen G., Dispense del corso: *Cosmologia Mod. A*, Padova, 2003

[82] Verde L., Kamionkowski M., Mohr J.J., Benson A.J., 2001MNRAS.321L...7V

[83] Verde L., Haiman Z., Spergel D.N., 2002ApJ...581....5V

[84] Vitvitska M., Klypin A.A., Kravtsov A.V., Wechsler R.H., Primack J.R., Bullock J.S., 2002ApJ...581..799V

[85] Volonteri M., Haardt F., Madau P., 2002ApSS.281..501V

[86] Warren M.S., Abazajian, K., Holz D.E., Teodoro L., 2006ApJ...646..881W

[87] Wechsler R.H., Bullock J.S., Primack J.R., Kravtsov A.V., Dekel A., 2002ApJ...568...52W

[88] White S.D.M., Cosmology and Large Scale Structure, les Houches session LX. Elsevier, Amsterdam p.77

[89] White S.D.M., Frenk C.S., 1991ApJ...379...52W

[90] White S.D.M., Rees M.J., 1978MNRAS.183..341W

[91] White S.D.M., Silk J., 1979ApJ...231....1W

[92] Wyithe S., Loeb A., 2003ApJ...595..614W

[93] Zel'Dovich Ya.B., 1970A&A.....5...84Z

[94] Zhang J., Hui L., 2006ApJ...641..641Z

[95] Zhang J., Ma C.P., Fakhouri O., 2008MNRAS.387L..13Z

[96] Zwiky, F., 1937, ApJ, 86, 217Z

"...come ultime volontà le poesie di Vian."
V.B.